UNIVERSITY OF CALIFORNIA, SAN DIEGO

Theoretical Studies on Hydrogen Ignition and Droplet Combustion

A dissertation submitted in partial satisfaction of the
requirements for the degree Doctor of Philosophy
in
Engineering Sciences (Engineering Physics)

by

Gonzalo Del Álamo

Committee in charge:

Professor Forman A. Williams, Chair
Professor Juan C Lasheras
Professor W. Kendall Melville
Professor Kalyanasundaram Seshadri
Professor William W. Young

2006

The dissertation of Gonzalo Del Alamo is approved, and it is acceptable in quality and form for publication on microfilm:

Chair

University of California, San Diego

2006

Table of Contents

LIST OF FIGURES

LIST OF TABLES

Acknowledgements

I are greatly indebted to Professor Forman A. Williams, for giving me the great privilege of learning from him, and to Antonio Sànchez, for giving me the first opportunity to work in Combustion Theory. I hope our collaboration will continue in the future. I am also indebted to Professor Amable Liñàn for helpful discussions in the course of this work. Related discussions with Professor Lasheras, Stefan Llewellyn Smith, and Constantine Pozrikidis also are greatly appreciated. Thanks are also due to all my friends, who were sometime very patient and made my stay a pleasant experience. I hope our friendship will continue for many years. Special thanks go to my family for supporting me emotionally, and to Juliana, for making my life so wonderful.

VITA

1975	Born, Madrid, Spain.
July, 2001	B.A. Engineering Degree (Mechanical), Universidad Carlos III de Madrid, Madrid, Spain.
Sept. 2001-July 2002	Consultant Engineer.
Jan. 2003-June 2006	Research Assistant, Department of Mechanical and Aerospace Engineering University of California, San Diego
June 2006	Ph. D. University of California, San Diego

PUBLICATIONS

"Hydrogen-Oxygen Induction Times Above Crossover Temperatures," by G. Del Álamo, F. A. Williams and A. L. Sánchez, Combustion Science and Tecnology, Vol. 176, No. 10, pp. 1599-1626, 2004.

"Thermal-Runaway Approximation for Ignition Times of Branched-Chain Explosions," by G. Del Álamo and F. A. Williams, AIAA Journal, vol. 43, no. 12, pp. 2599-2605, 2005.

"Theory Of Vaporization Of A Droplet In Slowly Varying Rectilinear Flow At Low Reynolds Numbers," by G. Del Alamo and F. A. Williams. (submitted).

FIELDS OF STUDY

Major Field: Engineering

Studies in Combustion.
Professor Forman A. Williams

Studies in Physics of Gases and Plasma.
Professors Forman A. Williams, Robert Cattolica.

Studies in Physics Plasma.
Professor Sergei Krasheninnikov.

Studies in Fluid Mechanics and Turbulence.
Professors Paul Linden, Stephan L. Smith and Sutanu Sharkar

Studies in Applied Mathematics.
Professors Stephan Llewellyn Smith and William R. Young

Studies in Numerical Analysis.
Professors Costas Pozrikidis and Tom Bewley

ABSTRACT OF THE DISSERTATION

Theoretical Studies on Hydrogen Ignition and Droplet Combustion

by

Gonzalo Del Álamo

Doctor of Philosophy in Engineering Sciences (Engineering Physics)

University of California, San Diego, 2006

Professor Forman A. Williams, Chair

The objective of this work is to investigate theoretically two different problems of interest in Combustion. First, autoignition in hydrogen-oxygen systems above crossover temperatures and under various conditions of pressure and composition is addressed computationally and by asymptotic methods. Different descriptions of the detailed chemistry are evaluated through comparison of computed and measured ignition times, and a balance between accuracy and simplicity is struck in selecting rate parameters to be used in investigating reduced chemistry. For isobaric, homogeneous, and adiabatic mixtures, only five elementary steps suffice to describe accurately ignition over the range of conditions addressed, which allows the derivation of explicit formulas for the induction time by neglecting heat release and reactants consumption. Further reduction of the chemistry to two overall steps, is used to include the effect of the energetics in the temperature-dependent initiation and branching rates. In this approach, an asymptotic analysis for high activation energy of the branching step is developed for predicting ignition times of branched-chain explosions on the basis of a criterion of thermal runaway.

The second study addresses the vaporization of a droplet in rectilinear motion relative to a stagnant gaseous atmosphere for the limit of low Reynolds numbers and slow variation of the droplet velocity. A formal asymptotic analysis is performed, showing that, under the conditions addressed, there is an inner region in

the vicinity of the droplet within which the flow is nearly quasisteady except during shorts periods of time when the acceleration changes abruptly and a fully time-dependent outer region in which departures of velocities and temperatures from those of the ambient medium are small. Matched asymptotic expansions, followed by a Greens-function analysis of the outer region enable expressions to be obtained for the velocity and temperature fields and for the droplet drag and vaporization rate. The results are applied to problems in which the droplet experiences constant acceleration, constant deceleration and oscillatory motion. The results, which identify dependences on the Prandtl number and the transfer number, are intended to be compared with experimental measurements on droplet behaviors in time-varying flows.

Chapter 1

Introduction

From early theoretical studies, multicomponent reactive gases are believed to be in local thermodynamical equilibrium based on the smallness of the mean-free path compared to the characteristic length scales of the convective and molecular transport phenomena. This approximation allows for the derivation of the governing conservation equations for multicomponent reactive-gas flows from the Boltzmann Equation [1], including Arrhenius-type description of the detailed chemistry and the dependence of the coefficients of viscosity, thermal conductivity, molecular diffusivity and thermal diffusivity on thermochemical variables [2]. Accurate numerical integration of these conservation equations and the measurements taken from experiments under carefully-controlled conditions are able to reproduce most of the gas-phase combustion processes encountered in practical situations, but the interpretation of their results becomes always an important and difficult task. Theory is still playing an important role in Combustion Science [3] to understand the interdependence of the chemical kinetics, the molecular transport phenomena and the fluid mechanics present in combustion phenomena. Due to the disparity in the charactersitic time and length scales present in typical reactive flows, large and small dimensionaless parameters appear in the nondimensionalized conservation equations [4]. Different types of asymptotic methods based on these parameters have been developed in the last decades to describe

analytically fundamental combustion phenomena such as gaseous deflagration and detonations, ignition of reactive mixtures, nonpremixed and partially-premixed flames and extinction [3].

In the present work, two different problems related to combustion are studied theoretically: the autoignition of high-temperature hydrogen-oxygen systems under adiabatic and homogeneous conditions and the unsteady vaporization of a droplet in slowly varying motion at low Reynolds numbers.

1.1 Hydrogen Ignition

Ignition of hydrogen-oxygen systems with various inerts is of interest because of applications in supersonic-combustion ramjet engines and in detonative-combustion engines concepts for aerospace propulsion, as well as concerns about safe storage, handling and transportation of hydrogen fuel associated with planning for a possible future hydrogen economy. Among the mixtures on which these needs focus attention are undiluted hydrogen-oxygen mixtures, hydrogen-air mixtures and mixtures with enhanced content of water vapor, envisioned in certain scenarios addressing nuclear-reactor safety, for example.

Two different type of problems concerning ignition of combustible systems can be identified depending if the mixture is homogeneous or nonuniform. In the former, concentrations and temperature gradients appear within the mixture, so that chemical reactions are taking place in presence of species and heat transport. Examples of this type are the ignition of diffusion flames and the initiation to deflagrations and detonations. Ignition in homogeneous mixtures is a time-evolution problem described by first-order ordinary differential equations with initial conditions. In these problems the system is typically assumed to be closed, all the thermodynamical variables and the species concentrations being uniform during ignition. Examples of this type are the ignition of combustible mixtures inside vessels and the ignition within the induction zone behind the shock wave in ZND

detonations. The characteristics of ignitability of hydrogen-oxygen homogeneous mixtures as a function of the initial temperature and pressure have been measured experimentally inside vessels by Lewis and Von Elbe [5], resulting in the reversed-S type of curves sketched schematically in Fig. 1.1. The three branches of this curve

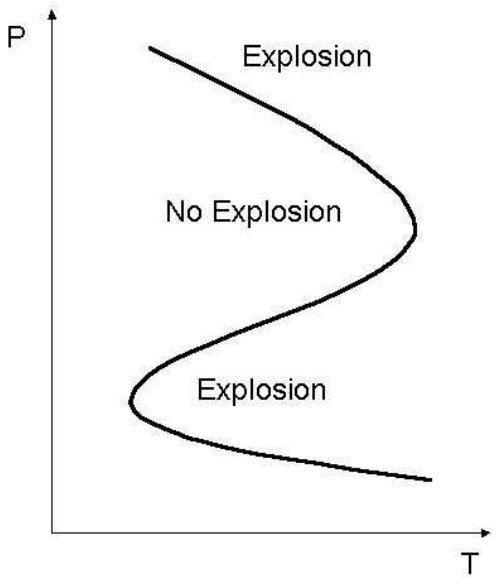

Figure 1.1 Schematic representation of the dependence of the explosion limits for H_2-O_2 mixtures on the initial temperature and pressure.

correspond to the different explosion limits typical of H_2-O_2 systems. Attention is focused here on the ignition of homegeneous and adiabatic mixtures with initial conditions corresponding to the explosion peninsula appearing in the lower part of the curve in Fig. 1.1, between the first and the second explosion limits. Under these conditions, the ignition of hydrogen-oxygen systems exhibits characteristic features of both branched-chain explosions and thermal explosions, because of the autocatalytic character and the high-activation energy of the chain-branching reactions [2].

A typical ignition history for H_2-O_2 systems at initial temperatures above the second explosion limit and under adiabatic and homogeneous conditions is

represented in Fig. 1.2, which shows the time evolution of the temperature and the concentration of reactants and H-radical for a stoichiometric hydrogen-air mixture at initial temperature $T_0 = 1500K$ and initial pressure P=1bar. It can be seen a

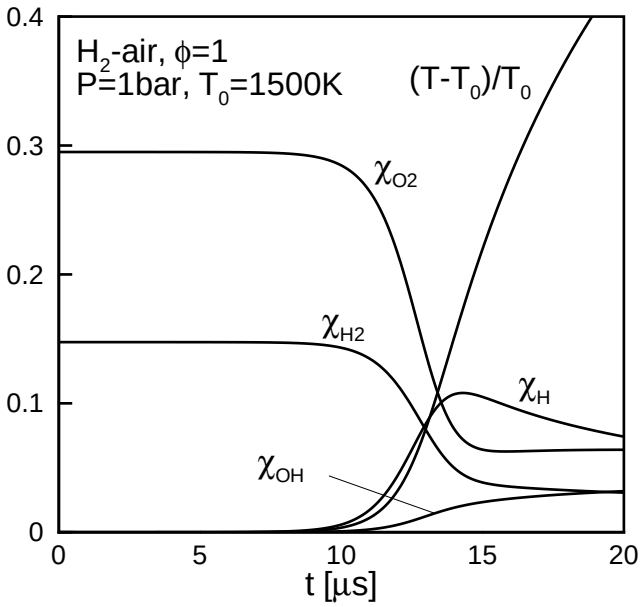

Figure 1.2 Time evolution of an adiabatic, isobaric, homogeneous H_2-air stoichiometric mixture at initial temperature $T_0 = 1500K$ and P=1 bar.

relatively long period of chain-carrier growth through the branching steps H + O_2 → OH+O, H_2 + O → OH + H and H_2 + OH → H_2O + H prior to significant heat release, which occurs mainly through the recombination reaction H + O_2 + M → HO_2 + M once a sufficiently large H-radical pool has formed [5]. This period, often called the induction period, is the dominant contribution to the ignition delay time, and the one to which simple approximations are considered in Chapters 3 and 4. Because of its practical importance the induction time in hydrogen-oxygen systems has remained an active topic for over forty years. Three different methodologies can be identified: experimental, numerical and analytical.

Shock-tube experiments are suitable to measure accurately ignition delay times, as well as to determine the chemical kinetics of combustion systems, under

homogeneous, adiabatic, isobaric, and stationary conditions. Nonideal effects in this type of experiments, such as inhomogeneities in the mixture and the interaction of the shock wave and the boundary layer, are typically small [28]. Numerous shock-tube experimental measurements of hydrogen-oxygen induction times are available in the literature [6-27]. The criteria used in experiments for defining the induction time vary. Thus, for some authors the induction period ends at the onset of luminosity or as the pressure rises above a given threshold value through heat release, while others prefer to relate the induction time to radical concentrations such as maxima of OH emission or absorption. Under most conditions, unlike situations that sometimes occur with some other fuels, the resulting value of the induction time depends relatively weakly on the definition used.

To determine computationally the ignition time, the entire time history is obtained based on numerical integrations, marching forward in time, of conservation equations that include detailed elementary chemistry, exothermic overall, believed to apply at the molecular level for the combustion system addressed [29,30]. Since ignition processes evolve in time, there is always some arbitrariness in defining computationally a single ignition time. One most relevant characteristic time often is taken to be the inflection point in the temperature-time profile, calculated for a homogeneous, adiabatic, isobaric system. The rationale for this choice in explosion theory is that the inflection point usually marks the onset of heat release to a level at which the chemistry begins to affect the gas dynamics, causing rapid pressure buildup, while the effect of chemistry on the pressure field remains fairly negligible prior to that time. This procedure is used in Chapter 2 to evaluate the knowledge currently available on H_2-O_2 ignition chemistry through comparisons of ignition-delay times obtained by numerical integrations using various chemical-kinetic mechanisms with some of the most recent shock-tube experimental results.

Although calculation of the temperature-inflection ignition time is rather straightforward computationally, it is convenient for quick estimates and for improved understanding to have analytical formulas that are derived by rational

systematic methods and that provide good approximations to the experimental and computational results. The analytical derivation of explicit formulas for the ignition time relies on the systematical reduction of the detailed chemistry. One procedure is to identify the main elementary reaction by which the non-steady-state species are consumed or produced [31], this set of reactions being called short mechanism. This approach was followed in early theoretical studies devoted to the calculation of hydrogen-oxygen induction times at high temperature [7,11,17,20,32,33]. Although the success of many of these previous analytical and computational efforts has been limited by uncertainties in reaction-rate parameters, especially in the earlier investigations, these works provided much understanding in the ignition process. For instance, already in the 1950's Schott and Kinsey [7] anticipated that the radicals O and OH follow a chemical-kinetic steady-state approximation if the mixture is sufficiently rich, and they used this to determine the induction time from the evolution of the H-atom concentration, the only species out of steady state. Both reactant consumption and heat release were found to be negligible during this initial stage of radical growth, giving an H-atom concentration that increases exponentially in time. Since $H + O_2 \rightarrow OH + O$ is the rate-limiting reaction, the resulting induction time was seen to be proportional to the reciprocal of the initial oxygen concentration [7]. This calculation procedure was extended in later works [11,17,20,32,33] by accounting for a larger number of radicals, to give a system of linear differential equations for evolution of the radical pool. The resulting induction time becomes inversely proportional to the largest eigenvalue of the associated eigenvalue problem, showing a dependence on the mixture composition more complex than that of rich mixtures. One such approximation for branched-chain explosions is followed in Chapter 3, where the chemistry is reduced to five elementary steps including non-steady-states for the radicals H, OH and O. The induction time is then defined as the time for radical concentrations to reach partial equilibrium isothermally. Although often reasonable, this approximation can overestimate ignition times by neglecting the rate increase associated with the

temperature increase caused by the heat release that occurs during radical buildup.

Further reduction of the chemistry allows to include the effect of the exothermicity in the analysis. The procedure is to identify an operable set of global reactions, typically from the short mechanism by means of steady-state and partial equilibrium approximations, thought to describe reasonably the overall influences of the elementary chemistry and the energetics [31]. Following this procedure results in simplified chemical models, where the parameters appearing therein are related to rate parameters of the elementary combustion chemistry of real fuel-oxidizer mixtures [34-41]. Different approaches to simplify the chemistry and to solve mathematically the resulting governing equations can be identified in the literature. For example, Varatharajan and Williams [39] considered a two-step chemical model which included a constant initiation rate and a temperature-dependent branching rate. The effect of the exothermicity was taken into account through a thermal-runaway criterion based on activation-energy asymptotics when the dominant heat release occurs in the branching step, obtaining parametric expressions for the ignition time. Practically at the same time, Bonilla et al [40] selected a two-step mechanism including temperature dependence in both initiation and branching rates, a slow temperature-insensitive recombination step and the effect of fuel depletion. In their analysis, the ratio of recombination to branching was assumed to be small, and the heat release to occur only through recombination step. They were able to provide the complete time history for the temperature and the fuel and radical concentration by means of a nonlinear multiscale technique based on rate-ratio asymptotics. The same chemical model was used later by Blythe et al [41], but they extended the analysis, based on activation-energy asymptotics, by considering initial temperature closed to the crossover limit.

In applying previous results to hydrogen-oxygen shock-tube ignition times, quantitative deficiencies to predict experimental measurements are found, that motivated us to investigate possible alternative simplified formulations. In Chapter 4 an alternative theory is presented, the chemical model including temperature-

dependent branching and initiation rates and temperature-insensitive recombination rate. One or both of the branching and recombination steps are assumed to be exothermic, whereas the initiation step can be endothermic or exothermic. The analysis is based on the smallness of the ratio of initiation to branching rates and the large activation energy of the branching step. An asymptotic formula for the ignition time is obtained by using a thermal-runaway criterion, which compares well with computational results. Attention is focused on branched-chain thermal explosions, defined as processes in which chain branching and heat release both occur in the same strongly temperature-dependent overall steps [39], which are characteristic of hydrogen-oxygen systems and which may also apply to other combustibles, such as acetylene-oxygen mixtures.

1.2 Droplet Combustion

Because of interest in understanding spray-combustion characteristics in rocket and gas-turbine combustors, internal combustion engines and oil-fires furnaces, studies of the combustion of fuel droplets have remained active research topics for over fifty years. Godsave [74] and Spalding [75] were the first to offer simplified models for the spherically symmetrical combustion of a liquid fuel droplet in a gaseous oxydizing atmosphere, envisioning the combustion to be diffusion-controlled and thereby deriving the well-known d-square law, according to which the square of the droplet diameter decreases linearly with time. Numerous reviews of this early work and somewhat later developments have been written, among them the treatments by Forman Williams [76], Alan Williams [77], Jerry Faeth [78] and Ed Law [79]. Most investigations pertain to quasisteady conditions, an approximation justifed for stationary droplets by the typically large ratio of liquid to gas density at normal atmospheric conditions, and some authors, such as Fendell and co-workers [80,81], Ayyaswamy and co-workers [82,83], Whichman and Baum [84] and Ackerman and Williams [85] address nonspherical quasisteady con-

vection in droplet combustion for small Reynolds numbers under these conditions. For large ratios of liquid to gas densities there have been relatively few studies of the possible time-dependent effects, although Crespo and Liñán [86] and Waldman [87] analyzed the time-dependent behavior for spherical symmetry. More recent reviews are available [88-92]. The ultimate interest of the present study is to consider effects of nonspherical time-dependent convection on the combustion of droplets having a large ratio of liquid to gas density, since in many applications the velocity of the droplet relative to the gas varies with time under such conditions.

To begin to approach this problem, attention in Chapter 5 is focused on vaporization of a droplet in slowly varying flows at low Reynolds numbers. Conditions are addressed in which the gas density can be approximated as being constant, that is, large temperature changes are excluded. Although this approximation is unrealistic in droplet-combustion applications, a thorough understanding of the constant-density problem is needed before variable-density effects can properly be addressed, and through judicious selection of values of properties, it has in fact been possible to relate results of constant-density analysis to results of droplet-combustion experiments in the presence of slow forced convection [85].

Given the approximations of a constant gas density and a large ratio of liquid to gas density, significant literature that does not address combustion underlies the present investigation [93]. The latter approximation enables the time variation of the droplet diameter to be neglected, as is done here. The problem then reduces to that of determining the velocity and temperature fields for flow around a sphere of fixed diameter. That flow, in general, induces flow of the liquid inside the droplet [94,95], but in the present work, to minimize the number of parameters that appear in the problem so as to simplify the results and facilitate understanding, it is assumed that the liquid viscosity is sufficiently large for liquid motion to be neglected (often a reasonable approximation). Therefore only rigid spherical droplets are considered. Moreover, for similar reasons, temperature variations within the liquid are neglected, so that only gas-phase conservation

equations need to be addressed. Boundary conditions at the droplet surface lead to specification of the temperature there as the vaporization temperature, determination of the proportionality between the heat flux to the droplet surface and the vaporization rate through the transfer number (denoted by B and defined below), and imposition of the no-slip condition for the velocity field there.

The droplet vaporization results in radially outward flow at the droplet surface, which then interacts with the externally imposed nonspherical convection through the equations of mass and momentum conservation. Consideration of this interaction distinguishes the present investigation from many previous investigations in which flow through the surface of the sphere is neglected. In that limit of a neglegible mass source, in the first approximation for low Reynolds numbers in steady flow, the Stokes drag law applies [96], the uniformly valid leading-order flow field having been first obtained by Oseen [97], as explained by Proudman and Pearson [98]. Heat and mass transfer in this same mass-source-free type of steady flow, leading to determination of Nusselt numbers, were addressed somewhat later [99-101], and the effect of the mass source on the flow was considered subsequently [95,102]. With coupling between the heat-transfer rate and the strength of the mass source, bringing in the equation for energy conservation, the Prandtl number σ becomes an additional parameter in the problem addressed here. A number of results will be summarized for steady flow, in forms simpler than those that can be found in the literature.

Tme-varying motions of droplets can introduce numerous complications that depend strongly on the type of motion [103]. For this reason, if analytical progress is to be made, it is necessary restrict attention to particular classes of motion. With this in mind, only straight-line, rectilinear motion is considered here, as a first step that needs to be undertaken before it is reasonable to address other, more complex motions. Moreover, to enable expansions to be developed, attention is restricted to slowly varying conditions, for which the flow in the vicinity of the droplet is quasisteady in the first approximation. The unsteady force on solid

spheres in flows of this type has been considered previously [104-107], and heat transfer to spheres in such flows has been analyzed without considering mass-source effects [108-111]. These various studies have addressed acceleration, deceleration and oscillatory motion, but not coupling of the momentum and energy fields, which is the subject of the present work. The Greens-function methods of previous studies [111], however, are essential in the present analysis, which addresses diffusion-controlled droplet evaporation in the limit of low-velocity flow varying slowly in time.

Chapter 2

Review of H_2 - O_2 Ignition Chemistry

The chemistry of hydrogen-oxygen combustion is probably known better than that of any other combustion system, but research on hydrogen-oxygen chemistry continues, partially because the applications often require greater accuracy in predictions than is required for other combustible mixtures. Moreover, since hydrogen-oxygen chemistry is basic to all hydrocarbon combustion chemistry, there is strong motivation for determining hydrogen-oxygen rate parameters as accurately as possible. The purpose of this chapter is to review the knowledge currently available on H_2-O_2 kinetics above crossover temperatures and over a wide range of conditions of pressure and composition. Through numerical integrations various chemical-kinetic mechanisms are used to calculate ignition histories, which are compared with experimental results. A balance between accuracy and simplicity is struck in selecting rate parameters to be used in investigating reduced chemistry

2.1 Detailed Chemistry

Since hydrogen-oxygen kinetics is a submechanism of all detailed kinetic schemes for hydrocarbon oxidation, there are numerous sources for detailed

hydrogen-oxygen kinetic mechanisms (Maas and Warnatz, 1988 [42]; Miller and Bowman, 1989 [43]; Balakrishnan and Williams, 1994 [44]; Tan et al., 1994 [45]; Frenklach et al., 1995 [46]; Ranzi et al., 1995 [47]; Marinov, Westbrook and Pitz, 1996 [48]; Allen, Yetter and Dryer, 1997 [49]; Lindstedt and Skevis, 1997 [50]; Glarborg et al., 1998 [51]; Mueller, Yetter and Dryer, 1999 [52]; Bhattacharjee et al., 2003 [53]; Li et al., 2003 [54]; Saxena and Williams, 2006 [56]). Table 2.1 lists the forward steps and associated rate parameters of the detailed mechanism selected in this work for subsequent reduction; all steps are reversible, with reverse rates obtained from equilibrium constants and forward rates. It is an updated version obtained by Saxena and Williams [56] (published on the cited website) from the original mechanism of Balakrishnan and Williams [44] and the later version of Del Álamo and Williams [55]. The mechanism of Balakrishnan and Williams [39] was developed originally only for supersonic-combustion applications at pressures below 10 bar and therefore did not include falloff. As a consequence, when tested up to very high pressures [22], it gave predictions in reasonable agreement with those of other mechanisms at the lower pressures but yielded ignition times about an order of magnitude shorter than other mechanisms at 600 bar. Addition of falloff for just one step $H_2O_2 + M \rightarrow 2OH + M$, following the Troe formulation [71], brought the high-pressure predictions into line with other mechanisms (there, of course, being no ignition data at such high pressures for testing any mechanism). This experience reinforced the idea that what leads to success of a mechanism is the correct inclusion of one key step, rather than addition of a large number of steps. Moreover, in view of the uncertainties in rate parameters for most of the steps in very large mechanisms, adding large numbers of steps may in fact degrade the quality of the mechanism. It is for these reasons that we have chosen to try to keep our detailed mechanism as short as possible. Table 2.1 also contains the step $H_2O_2 + O \rightarrow HO_2 + OH$, not in the mechanism of Balakrishnan and Williams [39]; this has a small but noticeable effect under lean, low-temperature, high-pressure conditions.

Table 2.1 The detailed mechanism with rate coefficients in the Arrhenius form k=AT^nexp(-E/RT).

Number	Reaction		A^a	n^a	E^a
1	$H + O_2 \rightleftharpoons OH+O$		3.52E+16	-0.7	71.42
2	$H_2 + O \rightleftharpoons OH + H$		5.06E+04	2.67	26.32
3	$H_2 + OH \rightleftharpoons H_2O + H$		1.17E+09	1.3	15.21
4	$H_2O + O \rightleftharpoons OH + OH$		7.60E+00	3.84	53.47
5[b]	$H + O + M \rightleftharpoons OH + M$		4.71E+18	-1	0
6[c]	$H + H + M \rightleftharpoons H_2 + M$		1.30E+18	-1	0
7[d]	$H + OH + M \rightleftharpoons H_2O + M$		4.00E+22	-2	0
8[e]	$O + O + M \rightleftharpoons O_2 + M$		6.17E+15	-0.5	0
9[f]	$H + O_2 + M \rightleftharpoons HO_2 + M$	k_0	5.75E+19	-1.4	0
		k_∞	4.65E+12	0.44	0
10[b]	$O + OH + M \rightleftharpoons HO_2 + M$		8.00E+15	0	0
11	$HO_2 + H \rightleftharpoons OH + OH$		7.08E+13	0	1.23
12	$HO_2 + H \rightleftharpoons H_2 + O_2$		1.66E+13	0	3.44
13	$HO_2 + H \rightleftharpoons H_2O + O$		3.10E+13	0	7.2
14	$HO_2 + O \rightleftharpoons OH + O_2$		2.00E+13	0	0
15	$HO_2 + OH \rightleftharpoons H_2O + O_2$		2.89E+13	0	-2.08
16[g]	$OH + OH + M \rightleftharpoons H_2O_2 + M$	k_0	2.30E+18	-0.9	-7.12
		k_∞	7.40E+13	-0.37	0
17	$HO_2 + HO_2 \rightleftharpoons H_2O_2 + O_2$		3.02E+12	0	5.8
18	$H_2O_2 + H \rightleftharpoons HO_2 + H_2$		4.79E+13	0	33.3
19	$H_2O_2 + H \rightleftharpoons H_2O + OH$		1.00E+13	0	15
20	$H_2O_2 + OH \rightleftharpoons H_2O + HO_2$		7.08E+12	0	6
21	$H_2O_2 + O \rightleftharpoons HO_2 + OH$		9.63E+06	2	16.7

[a] Units are mol,s,cm^3,kJ and K.

[b] chaperon efficiencies are 2.5 for H_2, 12.0 for H_2O, 1.9 for CO, 3.8 for CO_2, 0.75 for Ar and He and 1 for all other species.

[c] chaperon efficiencies are 2.5 for H_2, 12.0 for H_2O, 1.9 for CO, 3.8 for CO_2, 0.5 for Ar and He and 1 for all other species.

[d] chaperon efficiencies are 2.5 for H_2, 12.0 for H_2O, 1.9 for CO, 3.8 for CO_2, 0.38 for Ar and He and 1 for all other species.

[e] chaperon efficiencies are 2.5 for H_2, 16.3 for H_2O, 1.9 for CO, 3.8 for CO_2, 0.2 for Ar and He and 1.0 for all other species.

[f] chaperon efficiencies are 0.7 for Ar and He, 1.0 for O_2, 16.0 for H_2O, 1.2 for CO, 2.4 for CO_2, 1.5 for C_2H_6 and 1.0 for all other species; fall-off by the Troe formulation with $F_c = \exp(-T/345K) + \exp(-345K/T)$ (Troe, 2001 [64]).

[g] chaperon efficiencies are 0.4 for Ar and He, 2.0 for H_2, 6.0 for H_2O, 1.5 for CO, 2.0 for CO_2, 2.0 for CH_4, 3.0 for C_2H_6 and 1.0 for all other species; fall-off by the Troe formulation with $F_c = 0.265\exp(-T/94K) + 0.735\exp(-T/1756K) + \exp(-5182K/T)$ (Petersen and Hanson, 1999 [67]).

The kinetic scheme of Del Álamo and Williams [55] is an updated version of the mechanism of Balakrishnan and Williams [44]. It was developed exclusively to predict accurately experimental measurements of ignition delay times but when tested to predict burning velocities exhibited noticeable deficiencies. The result of this testing prompted Saxena and Williams to introduce new modifications of rate parameters for a few of the most important elementary reactions, as well as deletion of one chain-initiation step and addition of a recombination step. The resulting mechanism is able to predict accurately the experimental measurements for autoignition, as well as premixed-flames burning velocities, and structure and extinction of diffusion flames and of partially premixed flames of hydrogen-air mixtures [56].

The rate parameters of the forward steps 1, 2 and 3 in Table 2.1, the relevant chain-branching reactions in high-temperature combustion chemistry in hydrogen-oxygen mixtures, are, respectively, the one proposed by Masten el at [57], Yetter et al [58] and Baulch [59]. Although different mechanism employed different values of the rate parameters for these reactions, comparisons of numerical calculations of ignition times with detailed chemistry (shown below) indicate the good knowlegde of the rate parameters for these reactions, especially $H + O_2 \rightarrow OH + O$, the rate constant for which is now known with less than 5% uncertainty over the temperature range investigated with lest than 5% uncertainty.

Chain-initiation is presumed here to proceed only by the reaction $H_2+O_2 \rightarrow HO_2+H$, the reverse of the step 12 in Table 2.1, as in other current mechanisms [42, 46, 48-52 and 54]. Although different mechanisms employ different values for the rate parameters of this reaction, the resulting specific reaction-rate constant differs only moderately over the range of temperatures of interest ($1000K < T < 4000K$), e.g., by less than ten percent for two internet-posted mechanisms [46] and [56]. The rate parameters of the step 12 in Table 2.1 were adopted from the values recommended by Mueller et al [60] to improve predictions of burning velocities [56], and updates the values adopted in previous versions of

the current mechanism [44,55], which were obtained from experimental data collected in the eighties [61-63]. The mechanism of Balakrishnan and Williams [44], included a second initiation step, namely $H_2+O_2 \rightarrow 2OH$, as it happens in several others mechanisms [43,45,47 and 53]. However, more recent work [64] shows fairly convincingly that this reaction does not occur. The reaction-rate parameters of this initiation step was first estimated by Semenov [65] and later improved by Ripley and Gardiner [66], but the values adopted in all the mechanisms evaluated here are the one proposed by Jachimowski and Houghton [21].

Above 10 bar, falloff for $H + O_2 + M \rightarrow HO_2 + M$ begins to have some effect, and for this the detailed falloff study of Troe [67] was adopted in [55]. Later, the low-pressure rate parameters indicated by Troe [67] for this recombination reaction with N_2 as a bath gas was adopted in [56], modififying the chaperon efficiencies of O_2 (from 0.3 to 1) and of Ar and He (from 0.5 to 0.7) to improve predictions of burning velocities. The recent shock-tube experiments of Wang, Olivier and Grönig [27] at high water dilution prompted Del Álamo and Williams to increase the chaperon efficiency of H_2O from 7 to 12 for this step [55]. However, defiencies in predicting diffusion-flames extinction prompted Saxena and Williams [56] to increase the last efficiency from 12 to 16. Other modifications from previous versions incorporated in the current mechanism shown in Table 2.1 do not have significant implications to predict experimental ignition delay times and do not play any role in the reduction of chemistry and subsequent analysis presented in the following chapters, so the reference [56] is recommended to the reader for more discussion.

It is of interest to observe that the other two most successful mechanisms [47,54] effectively have temperature-dependent chaperon efficiencies for this step; that is, they treat different third bodies as different reactions having different temperature dependences of their rate constants. While there is some evidence that this is indeed the correct thing to do, it does lengthen and complicate the detailed chemistry somewhat, and on balance, weighing simplicity and uncertainty

against accuracy, we chose to retain constant efficiencies, believing that that would provide sufficient accuracy. The analytical developments given later employ a short mechanism derived from Table 2.1, with the rate parameters listed in that table, but the analysis can be applied equally well for any other selection of rate parameters.

2.2 Comparisons with Shock-Tube Experiments

Numerous shock-tube experimental measurements of ignition delay times in hydrogen-oxygen mixtures with various inerts are found in the literature [6-27], summarized in Table 2.2 with the experimental conditions and the criteria used to measure the ignition time. We have compared ignition-time predictions of many of the chemical kinetics schemes existing in the literature [42-56] with results of some of the more recent shock-tube autoignition experiments [20,22,26,27]. Instead of exercising a shock-tube code, computations were made for homogeneous, isobaric, adiabatic conditions, with the ignition time defined as the inflection point in the temperature-time history. The later procedure is simpler to implement and quicker to run, and it gives practically the same ignition-time results as a shock-tube calculation because the pressure remains essentially constant behind the shock until the ignition runaway event occurs [28]. The computations were made with the FLAMEMaster code [68], but they were also checked with an entirely new code especially written for the present problem. Both codes gave the same results, but FLAMEMaster was much faster and therefore finally was used throughout. Some further checks were made with the CHEMKIN code [69].

With these procedures, ignition times predicted by all of the current mechanisms agreed well at sufficiently high temperatures, reflecting the good knowledge of the rate parameters for the chain-branching steps. There were, however, noticeable differences in ignition-time predictions at lower temperatures, as crossover was approached. Crossover is defined as the temperature at which the chain-

Table 2.2 Summary of experimental measurements of hydroegn-oxygen shock-tube induction times.

First author	**Technique**	**Diluent%**	ϕ	**P(bar)**	**T(K)**	**Induction Period End**
Steinberg (1955)	Reflected	-	1	4.5-9	700-1000	Light emission onset
Schott (1958)	Incident and Reflected	Ar 75-99%	0.125-9	0.15-9.5	1050-2650	OH absortion onset
Strehlow (1962)	Reflected	Ar 25-94%	1	0.026-0.052	920-1820	Pressure inflection
Fujimoto (1963)	Reflected	Ar 70%	1	0.88-2.7	800-1400	Pressure inflection and light emission onset
Miyama (1964)	Reflected	Ar 70-90%	0.25-1	4.5-5.6	890-1350	OH absortion onset and pressure rise
Asaba (1965)	Incident	Ar 96-99%	0.085-1.5	0.2-0.5	1400-2400	OH absortion and emission onset
Belles (1965)	Incident	N_2 63-75%	0.125-0.595	0.1-0.5	1100-1900	OH emission maximum and UV emission onset
Skinner (1965)	Reflected	Ar 90%	2	5	900-1100	OH emission maximum
Snyder (1965)	Reflected	N_2 55-65%	0.5-1	1.0-9.0	800-1100	Pressure inflection and UV emission onset
Voevodsky (1965)	Reflected	-	0.5	0.5-4.0	800-1700	Pressure inflection and UV emission onset
White (1965)	Incident and Reflected	Ar 0-33%	0.0037-50	0.04-0.12	1100-2200	Inflection of density profiles
Craig (1966)	Reflected	N_2 55%	1	1.0-2.0	875-1000	OH emission onset
Cohen (1967)	Reflected	Ar 0-94%	1.0-2.0	0.25-8.3	900-1650	Pressure maximum and UV emission and absortion
Just (1968)	Reflected	N_2 55-76%	0.1-1.0	0.4-1.4	900-1250	Light Emission Onset
Jachimowski (1971)	Incident	Ar 91-95%	0.063-2	0.2-0.75	1200-1800	OH absortion at 5% of Maximum
Bhaskaran (1973)	Reflected	N_2 55%	1	2.5	800-1400	Pressure inflection and Light Emission Onset
Cheng (1977)	Reflected	Ar 90%	0.5-1	1.0-3.0	1000-1800	Pressure inflection
Blumenthal (1996)	Reflected	N_2 67%	0.42	3-50	700-1200	OH emission onset and pressure inflection
Petersen (1996)	Reflected	Ar 97-99.9%	1	33-87	1100-1900	Inflection of OH absortion
Wang (2003)	Reflected	N_2 10-18%, Steam 0-40%	0.42	3.0-5.0	1100-1400	Inflection of OH absortion

branching rate becomes of the same order as the chain-breaking rate. The principal chain-breaking reactions begin with the step H + O_2 + M → HO_2 + M, and so an explicit pressure-dependent crossover temperature can be defined by equating the rate of this elementary step to the rate of the elementary branching step, although, as will be seen later in the analytical development, for ignition it is more precise to define crossover as the condition at which the rate of this three-body step equals twice the rate of the branching step. The rate parameters for the three-body step are not quite so well known, especially concerning third-body chaperon efficiencies and high-pressure falloff, and combined with the very small but still existing differences in the branching-step rate parameters, clear differences in predictions emerge near crossover, associated with different mechanisms having different crossover temperatures.

Figures 2.1 to 2.6 compares ignition-time predictions for five different selected mechanisms (present mechanism, 2006 [56]; Maas and Warnatz, 1988 [42]; Glarborg et al, 1998 [51]; GRI mechanism 3.0, 1995 [46], Allen, Yetter and Dryer, 1995 [49]) with six different sets of experimental results from four different publications (Just and Schmalz, 1968 [20]; Bhaskaran, Gupta and Just, 1973 [22]; Petersen et al., 1996 [26]; Wang, Olivier and Grönig, 2003 [28]). Although comparisons were also made for other experiments, these six cases have been selected as representative of coverage of as wide a range of experimental conditions as possible. For one of these experiments, predictions of six other mechanisms (present mechanism, 2006 [56]; GRI mechanism 2.11, [46]; Ranzi et al, 1995 [47]; Marinov, Westbrook and Pitz, 1996 [48]; Miller and Bowman, 1989 [43]; Lindstedt and Skevis, 1997 [50]; Tan et al, 1994 [45]) are shown in Fig. 2.7; although calculations were made with these other mechanisms for the other cases as well, it was deemed excessive to show all of the results. The conditions addressed in Figs. 2.1 to 2.6 are low-pressure stoichiometric (Fig. 2.1), low-pressure very fuel-lean (Fig. 2.2), moderate-pressure stoichiometric (Fig. 2.3), high-pressure stoichiometric high-argon-dilution (Fig. 2.4), moderate-pressure fuel-lean (Fig. 2.5) and moderate-pressure fuel-lean high-

water-dilution (Fig. 2.6). In judging the performance of different mechanisms, it is important to keep in mind possible experimental errors. For example, in Fig. 2.2 at the higher temperatures all mechanisms predict ignition times longer than measured, possibly because the experimental criterion, onset of light emission, precedes temperature inflection, which should coincide better with pressure inflection. In general, the newer experiments and those employing inflection criteria may be expected to be more accurate and should agree better with predictions.

The mechanisms shown in Figs. 2.1 to 2.6 were chosen with the objective of exhibiting both best agreement with experiment and maximum deviation from experiment. On balance, over all six sets of conditions, the mechanisms of Saxena and Williams [56] and of Mueller, Yetter and Dryer [52] appear best in Figs. 2.1 to 2.6, while that of Maas and Warnatz [42] consistently overpredicts ignition times, and that of Glarborg et al. [51] substantially underpredicts them, except in Fig. 2.4, where it agrees best of all; although this last mechanism agrees well at this high pressure, in the experiments of the same authors at even higher pressures its agreement is not quite so good, but as good as that of the present mechanism. The latest GRI mechanism, version 3.0 [46], is included in the figure because it is used so widely; it is designed for methane problems, not hydrogen problems, and it tends to overpredict the data, although less so than the mechanism of Maas and Warnatz [42] and usually not by very much, even at the highest pressure (Fig. 2.4), where the predictions of Marinov, Westbrook and Pitz [48] and of Lindstedt and Skevis [50] (neither shown) are by far the worst. Figure 2.7 shows that, in contrast to GRI 3.0, an earlier version, GRI 2.11, tends to underpredict ignition-time data in a representative case, although it shows good agreement at high pressure and at high water dilution (neither shown). The mechanism of Miller and Bowman [43] underpredicts ignition times (see Fig. 2.7), much like that of Glarbog et al. [51] does under most conditions, while that of Tan et al. [45] provides good agreement except for overprediction at high pressure and significant underprediction at high water dilution (neither shown). The mechanism of Ranzi et al. [47] (Fig. 2.7)

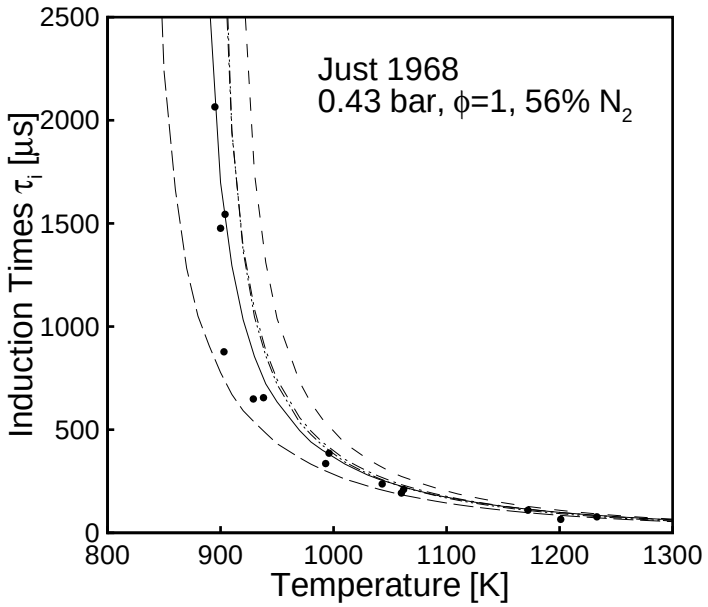

Figure 2.1 Variation with temperature of the induction time as obtained from detailed-chemistry numerical calculations; solid curves: present mechanism (2006) [56], short-dashed curves: Maas and Warnatz (1988) [42], long-dashed curves: Glarborg et al. (1998) [51], dot-dashed curves: GRI mechanism 3.0 (1995) [46], dot-dot-dashed curves: Allen, Yetter and Dryer. (1995) [49], while the symbols denote the shock-tube experimental results of Just and Schmalz (1968) [20] (p = 0.43 bar, ϕ=1)

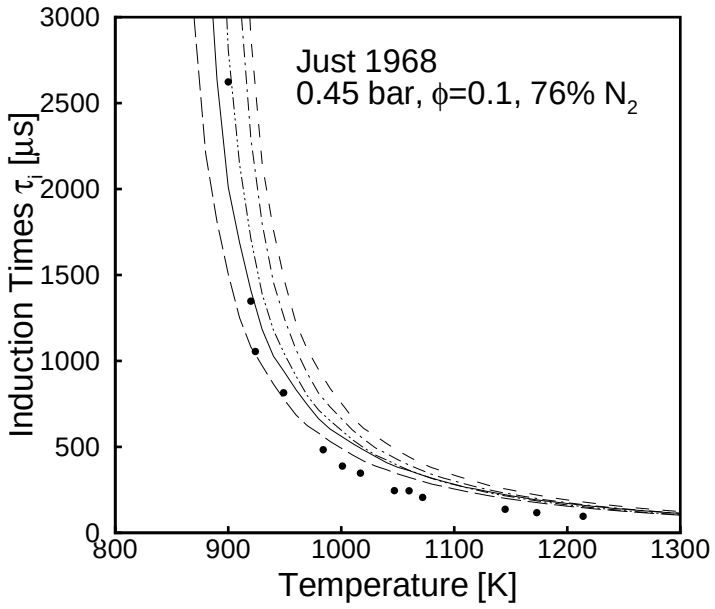

Figure 2.2 Variation with temperature of the induction time as obtained from detailed-chemistry numerical calculations; solid curves: present mechanism (2006) [56], short-dashed curves: Maas and Warnatz (1988) [42], long-dashed curves: Glarborg et al. (1998) [51], dot-dashed curves: GRI mechanism 3.0 (1995) [46], dot-dot-dashed curves: Allen, Yetter and Dryer. (1995) [49], while the symbols denote the shock-tube experimental results of Just and Schmalz (1968) [20] (p = 0.45 bar, ϕ=0.1).

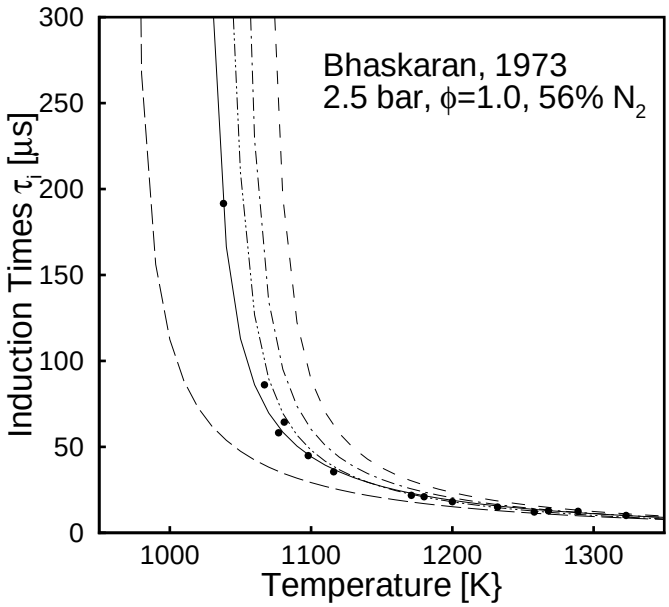

Figure 2.3 Variation with temperature of the induction time as obtained from detailed-chemistry numerical calculations; solid curves: present mechanism (2006) [56], short-dashed curves: Maas and Warnatz (1988) [42], long-dashed curves: Glarborg et al. (1998) [51], dot-dashed curves: GRI mechanism 3.0 (1995) [46], dot-dot-dashed curves: Allen, Yetter and Dryer. (1995) [49], while the symbols denote the shock-tube experimental results of Bhaskaran, Gupta and Just. (1971) [22] (p=2.5 bar, ϕ=1).

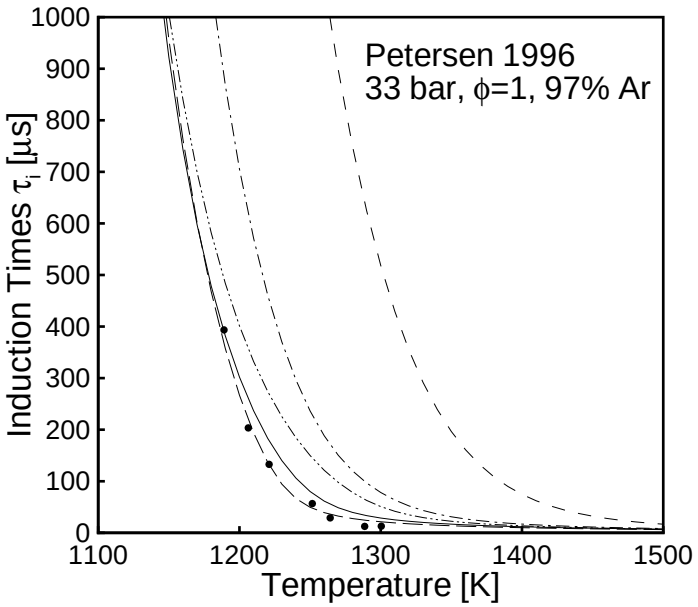

Figure 2.4 Variation with temperature of the induction time as obtained from detailed-chemistry numerical calculations; solid curves: present mechanism (2006) [56], short-dashed curves: Maas and Warnatz (1988) [42], long-dashed curves: Glarborg et al. (1998) [51], dot-dashed curves: GRI mechanism 3.0 (1995) [46], dot-dot-dashed curves: Allen, Yetter and Dryer. (1995) [49], while the symbols denote the shock-tube experimental results of Petersen et al. (1996) [26] (p=33 bar, ϕ=1).

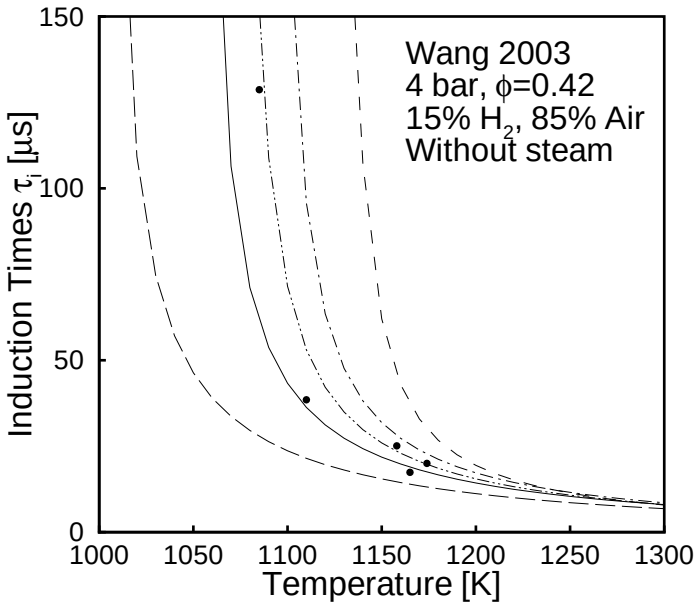

Figure 2.5 Variation with temperature of the induction time as obtained from detailed-chemistry numerical calculations; solid curves: present mechanism (2006) [56], short-dashed curves: Maas and Warnatz (1988) [42], long-dashed curves: Glarborg et al. (1998) [51], dot-dashed curves: GRI mechanism 3.0 (1995) [46], dot-dot-dashed curves: Allen, Yetter and Dryer. (1995) [49], while the symbols denote the shock-tube experimental results of Wang, Olivier and Gronig. (2003) [27] (p=3-5 bar, ϕ=0.42, without steam).

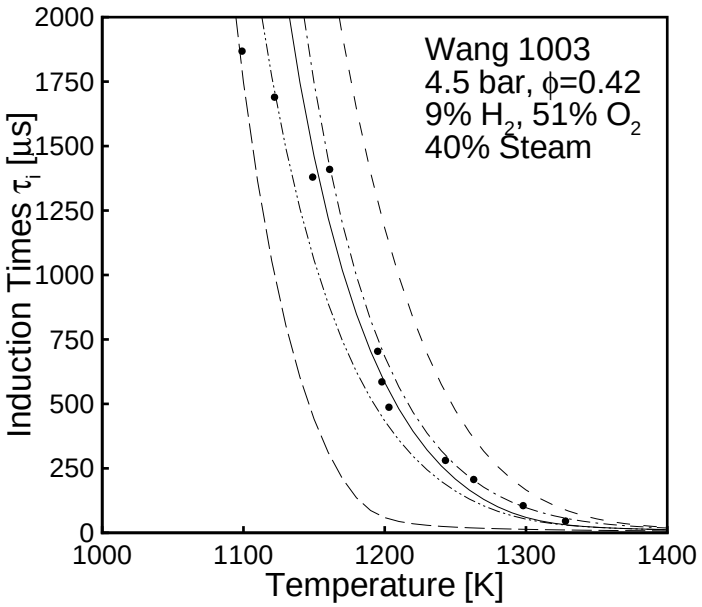

Figure 2.6 Variation with temperature of the induction time as obtained from detailed-chemistry numerical calculations; solid curves: present mechanism (2006) [56], short-dashed curves: Maas and Warnatz (1988) [42], long-dashed curves: Glarborg et al. (1998) [51], dot-dashed curves: GRI mechanism 3.0 (1995) [46], dot-dot-dashed curves: Allen, Yetter and Dryer. (1995) [49], while the symbols denote the shock-tube experimental results of Wang, Olivier and Gronig. (2003) [27] (p=3-5 bar, $\phi = 0.42$, 40% steam).

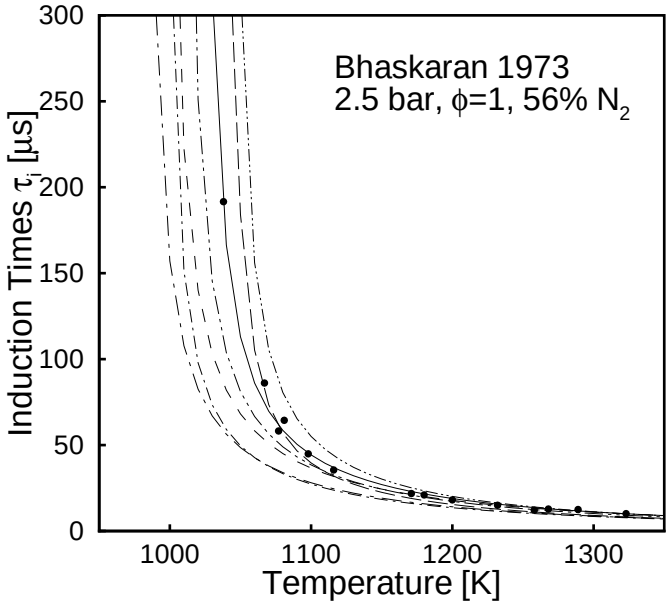

Figure 2.7 Variation with temperature of the induction time as obtained from detailed-chemistry numerical calculations; solid curve: present mechanism (2006) [56], short-dashed curve: GRI mechanism 2.11 [46], log-dash curve: Ranzi et al (1995) [47], long-dot-dashed curve: Marinov, Westbrook and Pitz. (1996) [48], short-dot-dashed curve: Miller and Bowman (1989) [43], short-dash-dot-dot curve: Lindstedt and Skevis (1997) [50], long-dash-dot-dot curve Tan et al (1994) [45], while the symbols denote the shock-tube experimental results of Bhaskaran, Gupta and Just (1971) [22] (p=2.5 bar, ϕ=1).

performed very well under all conditions addressed, as well as or better than the mechanisms of Mueller, Yetter and Dryer [52] (which performed very much like the mechanism of Allen, Yetter and Dryer [49], not shown) and of Saxena and Williams [56], so that, for best agreement with these experiments, any one of these three mechanisms can be employed. Where mechanisms do not work so well discrepancies probably mainly reflect deficiencies in certain rate parameters.

2.3 Concluding Remarks

Although different hydrogen-oxygen-inert chemical-kinetic mechanisms give noticeably different ignition times in the vicinity of crossover, their predictions tend to agree at higher temperatures. Three mechanisms are now available that yield good agreement with all of the existing shock-tube ignition-time data. These mechanisms seem likely to be reliable for temperatures above about 1000 K and pressures below about 50 bar. It would be of interest to obtain experimental ignition-time results for pressures above 50 bar at varying degrees and types of dilution to test predictions of the mechanisms under extreme conditions.

Chapter 3

Isothermal Approximation to the Induction Time of H_2-O_2 Branched-Chain Explosions

Through numerical calculations for isobaric, homogeneous and adiabatic hydrogen-air mixtures it is shown that the detailed chemistry can be reduced to only five elementary steps for determining induction times over the range of conditions addressed. From these five steps, an analytical expression for ignition time is derived which agrees well with computational results concerning dependence on pressure, temperature and composition. It is shown that O and OH maintain steady states during ignition for stoichiometric and fuel-rich mixtures, while H maintain a steady state for sufficiently fuel-lean conditions. Simple asymptotic formulas for the induction times are derived for these two limits which demonstrate the limiting effect of O_2 under rich conditions and of H_2 under lean conditions. These formulas are combined in an approximate way to obtain an expression for the ignition time that can be used for all equivalence ratios

3.1 The Five-step Short Mechanism

The detailed reaction mechanism of Table 2.1 comprises 21 reversible reactions among 8 species, including as intermediates H,OH,O,HO_2 and H_2O_2. Because of the low radical concentrations, however, only five elementary steps suffice to describe accurately the induction period over a wide range of conditions, as was found by comparing ignition times calculated with various degrees of reactions. Table 3.1 lists these five steps, all of which are irreversible.

Table 3.1 The five-step short mechanism and corresponding rates in Table 2.1.

Number	Reaction	Step in Table 2.1
1	$H_2 + O_2 \rightarrow HO_2 + H$	step 12 backward
2	$H + O_2 \rightarrow OH + O$	step 1 forward
3	$H_2 + O \rightarrow OH + H$	step 2 forward
4	$H_2 + OH \rightarrow H_2O + H$	step 3 forward
5	$H + O_2 + M \rightarrow HO_2 + M$	step 9 forward

It may be noted that this mechanism does not consider HO_2 consumption, which may introduce small inaccuracies in induction times very close to crossover [13], and it does not involve H_2O_2 at all. The origin of the rate data for the chain-carrying steps, 2, 3 and 4 and the recombination step 5 in Table 3 is discussed in Chapter 2. Only one initiation step (step 1 in Table 3.1) is included in the short mechanism, while others that are much slower, such as the disotiation reaction H_2 + M $\rightarrow$ 2H + M, are neglected. Previous theoretical investigations of hydrogen-oxygen ignition with reduced chemistry use different initiation reactions. The reaction H_2+O_2 $\rightarrow$ HO_2+H was preferred by Just and Schmalz [20] and by Treviño [33], while the reaction H_2+O_2 $\rightarrow$ 2OH was selected by Schott and Kinsey [7], by Asaba, Gardiner and Stubbeman [11] and by Craig [17]. Only the early investigation of Kushida [32] uses both initiation reactions.

Figure 3.1 compares products of ignition times with oxygen concentration predicted by this short mechanism with those obtained from the detailed mechanism at temperatures above crossover for stoichiometric hydrogen-air mixtures at

different pressures and for hydrogen-air mixtures at atmospheric pressure with different equivalence ratios. The calculations were performed numerically employing the temperature-inflection criterion.

The agreement is seen to be excellent, except very near crossover at pressures of 10 bar and above, for very high initial temperatures at low and moderate pressures and for very lean conditions. Near crossover, reactions involving consumption of HO_2 become important, having an exothermic overall effect which shorten the induction period. This effect is enhanced at higher pressure as the HO_2 production increases through the recombination reaction $H+O_2+M \rightarrow HO_2+M$. The limiting concentration of H_2 for very lean mixtures (equivalence ratios close to 0.1) causes the reaction $H+O_2 \rightarrow O+OH$ to be the fastest in the branching steps with subsequent significant net production of both OH and H radicals, higher temperatures increasing this effect. Consequently, the chain-breaking reactions $OH+OH \rightarrow H_2O+O$ and $H+OH+M \rightarrow H_2O+M$ (only included in the detailed chemistry) become important, therefore delaying ignition. These chain-breaking reactions are not present in the short mechanism, which gives shorter ignition times than the corresponding to detailed chemistry. It can be seen in Fig. 3.1b that for hydrogen-air mixtures at P=1 bar, $\phi = 0.1$ and temperatures above 1500K, numerical calculations with the five-step mechanism failed to determine ignition times with temperature-inflection criterion (dashed curves). Under these conditions, the endothermicity of the dominant branching reaction $H+O_2 \rightarrow O+OH$ makes the overall short mechanism endothermic and the temperature to decrease during the induction period. Using partial equilibrium of this reaction to determine numerically the end of the induction period with the five-step mechanism and for the same conditions results in the dash-dot curve of Fig 3.1b. Employing both criteria, temperature-inflection and partial equilibrium of the reaction $H+O_2 \rightarrow O+OH$, with the short mechanism gives almost the same values for the ignition time, but shorter than the values obtained using temperature-inflection with detailed chemistry, mainly because of the effect of the chain-breaking reac-

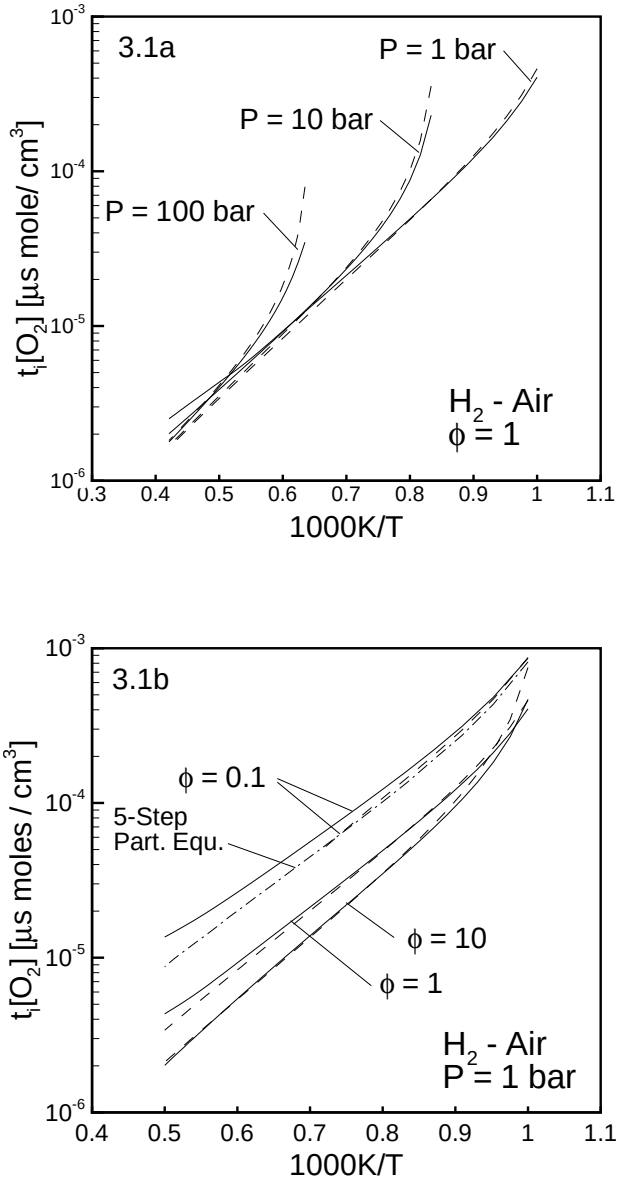

Figure 3.1 Numerical calculations of $t_i[O_2]$ with the detailed chemistry (solid curves) and with the five-step short mechanism (dashed curves), a: for stoichiometric hydrogen-air mixtures at different values of pressure (p = 1,10,100 bar), b: for hydrogen-air mixtures of different equivalence ratios ($\phi = 0.1, 1, 10$) at atmospheric pressures.

tions OH+OH→H_2O+O and H+OH+M→H_2O+M.

Estimates were made of the range of conditions over which this five-step short mechanism is reasonably accurate. The results are shown in a pressure-temperature diagram in Fig. 3.2. The boundaries of this diagram, which are not

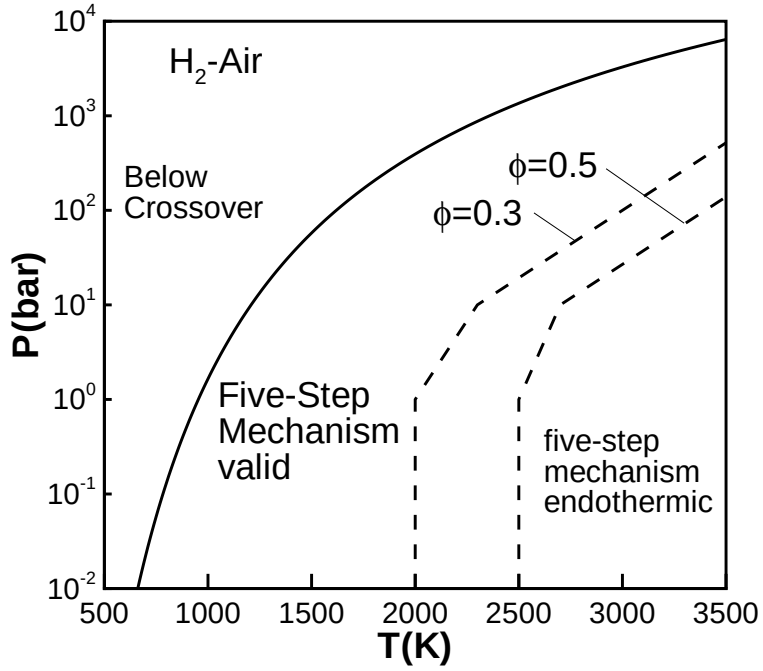

Figure 3.2 Estimated region of validity of the five-step short mechanism for hydrogen-air systems, shown in a pressure-temperature plane for two different equivalence ratio.

extremely accurate, are indications of where temperature-inflection ignition times predicted by the detailed and short mechanisms differ by about ten percent. The solid line representing the low-temperature, high-pressure boundary is the crossover curve; it corresponds approximately to the second explosion limit and, although it is shown only for stoichiometric hydrogen-air systems, it is not greatly modified (changes in pressure less than 50% at any given temperature) for pure hydrogen-oxygen systems or at great excess of argon dilution. In addition to this low-temperature limit, there is a high-temperature limit for lean mixtures ($\phi \leq 0.5$),

above which the five-step mechanism become endothermic overall because of the dominant effect of the branching reaction $H+O_2 \rightarrow O+OH$. Beyond this limit, the criteria of temperature inflection and thermal runaway becomes irrelevant to determine ignition. Figure 3.2 shows that this temperature-limit is pressure-independent below approximately 1 bar, but increase with increasing pressure because of the exothermic recombination reaction $H+O_2+M \rightarrow HO_2+M$ becomes important. The region of applicability narrows with decreasing the equivalence ratio. Between the low and high-temperature limits, as pressure is decreased, the three-body recombination step $H+O_2+M \rightarrow HO_2+M$ becomes relatively less important, the exothermic bimolecular branching alone contributing more to ignition, but the five-step mechanism remains an excellent approximation to the detailed mechanism between 1000K and 2000K for predicting induction times based on thermal runaway. This was verified computationally by calculating ignition times with both mechanisms for pressures all the way down to 10^{-10} bar, where the ignition time at 2000K is 3×10^4s, nearly ten hours, for example. For very high temperatures (T>5000K) the hydrogen dissociation reaction $H_2+M \rightarrow 2H+M$ becomes important; it depends on equivalence ratio (as well as on dilution) because the collision involves H_2 with any molecule, not only with O_2. At even higher temperatures oxygen dissociation becomes a contributing initiation step as well. This limit are not shown in Fig. 3.2 as it is beyond the conditions encountered in practical applications. The five-step mechanism thus enjoy a very wide range of applicability except for very lean mixtures.

3.2 Nondimensional Formulation of the Ignition Problem

The temperature increment and the reactant consumption occurring during the induction period are small and therefore are neglected here when writing the evolution equations for the radicals [11,66]. The dimensionless radical-evolution equations can be expressed as

$$\frac{dy_H}{d\tau} = -(c + 1/2)y_H + y_O + y_{OH} + \nu, \tag{3.1}$$

$$\frac{dy_O}{d\tau} = \frac{\phi}{\kappa_O}(y_H/2 - y_O), \tag{3.2}$$

$$\frac{dy_{OH}}{d\tau} = \frac{\phi}{\kappa_{OH}}(y_H/2 + y_O - y_{OH}), \tag{3.3}$$

corresponding to the five-step short mechanism defined above. In this formulation, $\phi = c_{H_2}/2c_{O_2}$ represents the equivalence ratio of the mixture, with c_{H_2} and c_{O_2} denoting the initial concentrations of hydrogen and oxygen. Use is made of the characteristic branching time of step 2 to define the dimensionless time $\tau = 2k_2c_{O_2}t$. Correspondingly, the reaction rates enter in the formulation through the ratios $\nu = k_1/k_2$, $c = k_5c_M/2k_2$, $\kappa_O = k_2/k_3$ and $\kappa_{OH} = k_2/k_4$, where c_M denotes the effective third-body concentration. Also, the radical concentrations have been scaled according to $y_H = 2c_H/c_{H_2}$, $y_O = c_O/(\kappa_O c_{O_2})$ and $y_{OH} = c_{OH}/(\kappa_{OH}c_{O_2})$.

The variations with temperature of the reaction-rate parameters are shown in Fig. 3.3, which also shows the equilibrium constant K_2 of reaction 2, to be used below when defining the induction time. As can be seen in Fig. 3.3a, the radical-recombination parameter c is a decreasing function of the temperature that increases linearly with pressure. The value $c = 1$ defines the crossover temperature, below which ($c > 1$) chain branching cannot occur because all the H produced in the branching mechanism is consumed faster through recombination when $c > 1$. This can be inferred, for example, by putting the time derivatives equal to zero in the equations; there are slow-reaction solutions to the resulting algebraic equations for y_H, y_O and y_{OH} if $c > 1$ but not for $c < 1$ since negative radical concentrations are then obtained. The initiation-to-branching ratio ν is always extremely small for all temperatures of practical interest.

Integration of the linear equations (3.1)-(3.3) with initial conditions $y_H = y_O = y_{OH} = 0$ at $\tau = 0$ provides the evolution of the radical pool. The initiation term control the initial radical growth, giving scaled radical concentrations that reach small values of order ν for τ order unity. For $\tau \gg 1$, initiation is no longer

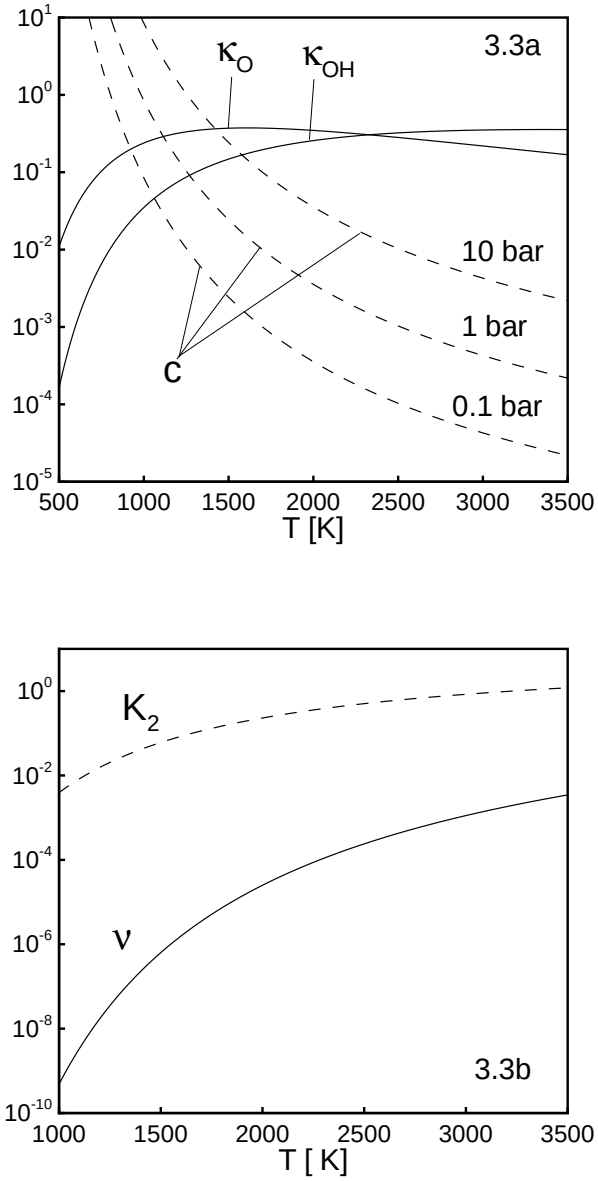

Figure 3.3 Variation with temperature of a: the dimensionless parameters c (dash curves for different pressures), κ_O and κ_{OH} (solid curves) and b: the equilibrium constant K_2 (dashed curve) and the dimensionless parameter ν (solid curves).

important, and the radical concentrations continue to grow exponentially in time in a chain-branching process. Reactant consumption and radical-radical reactions, e.g., the reverse of the shuffle reactions 2-4, become important only at the end of the induction period, causing the radical concentrations to reach a maximum value. In computing the induction time from the integration of equations (3.1)-(3.3) one has to introduce a threshold value for the radical concentrations at ignition. Since the radical concentrations increase exponentially in time, the resulting induction time does not depend strongly on this arbitrary selection. In the analytical development, ignition is identified as the instant when, with the radical concentration obtained from (3.1)-(3.3), the branching reaction 2 reaches partial equilibrium, which corresponds to

$$y_O y_{OH}/y_H = K_2\phi/(\kappa_O\kappa_{OH}). \tag{3.4}$$

3.3 Derivation Of The Formula For The Induction Time

The linear equations (1)-(3) can be solved exactly for $Y = (y_H, y_O, y_{OH})$ as a combination of the particular solution

$$Y_P = (-\frac{\nu}{1-c}, -\frac{1}{2}\frac{\nu}{1-c}, -\frac{\nu}{1-c}) \tag{3.5}$$

with the general solution to the homogeneous system $\sum_{i=1,3} A_i Y_i exp(\lambda_i \tau)$, where λ_i are the roots of the characteristic equation

$$\lambda^3 + [(c+1/2) + \frac{\phi}{\kappa_O\kappa_{OH}}(\kappa_O + \kappa_{OH})]\lambda^2 + \frac{\phi}{\kappa_O\kappa_{OH}}[c(\kappa_O + \kappa_{OH}) + \phi]\lambda -$$
$$\frac{\phi^2}{\kappa_O\kappa_{OH}}(1-c) = 0. \tag{3.6}$$

Here Y_i are their associated eigenvectors, and the constants A_i are determined from imposing the initial (null) conditions upon $Y_P + \sum_{i=1,3} A_i Y_i$. Only one of the roots of equation (3.6) is real and positive, λ_1, the other two being complex conjugates

with negative real parts. Therefore for large τ the solution can be expressed as $A_1 Y_1 exp(\lambda_1 \tau)$.

The solution of the cubic equation (3.6) for λ_1 is

$$\lambda_1 = \left(r + \sqrt{q^3 + r^2}\right)^{1/3} + \left(r - \sqrt{q^3 + r^2}\right)^{1/3} - a_2/3, \tag{3.7}$$

where

$$q = a_1/3 - a_2^2/9, \qquad r = (a_1 a_2/3 - 3a_0)/6 - a_2^3/27, \tag{3.8}$$

with a_i representing here the coefficient multiplying the i-th power of λ in equation (3.6). The corresponding eigenvector can be written as $Y_1 = (1, Y_O, Y_{OH})$, where

$$Y_O = \frac{\phi}{2(\phi + \kappa_O \lambda_1)}, Y_{OH} = \frac{\phi(2\phi + \kappa_O \lambda_1)}{2(\phi + \kappa_O \lambda_1)(\phi + \kappa_{OH} \lambda_1)}. \tag{3.9}$$

The associated multiplying constant becomes

$$A_1 = \frac{-\left[\nu/(1-c)\right](P + Q/2 - 1)}{Y_{OH} - Y_O Q + P} \tag{3.10}$$

with

$$P = \frac{(\phi^2/2)\,(2\kappa_{OH}/\kappa_O - 1)}{(\phi + \lambda_R \kappa_{OH})^2 + (\lambda_I \kappa_{OH})^2} \tag{3.11}$$

and

$$Q = \frac{(\kappa_{OH}/\kappa_O)\left[(\phi + \lambda_R \kappa_O)^2 + (\lambda_I \kappa_O)^2\right] + \phi \lambda_R \kappa_{OH} + \phi^2\,(1 + \kappa_{OH}/\kappa_O)}{(\phi + \lambda_R \kappa_{OH})^2 + (\lambda_I \kappa_{OH})^2}, \tag{3.12}$$

where $\lambda_R = -\lambda_1/2 - a_2/3$ and $\lambda_I = (\sqrt{3}/2)\left[\left(r + \sqrt{q^3 + r^2}\right)^{1/3} - \left(r - \sqrt{q^3 + r^2}\right)^{1/3}\right]$, in which λ_R and λ_I represent the real and imaginary parts of the roots for which λ is complex. From equation (3.4), this leads to the expression

$$t_i = \frac{1}{2 k_2 c_{O_2} \lambda_1} \ln\left(\frac{K_2 \phi}{\kappa_O \kappa_{OH}} \frac{1}{Y_O Y_{OH} A_1}\right) \tag{3.13}$$

for the induction time, which was used to generate the dashed curves in Fig. 3.4. The dashed curves are nearly undistinguishable from solid curves, which represent the full numerical solution obtained using equations (3.1)-(3.4).

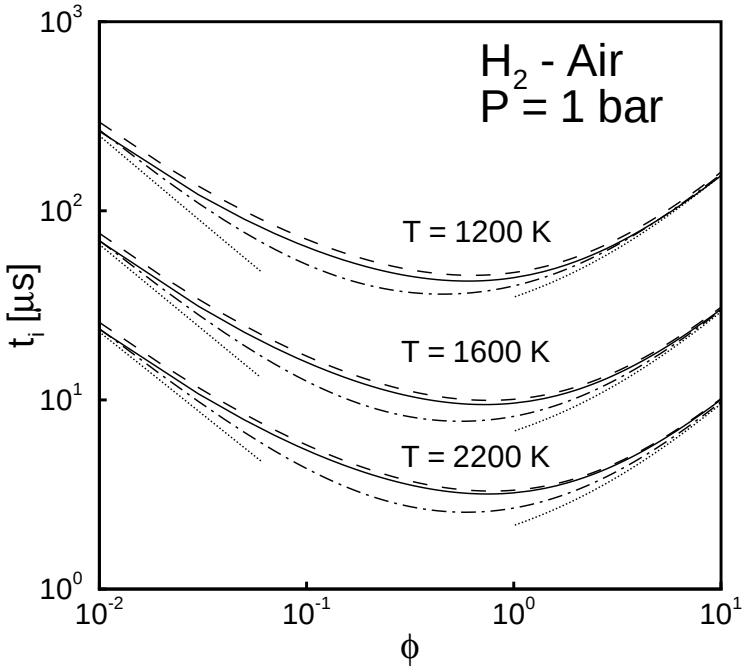

Figure 3.4 The induction time at atmospheric pressure for three different temperatures as obtained a: from numerical integration of the equations (3.1)-(3.4) (solid curves), from evaluation of the approximate solution to (3.1)-(3.3) given in equation (3.13) (dashed curves), from evaluations of the asymptotic predictions given in equations (3.14) and (3.16) (dotted curves) and from evaluation of the ad-hoc approximation given in equation (3.17) (dash-dotted curves).

3.4 Asymptotic Approximations For The Induction Time For Rich And Lean Limits

As previously indicated, simplified expressions for t_i can be sought in the limit of rich and lean mixtures. For $\phi \gg 1$, one can in principle construct the solution by introducing expansions for A_1, Y_1 and λ_1 in inverse powers of ϕ and by solving the resulting problems arising at each order in a sequential manner. The leading-order solution of such as asymptotic analysis turns out to be equivalent to introducing steady-state assumptions for the radicals O and OH, which corresponds to taking the limit $\phi \to \infty$ in equations (2) and (3) to give $y_O = y_H/2$ and $y_{OH} = y_H + \nu_2$. Using these steady-state expressions in equation (3.1) yields $dy_H/d\tau = (1-c)y_H + \nu$, which can be easily integrated to give $y_H = [\nu/(1-c)]exp[(1-c)\tau]$ for $\tau \gg 1$. Substituting these results into equation (3.4) gives

$$t_R = \frac{1}{2k_2 c_{O_2}(1-c)} \ln\left(\frac{2K_2\phi}{\kappa_O \kappa_{OH}} \frac{1-c}{\nu}\right) \tag{3.14}$$

for the induction time of rich mixtures. As seen in the first multiplying factor, the oxidizer is the limiting reactant in this case. Early predictions for induction times exhibited this same dependence regardless of the initial mixture composition. We shall see below that O_2 is no longer the limiting reactant in sufficiently fuel-lean mixtures.

Equation (3.14) is tested in Fig. 3.4, giving results in close agreement with the exact solution for $\phi \geq 1$. It can be concluded that the smallness of the parameters κ_O and κ_{OH} helps to extends the validity of the steady-state assumptions for O and OH all the way to stoichiometric mixtures. It is worth mentioning that the leading-order results were carried on to a higher order following the asymptotic procedure outlined above. It was found that the higher-order corrections, which included two additional terms in the expansion for λ_1, do not improve the accuracy near stoichiometric conditions, and they only improve the agreement marginally for $\phi \gg 1$, indicating that the leading-order prediction given in equation (3.14)

yields the best compromise between simplicity and accuracy.

The analysis of the limiting case $\phi \ll 1$ is somewhat more involved than that previously indicated for $\phi \gg 1$. One could construct the solution by using asymptotic expansions in powers of ϕ. The leading-order solution of such a development is in this case equivalent to introducing a steady-state assumption for H. To see this more clearly, it is convenient to rewrite (3.1)-(3.3) in terms of the alternatively dimensionless time $\bar{\tau} = \phi\tau = c_{H_2}k_2t$. Taking then the limit $\phi \to 0$ in the modified equation for H yields the steady-state expression $y_H = (y_O + y_{OH} + \nu)/(c + 1/2)$. Substituting then this result into the conservation equations for O and OH and integrating gives $y_O = (\nu/4)(1+\sqrt{2\kappa_{OH}/\kappa_O})exp(\lambda_1\bar{\tau})$ and $y_{OH} = \sqrt{2\kappa_O/\kappa_{OH}}y_O$ for $\bar{\tau} \gg 1$, where

$$\lambda_1 = \frac{\left[(2(1+c) - 4c^2)\,\kappa_O\kappa_{OH} + c^2(\kappa_O + \kappa_{OH})^2\right]^{1/2} - c(\kappa_O + \kappa_{OH})}{\kappa_O\kappa_{OH}(1+2c)}. \tag{3.15}$$

Introducing these results into (3.4) gives

$$t_L = \frac{1}{k_2c_{H_2}\lambda_1}\ln\left(\frac{2K_2\phi}{\kappa_O\kappa_{OH}}\frac{4}{\nu}\frac{1+\sqrt{\kappa_{OH}/2\kappa_O}}{1+\sqrt{2\kappa_{OH}/\kappa_O}}\right) \tag{3.16}$$

for the induction time of lean mixtures. The factor multiplying the logarithm, which further reduces to $\left(c_{H_2}\sqrt{2k_3k_4}\right)^{-1}$ when $c \ll 1$, now contains $c_{H_2}^{-1}$, indicating that the fuel becomes the limiting reactant for lean mixtures. This dependence of the induction time in lean mixtures was already pointed out by Miyama and Takayama (1965), although these authors attributed the resulting behavior to the existing low temperature rather than to the fuel-lean conditions used in their experiments. The accuracy of equation (16) is tested in Fig. 3.4. The results show reasonable agreement for $\phi \leq 0.07$, while for values of ϕ close to unity the steady-state assumption for H clearly fails. As before, a correction of order ϕ was incorporated in the expression for to extend the validity of the approximation, but no significant improvement was seen to follow from asymptotic development.

The formulas in equations (3.14) and (3.16) are expressed in dimensional forms in the appendix, where further discussion of the results may be found.

3.5 An Ad Hoc Approximation For The Induction Time

Figure 3.4a indicates that in the intermediate range $0.07 \leq \phi \leq 1$ all three radical are out of steady state. The corresponding induction time evolves from the fuel-limited value (3.16) corresponding to lean mixtures to the oxidizer-limited solution of rich mixtures given in (3.14). The exact solution given in (3.7)-(3.13) is in principle necessary to compute this transition. Nevertheless, the sum,

$$t_i = t_L + t_R, \tag{3.17}$$

provides results that are correct to within a factor of two over the entire range of equivalence ratios, as may be seen from Fig. 3.4. The appendix summarizes expressions for t_L and t_R in physical variables.

3.6 Comparisons Of The Approximate Solutions With Predictions Of Detailed Chemistry

Induction times at atmospheric pressure, obtained from equations (3.1)-(3.4), are compared in Fig. 3.5 with those obtained from the detailed chemistry. In computations with detailed chemistry addressing achievement of partial equilibrium, a factor 0.95 was placed on the right hand side of equation (3.4), corresponding to 95% of partial equilibrium of reaction 2. As seen in Fig. 3.5, this selection gives values of the induction time near those obtained from equation (3.13). If complete partial equilibrium is employed, the prediction of the induction time is too large by an amount that increases with increasing equivalence ratio and temperature. For lean mixtures the overprediction is small (20-50%) for all temperatures. However, for stoichiometric and rich mixtures the values for the

induction time obtained by considering complete partial equilibrium are overpredicted roughly by a factor of ten for temperatures above 2000K. For very rich mixtures ($\phi \geq 10$) a complete partial equilibrium is not reached according to the detailed chemistry. The reason that equation (3.4) works for the short mechanism but requires modification for the detailed mechanism is that the latter includes reverse shuffle reactions, which become significant and delay achievement of partial equilibrium as it is approached.

Also shown in Figure 3.5 is the prediction of the detailed chemistry employing the inflection-point criterion. This prediction applies only for $0.1 \leq \phi \leq 10$; beyond this range, the rate of heat release is very small or negative so that the temperature-inflection criterion become irrelevant and would give misleading results. It is seen in Fig. 3.5 that when the temperature inflection criterion is used, there is generally reasonable agreement, except for very lean or very rich mixtures and for very high temperatures, indicating that the short mechanism, the criterion (3.4) and the assumptions of negligible reactant consumption and heat release are all appropriate for computing induction times under most conditions. The discrepancies found between the predictions of the detailed-chemistry with the temperature-inflection criterion and the values given by Eq. (3.13) for very lean mixtures are associated with the non-negligible reactant consumption and the chain-breaking effect of the reactions OH+OH$\rightarrow$$H_2O$+O and H+OH+M$\rightarrow$$H_2O$+M, both introducing an additional delay. For very rich mixtures, the shuffle reactions 3 and 4 are much faster than reaction 2, therefore temperature inflection occuring earlier than partial equilibrium of reaction 2 by as much as a factor of two at the higher temperatures. The largest discrepancies are found for very high temperatures (T>2000K). Two different curves obtained with the inflection-point criterion are represented in Fig. 3.5 for T= 2200K. The curve coming from the rich side represents a maximum of heat release associated to the recombination reaction H+O_2+M $\rightarrow$ HO_2+M. The curve coming from the lean side represents another maximum of heat release, occuring later than

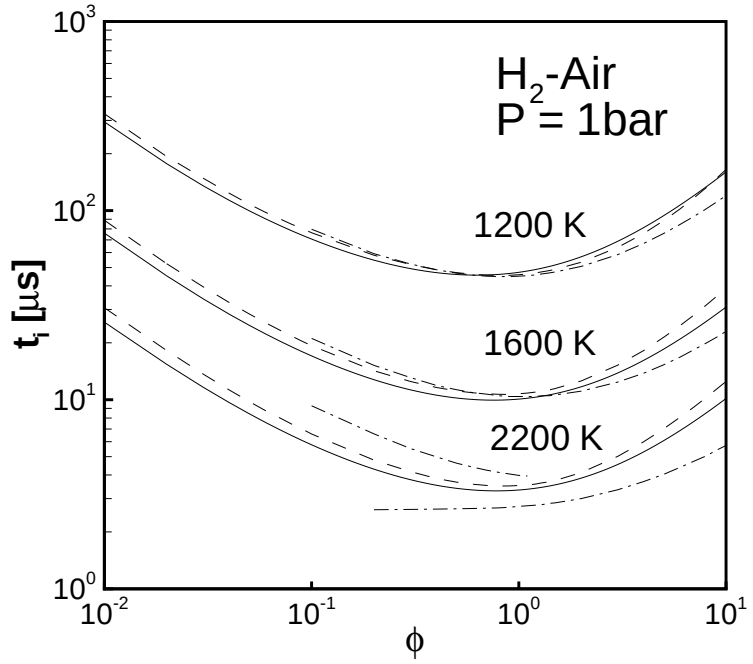

Figure 3.5 The induction time at atmospheric pressure for three different temperatures as obtained from numerical integration with the detailed chemistry using 95% partial equilibrium for the reaction $H+O_2 \rightleftharpoons O+OH$ (dash curves) and the inflection point for temperature(dash-dotted curves) and from evaluation of the approximate solution to (3.1)-(3.3) given in equation (3.13) (solid curves).

the previous one, associated with the exothermicity of the recombination reaction H+OH+M→H_2O+M and the chain-breakinh reaction OH+OH→H_2O+O. It can be seen in Fig. 3.5 that both curves overlapped for equivalent ratios between 0.2 and 0.9, indicating that the rate of heat release exhibits two peaks under these conditions. Nevertheless, equation (3.13) gives the induction time with generally acceptable accuracy over most of the intermediate range of ϕ and temperatures below 2000K, corresponding to flammable or detonable mixtures.

3.7 Concluding Remarks

Above crossover temperatures, a very simple five-step elementary mechanism has been identified and its validity has been evaluated over a wide range of conditions of temperature, pressure and composition. This short-mechanism describes the autoignition well above equivalence ratios above about 0.1, at temperatures between the crossover limit and about 2000K, and below about 10 bar, which represent the range of conditions encountered in practical applications. This mechanism, which also works well at higher pressures away from crossover, provides the basis for an analytic development that neglects heat release and reactant consumption prior to ignition and that invokes achievement of partial equilibrium of the step $H + O_2 \rightarrow OH + O$ as an ignition criterion. With these approximations, an explicit ignition-time formula can be derived, which in turn can be greatly simplified through leading-order asymptotic expansions for large and small equivalence ratios. The good agreement of these analytical results with ignition-time predictions of detailed chemistry emphasizes how simple and comprehensible hydrogen-oxygen autoignition is under these conditions. The resulting ignition-time formulas, which were not previously available, can be used in future autoignition applications.

Chapter 4

The Induction Time of Branched-Chain Thermal Explosions

An asymptotic analysis for high activation energy of the branching step is developed for predicting ignition times of branched-chain explosions on the basis of a criterion of thermal runaway in homogeneous, isobaric, adiabatic systems. The chemistry includes an initiation step, a branching step and a recombination step and leads to a nonlinear second-order ordinary differential equation for the temperature as a function of time under adiabatic conditions. One or both of the branching and recombination steps must be exothermic, while the initiation step may be endothermic or exothermic. A two-term expansion is derived in a small parameter representing the ratio of the initiation rate to the branching rate, yielding explicit expressions for the ignition time. At leading order, the ignition time is found to be inversely proportional to the net branching rate, the proportionality constant being the logarithm of the ratio of the branching rate to the initiation rate multiplied by energetic and rate parameters associated with branching and recombination. Resulting ignition times are shown to correspond closely with those calculated by numerical integration of the full equations on the basis of a

temperature-inflection criterion, except near crossover, where the branching rate equals the recombination rate. Application to the theory to fuel-rich hydrogen-oxygen systems demonstrates good agreement.

4.1 The Model Problem

Consider a homogeneous, adiabatic, isobaric system experiencing the two-steps chemical process

$$\mathrm{F} + \mathrm{O} \rightarrow \mathrm{P} + \mathrm{X}, \qquad \mathrm{X} \rightarrow \mathrm{P}, \tag{4.1}$$

where F denotes fuel, O oxidizer, P collections of products and X an active species such that the rates of both steps increase with increasing concentration of X, the mole fraction of which is denoted by X. The rate of the first step divided by the total number of moles of the mixture (assumed constant) is written as $A + BX$, where $A = A_0 \exp(T_i/T_0 - T_i/T)$ and $B = B_0 \exp(T_a/T_0 - T_a/T)$ are reciprocal times, the first measuring the initiation rate and the second the branching rate. Here T denotes temperature, T_0 is the initial temperature, T_a the activation temperature for branching and T_i the activation temperature for initiation. Both A_0 and B_0 are constants during ignition, although in general they depend on T_0, pressure and the initial composition of the system. The rate of the second step divided by the total number of moles of the mixture is written as cB_0X, where c is the ratio of the recombination rate to the branching rate at the initial temperature, a constant that also depends on T_0, pressure and the initial composition. A pressure-dependent crossover temperature is defined by putting $c = 1$; below this temperature, a branched-chain explosion cannot occur because the rate of radical removal exceeds the rate of radical production, and somewhat above this temperature typically $c \ll 1$, because of the strong temperature dependence of the branching rate.

Initiation is usually endothermic, and its heat absorbed per mole of oxidizer consumed divided by the heat capacity per mole of mixture (assumed con-

stant) is denoted here by q_i. Branching and recombination steps are assumed to be exothermic, and their heat released per mole of oxidizer consumed, divided by the heat capacity per mole of mixture are denoted by q_b and q_r, respectively. These definitions enable conservation of energy to be written as

$$\frac{dT}{dt} = -q_i A + q_b BX + q_r cB_0 X, \tag{4.2}$$

t denoting time. The equation for conservation of the active species is

$$\frac{dX}{dt} = A + BX - cB_0 X. \tag{4.3}$$

Initial conditions for Eqs. (4.2) and (4.3) at $t = 0$ are $T = T_0$ and $X = X_0$, the latter generally taken to be zero since the initiation serves to generate X, removing the necessity of artificially assuming a positive initial radical concentration to enable chemistry to begin.

The relationship of the model problem to a problem with detailed chemistry depends on the chemical system. For fuel-rich hydrogen-oxygen systems there is a good systematically reduced two-step description [39,72,73], based on steady-state approximations for O and OH, that has a branching step $3H_2+O_2 \rightarrow 2H_2O+2H$, principally at the rate of the elementary reaction $H+O_2 \rightarrow OH+O$, followed by a recombination step, $2H \rightarrow H_2$, at the rate of the elementary step $H+O_2+M \rightarrow HO_2+M$. Besides branching and recombination, an initiation step is needed for autoignition in the absence of initial radicals. This result in the model problem addressed here, X representing H, with the branching rate twice that of $H+O_2 \rightarrow OH+O$ and the recombination rate that of $H+O_2+M \rightarrow HO_2+M$, provided that the reactant consumption is neglected. With this correspondence, A is proportional to the product of the concentrations of H_2 and O_2, B_0 is proportional to the concentration of O_2, and c is the ratio of the recombination rate to twice the branching rate, so that it is proportional to pressure away from falloff but independent of the chemical composition except insofar as chaperon efficiencies depend on composition.

It is of interest to compare this model problem with the earlier, simpler model problem [39]. The earlier analysis was more general in the sense that the branching rate was allowed to be proportional to a power of X that could be different from unity. Since that power is generally unity for real branching chemistry, there is little motivation to address this degree of generalization. The previous work did not allow for recombination and thus pertains to the limit $c = 0$ of the present description. In addition, for simplicity, so that it only would be necessary to work with a first-order ordinary differential equation, the earlier study was based on a one-equation model, which in a formal sense implicitly requires initiation to be exothermic with the same heat release as branching ($q_i = -q_b$), a generally unrealistic restriction that nevertheless turns out to be not exceedingly severe since the energetic effect of initiation will be shown here to be unimportant. Equations (2) and (3) imply that, in contrast to the previous model [39], the present study requires consideration of a second-order ordinary differential equation, that is, it is a two-equation model. The previous work [39] also required the initiation rate to be constant, an approximation that will be shown below to apply correctly at $c = 0$ for sufficiently small initiation rates even though the activation energy for this step typically is the largest.

4.2 Formulation for Activation-Energy Asymptotics

In the Frank-Kamenetskii approach [35], to leading order in the small parameter T_0/T_a, the approximations $A = A_0 e^{i\theta}$ and $B = B_0 e^{\theta}$ apply, where $\theta = (T - T_0)T_a/T_0^2$, and $i = T_i/T_a$. The resulting exponential, with reactant consumption neglected, drives the temperature to infinity at a finite time whenever the endothermicity of initiation is unimportant, yielding a thermal runaway that can replace the temperature-inflection criterion for determining an ignition time. These results can be justified by a formal asymptotic expansion in the small parameter T_0/T_a, which underlies the present development. In this approximation,

Eqs. (4.2) and (4.3) become

$$\frac{d\theta}{dt} = -\alpha_i A_0 e^{i\theta} + \left(\alpha_b e^{\theta} + \alpha_r c\right) B_0 X \tag{4.4}$$

and

$$\frac{dX}{dt} = A_0 e^{i\theta} + \left(e^{\theta} - c\right) B_0 X, \tag{4.5}$$

subject to the initial conditions $\theta = 0$ and $X = 0$ at $t = 0$, where the definitions $\alpha_i = q_i(T_a/T_0^2)$, $\alpha_b = q_b(T_a/T_0^2)$ and $\alpha_r = q_r(T_a/T_0^2)$ have been introduced. Use of Eq. (4.4) to eliminate X from Eq. (4.5) gives

$$\frac{d^2\theta}{d\tau^2} = -a\epsilon i e^{i\theta}\frac{d\theta}{d\tau} + \epsilon e^{i\theta}\left(\frac{e^{\theta} + bc}{1 + bc}\right) + (e^{\theta} - c)\left(\frac{d\theta}{d\tau} + a\epsilon e^{i\theta}\right) + \frac{e^{\theta}}{e^{\theta} + bc}\left(\frac{d\theta}{d\tau}\right)\left(\frac{d\theta}{d\tau} + a\epsilon e^{i\theta}\right), \tag{4.6}$$

where the nondimensional time is $\tau = tB_0$, the ratio of the recombination to branching heat release is $b = \alpha_r/\alpha_b$, and the ratio of the heat absorbed in initiation to the heat released in branching and recombination is $a = \alpha_i/(\alpha_b + \alpha_r c)$. A measure of the ratio of the initiation rate to the branching rate,

$$\epsilon = A_0(\alpha_b + \alpha_r c)/B_0, \tag{4.7}$$

is generally small in explosion problems and will be treated as a small parameter in an asymptotic analysis.

4.3 Asymptotic Analysis for Small Initiation Rates

Equation (4.6) is to be solved subject to the initial conditions $\theta = 0$, $d\theta/d\tau = -a\epsilon$ at $\tau = 0$, as an asymptotic expansion for small ϵ. It is convenient to define $f(\theta) = d\theta/d\tau$ and to write Eq. (4.6) in a phase plane,

$$f df/d\theta = -a\epsilon i e^{i\theta} f + \epsilon e^{i\theta}\left(\frac{e^{\theta} + bc}{1 + bc}\right) + (f + a\epsilon e^{i\theta})(e^{\theta} - c) + \frac{e^{\theta}}{e^{\theta} + bc} f(f + a\epsilon e^{i\theta}), \tag{4.8}$$

with $f = -a\epsilon$ at $\theta = 0$. A uniformly valid matched asymptotic expansion of the solution $f(\theta)$ to Eq. (4.8) is to be sought [112,113]. The nondimensionalized ignition time τ_∞, defined as the value of τ at which θ goes to infinity, can be obtained from this solution as

$$\tau_\infty = \int_0^\infty (d\theta/f)\,. \tag{4.9}$$

It is evident that, in addition to its dependence on the expansion parameter ϵ, τ_∞ may depend on the fixed parameters a, b, c and i. To assure that thermal runaway occurs on the time scale τ, attention is restricted here to nonnegative values of b, to values of a and i of order unity or smaller, and to $c < 1$, with $1 - c$ of order unity. The appendix addresses the question of what happens as c approaches unity. With this ordering, there is an inner zone near $\theta = 0$ in which appropriate variables are $y = \theta/\epsilon$ and $F = f/\epsilon = dy/d\tau$, both of order unity, as may be inferred from Eq. (4.8) in view of the ϵ in the initial condition for f. For $\epsilon \ll 1$, in these variables Eq. (4.8) becomes

$$FdF/dy = -a\epsilon i(1 + i\epsilon y + ...)F + (1 + \frac{\epsilon y}{1 + bc} + i\epsilon y + ...)$$

$$+(F+a+ai\epsilon y+...)(1-c+\epsilon y+...)+\frac{\epsilon}{1+bc}F(F+a+ai\epsilon y+...)(1+bc\epsilon y+...). \tag{4.10}$$

With the expansion $F = F_0 + \epsilon F_1 + ...$, Eq. (4.10) gives

$$F_0 dF_0/dy = 1 + (1 - c)(F_0 + a), \tag{4.11}$$

with the initial condition $F_0 = -a$ at $y = 0$, and

$$dF_1/dy + F_1[1 + (1 - c)a]/F_0^2 =$$

$$-ai + \frac{y\{1 + i + [F_0 + a + ai(1 - c)](1 + bc)\}}{(1 + bc)F_0} + \frac{F_0(F_0 + a)}{(1 + bc)F_0}, \tag{4.12}$$

with the initial condition $F_1 = 0$ at $y = 0$. The solution to Eq. (4.11), subject to the initial condition, is expressible as

$$\left(\frac{1}{1 - c}\right)^2 \{(1 - c)(F_0 + a) - [1 + a(1 - c)] \ln [1 + (1 - c)(F_0 + a)]\} = y. \tag{4.13}$$

Equation (4.12) is linear and has the solution

$$F_1 = \exp\left[-\int_0^y \frac{1+(1-c)a}{F_0^2}dy\right]\left\{1+\int_0^y \exp\left(\int_0^y \frac{1+(1-c)a}{F_0^2}dy\right)\times\right.$$

$$\left.\left[\frac{y[1+i+(F_0+a)(1+bc)]}{(1+bc)F_0} - \frac{ai(1+bc)F_0+F_0(F_0+a)}{(1+bc)F_0}\right]\right\}. \qquad (4.14)$$

These results show that F_0 approaches $(1-c)y$ as y approaches infinity, while F_1 becomes proportional to y^2 in this limit, explicitly demonstrating the lack of uniform validity of the inner solution.

For θ and f of order unity, the leading-order outer solution to Eq. (4.8), f_0, in the expansion $f = f_0 + \epsilon f_1 + ...$, is obtained by solving the equation

$$f_0 df_0/d\theta = f_0(e^\theta - c) + \frac{e^\theta}{e^\theta + bc}f_0^2. \qquad (4.15)$$

Then

$$f_0 = (e^\theta + bc)\left\{k + \ln\left(e^\theta + bc\right) + \frac{1}{b}\ln\left(\frac{e^\theta + bc}{e^\theta}\right)\right\}, \qquad (4.16)$$

where k is a constant of integration. Matching with the inner solution gives $k = -(1+1/b)\ln(1+bc)$. The composite solution to Eq. (4.8) at leading order then becomes

$$f = \epsilon F_0 + (e^\theta + bc)\left\{\ln\left(\frac{e^\theta + bc}{1+bc}\right) + \frac{1}{b}\ln\left(\frac{1+bce^{-\theta}}{1+bc}\right)\right\} - (1-c)\theta, \qquad (4.17)$$

the last term of which is the common part that matched. The nondimensional ignition time is then recovered from Eq. (4.9) by substituting Eq. (4.17) into the integrand, with F_0 determined by Eq. (4.13).

An asymptotic expansion of τ_∞ for small values of ϵ may be obtained from Eq. (4.17) by breaking the integral in Eq. (4.9) into two parts, $\tau_\infty = \int_0^\delta (d\theta/f) + \int_\delta^\infty (d\theta/f)$, with $\epsilon \ll \delta \ll 1$. To leading order, the first of these integrals is $\int_0^{\delta/\epsilon}(dy/F_0)$, which is found from Eq. (11) to be $(1-c)^{-1}\ln[1+(1-c)(F_0+a)]$, with F_0 evaluated at $y = \delta/\epsilon$. Since δ/ϵ is large, Eq. (4.13) shows that to leading order this result can be written as $(1-c)^{-1}\ln[1+a(1-c)+(1-c)^2\delta/\epsilon]$, which approaches $(1-c)^{-1}\ln[(1-c)^2\delta/\epsilon]$ for large values of δ/ϵ. The second integral to leading

order is $\int_\delta^\infty (d\theta/f_0)$, with f_0 given by Eq. (4.16). Since the resulting integrand approaches $[(1-c)\theta]^{-1}$ as θ approaches zero, there is a divergent contribution of $-(1-c)^{-1}\ln\delta$ from this integral at its lower limit, which cancels the divergent contribution $(1-c)^{-1}\ln\delta$ of the previous integral.

Combining these two results for large values of δ/ϵ in the limit of vanishing δ gives a convergent expression for τ_∞ which can be written as

$$\tau_\infty = \frac{1}{1-c}\ln\left(\frac{1}{\epsilon}\right) + \frac{2}{1-c}\ln(1-c) - K(b,c), \tag{4.18}$$

up to terms of order ϵ, where

$$K(b,c) \equiv \lim_{\delta\to 0}\left\{-\frac{\ln\delta}{1-c} - \int_\delta^\infty \left\{\frac{1}{e^\theta+bc}\left[\ln\left(\frac{e^\theta+bc}{1+bc}\right) + \frac{1}{b}\ln\left(\frac{1+bce^{-\theta}}{1+bc}\right)\right]^{-1}\right\} d\theta\right\}$$

$$= \int_0^\infty \left\{\frac{1}{(1-c)\theta e^\theta} - \right.$$

$$\left.\frac{1}{e^\theta+bc}\left[\ln\left(\frac{e^\theta+bc}{1+bc}\right) + \frac{1}{b}\ln\left(\frac{1+bce^{-\theta}}{1+bc}\right)\right]^{-1}\right\} d\theta + \frac{\gamma}{1-c}. \tag{4.19}$$

The identity $\gamma = \lim_{\delta\to 0}[\ln(\delta^{-1}) - \int_\delta^\infty (\theta e^\theta)^{-1} d\theta]$, where $\gamma = 0.5772$ is Euler's constant, has been employed here to enable $K(b,c)$ to be written as a convergent integral. Numerical evaluation of this integral results in the curves of $K(b,c)$ shown in Fig. 4.1 for finite values of b. It is noteworthy that, to leading order, the value of τ_∞ is independent of the values of the parameters a and i, and the result dimensionally gives the runaway ignition time t_∞ as

$$t_\infty = \frac{1}{B_0(1-c)}\ln\left(\frac{B_0}{A_0(\alpha_b+\alpha_r c)}\right) - \frac{1}{B_0}\left[\frac{2}{(1-c)}\ln\left(\frac{1}{1-c}\right) + K(b,c)\right]. \tag{4.20}$$

4.4 Simplification of Results for Special Cases

It is of interest to consider different limits for the parameters c and b. For hydrogen-oxygen mixtures somewhat above crossover temperatures, branching is much faster than recombination during the induction period, so that $c \to 0$ is a

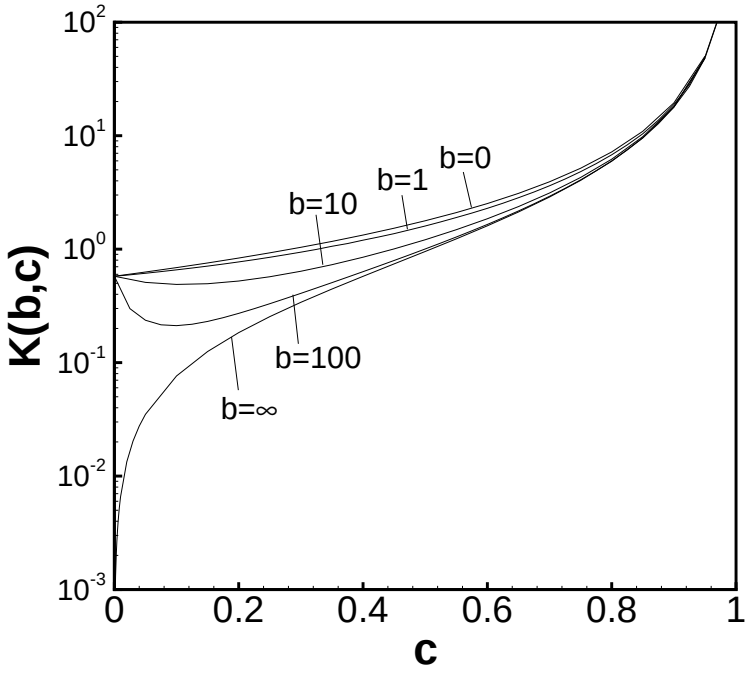

Figure 4.1 The dependency of $K(b, c)$ on c for $b = 0, 1, 10, 100, \infty$, obtained from the last equality in Eq. (4.19) and from Eq. (4.23).

relevant limit. If the ratio of the heat release in recombination to the heat release in branching is high enough that bc may be best assumed not vanish in the limit $c \to 0$, then $\tau_\infty = \ln(1/\epsilon) - K'(bc)$, with

$$K'(bc) = \gamma + \int_0^\infty \left\{ \frac{1}{\theta e^\theta} - \frac{1}{e^\theta + bc} \left[\ln\left(\frac{e^\theta + bc}{1 + bc} \right) \right]^{-1} \right\} d\theta, \tag{4.21}$$

which is plotted in Fig. 4.2. If $bc \to 0$ in the limit $c \to 0$, then heat release by

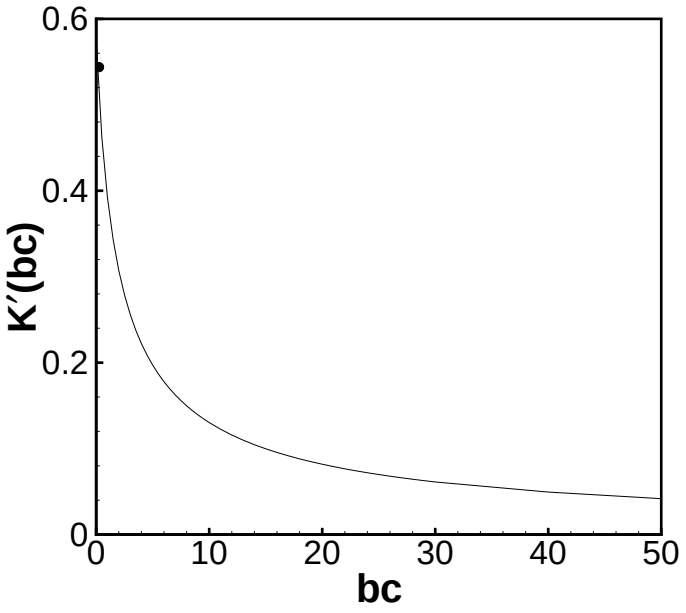

Figure 4.2 The function $K'(bc)$ obtained by evaluating numerically the integral in Eq. (4.21).

recombination prior to ignition becomes negligible as well, and $K' \to \gamma$ so that the expression $\tau_\infty = \ln(1/\epsilon) - \gamma$, obtained previously[9], is recovered. The present analysis thus demonstrates explicitly that, to the order to which the expansion in ϵ was carried, the previous results [39] do not depend on the specific choices made for values of a and i, so long as these parameters are of order unity.

In the limit $b \to 0$, heat release by recombination becomes negligible, but radical depletion remains important. The dimensionless induction time in this limit becomes $\tau_\infty = \ln(1/\epsilon)/(1-c) + 2\ln(1-c)/(1-c) - \gamma/(1-c) - K_0(c)$,

where

$$K_0(c) = \int_0^\infty \left\{ \frac{1}{(1-c)\theta e^\theta} - \frac{1}{e^\theta \left[\theta - c\left(1-e^{-\theta}\right)\right]} \right\} d\theta = \frac{c}{1-c} \int_0^\infty \left\{ \frac{\theta - 1 + e^{-\theta}}{\theta \left[\theta e^\theta - c\left(e^\theta - 1\right)\right]} \right\} d\theta. \tag{4.22}$$

The curve for $b = 0$ in Fig. 4.1 is $K(0, c) = \gamma/(1-c) + K_0(c)$. In the context of the previous analysis [39], in which there was no recombination heat release, this limit affords an indication of the delay in the ignition time associated with radical depletion.

In the limit $b \to \infty$, branching heat release becomes negligible, and $\tau_\infty = \ln(1/\epsilon)/(1-c) + 2\ln(1-c)/(1-c) - \gamma/(1-c) - K_\infty(c)$, where

$$K_\infty(c) = \int_0^\infty \left\{ \frac{1}{(1-c)\theta e^\theta} - \frac{1}{e^\theta - c\theta - 1} \right\} d\theta = \int_0^\infty \left\{ \frac{1 - \theta - e^{-\theta} + c\theta(1-e^{-\theta})}{(1-c)\theta(e^\theta - 1 - c\theta)} \right\} d\theta. \tag{4.23}$$

The curve for $b = \infty$ in Fig. 4.1 was obtained as $K(\infty, c) = \gamma/(1-c) + K_\infty(c)$ by evaluating this integral numerically. The first equality in Eq. (4.23) implies that $K_\infty(0) = -\gamma$, so that $K(\infty, 0) = 0$, unlike the result $K(b, 0) = \gamma$ obtained from Eq. (4.19) for all finite values of b. The limit $b \to \infty$ might be thought to be more relevant than the limit $b \to 0$ for hydrogen-oxygen systems because $b > 1$ in such mixtures. The resulting ignition time will tend to be an upper bound for hydrogen-oxygen, however, because of the neglect of the accelerating effect of the branching heat release on the branching rate, a substantial influence that may render the upper bound excessively high.

4.5 Discussion of Results of the Asymptotic Analysis

To leading order, the ignition time is given by the first term in Eq. (4.20). The most dominant factor in this term is $(B_0 - cB_0)^{-1}$, the reciprocal of the difference between the branching rate and the recombination rate, these rates being

expressed as reciprocal times through division by an appropriate initial reactant-mixture concentration. The time scale for thermal runaway is therefore obtained from the net branching rate. The factor $(1-c)$ multiplying B_0 in Eq. (4.20) corrects the earlier [39] result for the effect of radical depletion by recombination, to be called here simply radical depletion. This effect is independent of energetics, effects of which appear inside the logarithm at leading order. It causes the induction time to approach infinity at crossover (c=1) in leading order. Even though ignition occurs through thermal explosion in this model, net branching is essential to build up the radicals needed for the important strongly temperature-sensitive step, the branching step, to proceed.

In the leading-order logarithmic term in Eq. (4.20), the ratio of the initiation rate to the branching rate, A_0/B_0, appears. Increasing A_0/B_0 decreases the ignition time. This logarithmic effect is well known for branched-chain processes [39]. Also well known in the context of Frank-Kamenetskii types of analyses [35] for small $\epsilon = (A_0/B_0)\alpha_b(1+bc)$ is the dependence on the activation temperature T_a and on the heat release (divided by the heat capacity) q_b through $\alpha_b = q_b T_a/T_0^2$. The present analysis serves to determine the trade-off between effects of heat release in branching α_b and in recombination $\alpha_r = b\alpha_b$. The parameter that finally appears, $\alpha_b + \alpha_r c = (q_b + cq_r)T_a/T_0^2$, is a kind of Zel'dovich number, in which the effective heat release is that in branching plus the initial ratio of the recombination rate to the branching rate times that in recombination.

If there is no heat release in recombination, then $b = 0$, ϵ is independent of c, and the previous[9] ϵ is recovered, $\epsilon = (A_0/B_0)\alpha_b$, indicating the reduction in the induction time through increasing heat release in branching (from α_b inside the logarithm) at leading order. In the opposite limit in which there is no heat release in branching, $b = \infty$, the value of ϵ becomes proportional to c, $\epsilon = (A_0/B_0)\alpha_r c$, so that some recombination is necessary for any heat release at all to be present, enabling the thermal explosion to occur at a finite time. In this limit, the ignition time is infinite at leading order when $c = 0$, and increasing the ratio c of the

recombination rate to the branching rate initially decreases the ignition time by increasing the amount of heat release, an effect which continues until reactant depletion begins to dominate the increase in heat release, driving the ignition time to infinity at $c = 1$, as illustrated in Fig. 4.3 for particular sets of parameters. Figure 4.3 also shows that this effect, the existence of a minimum ignition time at

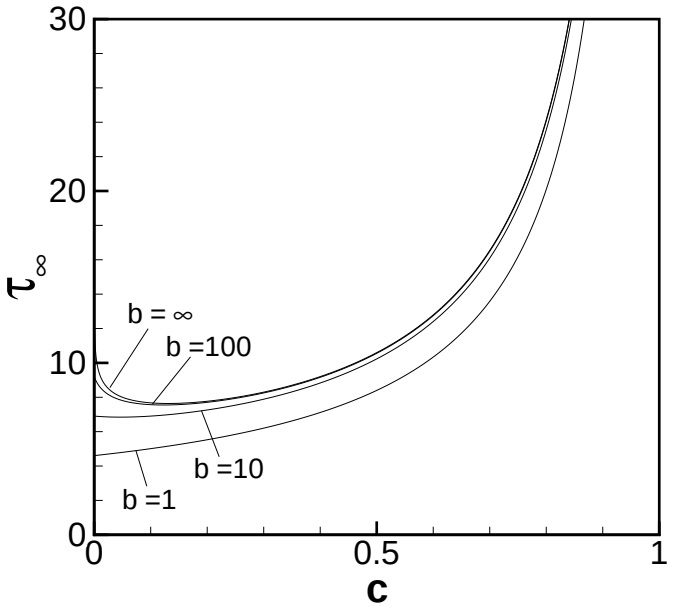

Figure 4.3 The dependence of τ_∞ on c at leading order for $\alpha_r A_0/B_0 = 10^{-2}$ and $b = \infty, 100, 10$ and 1.

an optimal value of c in leading order, persists to finite values of b, at which there is some heat release in branching, so long as $b > \ln(1/\epsilon)$.

The remaining terms in Eq. (4.20) always have the effect of reducing the ignition time below the value obtained at leading order. As c approaches unity the higher-order $\ln(1-c)$ term formally becomes dominant and eventually drives τ_∞ negative, but this is unreal and occurs outside the range of validity of the expansion. It reflects the failure of the expansion as crossover is approached. This is illustrated in Fig. 4.4, which compares values of τ_∞ calculated from Eq. (4.18) with those obtained by numerical integration of Eq. (4.6) for various representa-

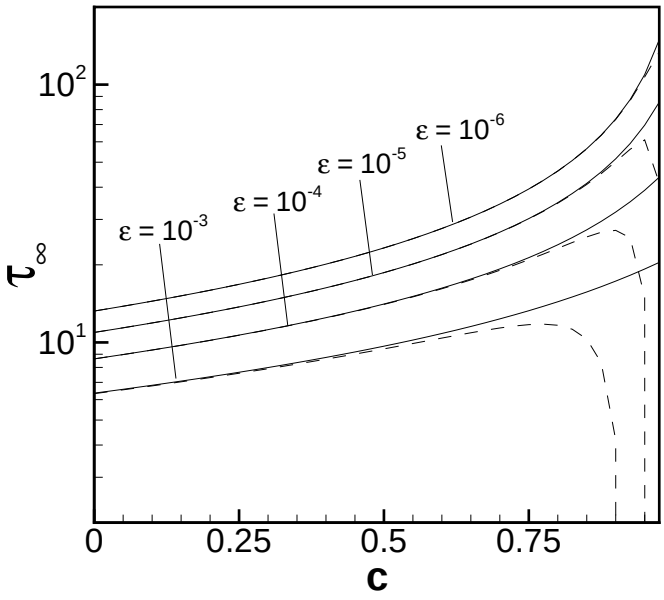

Figure 4.4 Variation of τ_∞ with c, obtained by numerical integration of Eq.(4.6) with $a = 1$, $i = 1$, $b = 1$ (solid curves) and predicted by the asymptotic approximation, Eq. (4.18) with $b = 1$ (dashed curves), for $\epsilon = 10^{-3}, 10^{-4}, 10^{-5}$ and 10^{-6}.

tive cases. In the numerical integration the ignition time was defined by putting $\theta = 10$, which gives a time very near the time at which the solution to Eq. (4.6) approaches infinity. This figure demonstrates the delay in ignition by radical depletion and shows excellent agreement between the numerical and the asymptotic solutions until crossover is approached too closely. The effective small parameter of expansion actually is $\epsilon/(1-c)^2$, and the agreement is excellent when this parameter is sufficiently small. A different expansion is needed near crossover (see Appendix B).

The higher-order term $K(b, c)$ always augments the effect of the $\ln(1-c)$ term in reducing the ignition time. Figure 4.1 shows that the extent of this augmentation decreases as the ratio b increases, suggesting that heat release in branching is more effective than heat release in recombination in promoting ignition, at least

if $\alpha_b + \alpha_r c$ (and hence ϵ) is held fixed as b varies. For $b = \infty$ (all heat release in recombination) and for small b there is a monotonic variation with c in Fig. 4.1 augmenting the effect of the $\ln(1-c)$ term, but for higher finite intermediate values of b this variation is nonmonotonic, contributing an increase in ignition time with increasing c for small c as the recombination heat release comes into play, altering the solution from that obtained [39] with $c = 0$ and heat release only in branching. The jump in $K(b, 0)$ at $b = \infty$ is smoothed by the alternative limit of Eq. (4.21), shown in Fig. 4.2, which expands the region at $c = 0$ near $b = \infty$ of Fig. 4.1 to produce a continuous variation from the result [39] with heat release only in branching to the present result ($b = \infty$) for heat release only in recombination. In this continuous variation at $c = 0$, the higher-order reduction in the nondimensional ignition time from the leading-order value $\tau_\infty = \ln[B_o/(A_0\alpha_b)]$ at $bc = 0$, namely $-\gamma$, decreases to zero as bc increases to infinity, the nondimensional ignition time at leading-order, $\tau_\infty = \ln\{B_0/[A_0\alpha_b(1+bc)]\}$, itself decreasing with increasing total heat release through increasing recombination heat release at constant branching heat release and initiation and branching rates (α_b, A_0 and B_0 (fixed).

4.6 Comparisons of Results for Hydrogen-Oxygen Systems

As indicted in the introduction, one motivation for development of the present theory is its potential application to hydrogen-oxygen systems. For ignition in such systems, under fuel-lean conditions only the H-atom concentration obeys an accurate steady-state approximation, and two radicals, OH and O, are out of steady-state (see Chapter 2 and [55]). This complication precludes an immediate direct comparison for fuel-lean conditions; further analysis would be needed to reduce the concentrations of these two intermediate species to a single effective chain-carrier concentration, and that reduction will not be pursued here. Attention therefore is restricted to fuel-rich and stoichiometric systems, comparisons being

given specifically for hydrogen-air mixtures with equivalence ratios of $\phi = 10$ and $\phi = 1$. The resulting comparisons are, however, representative of those that would be obtained in pure hydrogen-oxygen mixtures or at high dilution, over the full near-stoichiometric and fuel-rich range of equivalence ratios.

From the previous discussion of the model problem it may be seen that A_0 and B_0 are both proportional to the O_2 concentration. It therefore follows from Eq. (4.20) that it is most convenient to make comparisons on the basis of the variation of the product of the ignition time and the oxygen concentration, $t_\infty[O_2]$, with the initial temperature T_0. Such coordinates are quite common in the literature, extensive citations of which are available [55]. Values of T_0 from about 1000 K to about 2500 K are considered here, and results for pressures of $p = 1$ bar and $p = 100$ bar are shown, since they illustrate results that are representative of the general temperature and pressure variations. These selections lead to values of the parameters ϵ between 10^{-7} and 10^{-5} and a between 1.3 and 3.6, with $b = 4.3$ and $i = 3$, so the ordering adopted in the analysis is applicable. If the elementary initiation reaction $H_2+O_2 \rightarrow 2OH$ were included in the short mechanism, negative values of a would be obtained at the lower temperatures, arising from the fact that the rate of the exothermic global reaction $3H_2+O_2 \rightarrow 2H_2O+2H$ in the two-step reduced mechanism would include twice the rate of this elementary initiation reaction $H_2+O_2 \rightarrow 2OH$, thereby effectively contributing exothermicity to initiation in the reduced-chemistry description.

Figure 4.5 compares results of the present theory with those of the previous approximation, shown in Chapter 2 and [55] that equated the ignition time with the time for radicals to reach partial equilibrium isothermally. These two approximations are quite different because partial equilibrium of H plays no role whatever in the present theory, while the temperature change of the present (thermal-runaway) theory is entirely absent for the previous (isothermal) conditions. Yet it is seen in Fig. 4.5 that results of the two different approximations are not very different. Ignition times predicted here are less than those obtained from the pre-

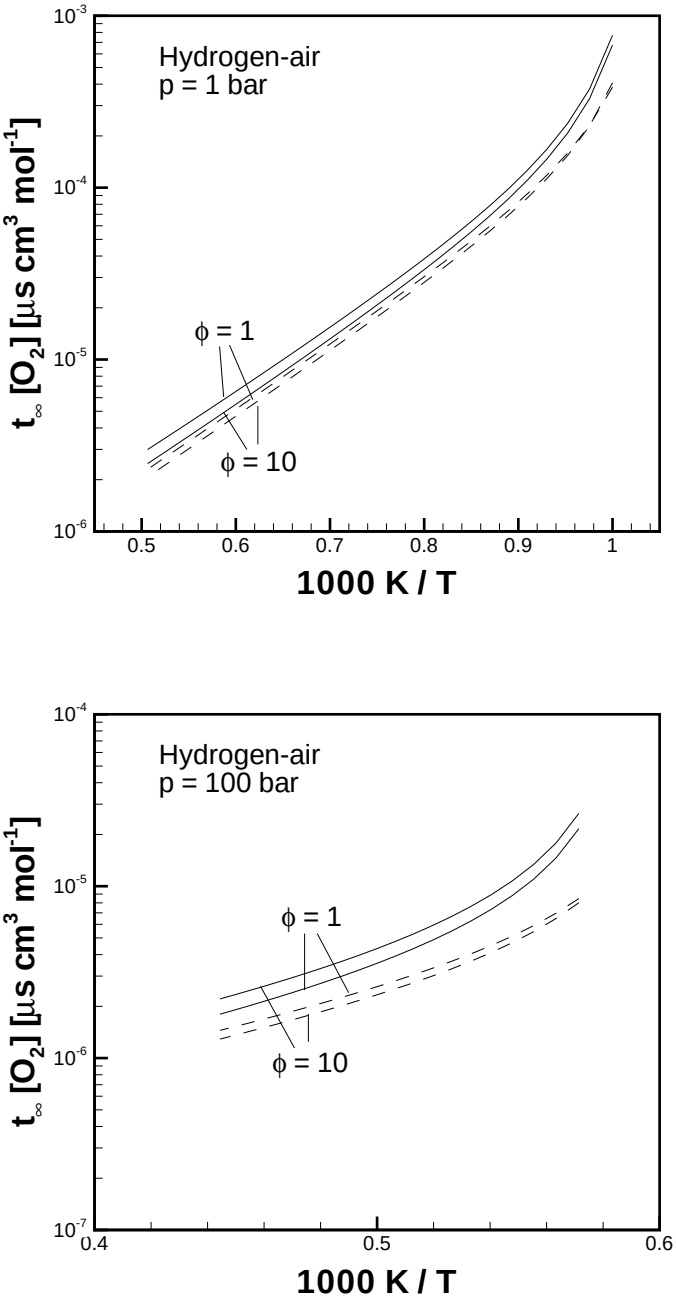

Figure 4.5 Variation of the product $t_\infty[O_2]$ with temperature T_0, predicted by Eq. (4.20) (dashed curves), and obtained in the approximation of isothermal branched-chain explosion considering the ignition time to be the time at which radical concentrations reach partial equilibrium (solid curves), a: for hydrogen-air mixtures with equivalence ratios $\phi = 1, 10$ at a pressure of 1 bar, and b: for hydrogen-air mixtures with equivalence ratios $\phi = 1, 10$ at a pressure of 100 bar.

vious approximation. This indicates that thermal runaway occurs before partial equilibrium is reached, a situation that in fact persists to very low pressures for stoichiometric and fuel-rich mixtures. The heat release that occurs through branching and recombination during radical buildup increases the temperature sufficiently for the associated increased branching rate to produce thermal runaway before the system can achieve partial equilibrium. The difference is larger at higher equivalence ratios and at higher pressures (approaching a factor of two at 100 bar) because the chemistry and heat release are then faster, causing an earlier departure from the isothermal conditions assumed in applying the partial-equilibrium criterion. This result implies that, even with reactant depletion neglected, the partial-equilibrium criterion always overestimates the temperature-inflection ignition time somewhat in stoichiometric and fuel-rich systems. The overestimate increases substantially as the system becomes very fuel-rich (see Chapter 2 and [55]. The present result therefore is a significant improvement over the previous approximation for stoichiometric and rich mixtures when there is interest in ignition times based on temperature inflection.

It is worthwhile to compare the ignition times predicted here with those obtained by full numerical integrations that employ the temperature-inflection criterion. The computations were performed with the FLAMEMaster code [68], all results fully converge with error less than 1%. For the high-temperature conditions addressed here, it was previously shown that autoignition times predicted by full detailed chemistry are indistinguishable from those predicted by a six-step short mechanism that retains only the steps $H_2+O_2 \rightarrow 2OH$, $H_2+O_2 \rightarrow HO_2+H$, $H+O_2 \rightarrow O+OH$, $H_2+O \rightarrow OH+H$, $H_2+OH \rightarrow H_2O+H$ and $H+O_2+M \rightarrow HO_2+M$, all steps treated as irreversible [55]. Since the first of these steps is no longer viable, this becomes a five-step short mechanism that retains agreement with the corresponding detailed mechanism, giving ignition times that differ by less than 10% until crossover is approached. Results of integrations performed with this five-step mechanism and with the detailed mechanism are compared with the present results

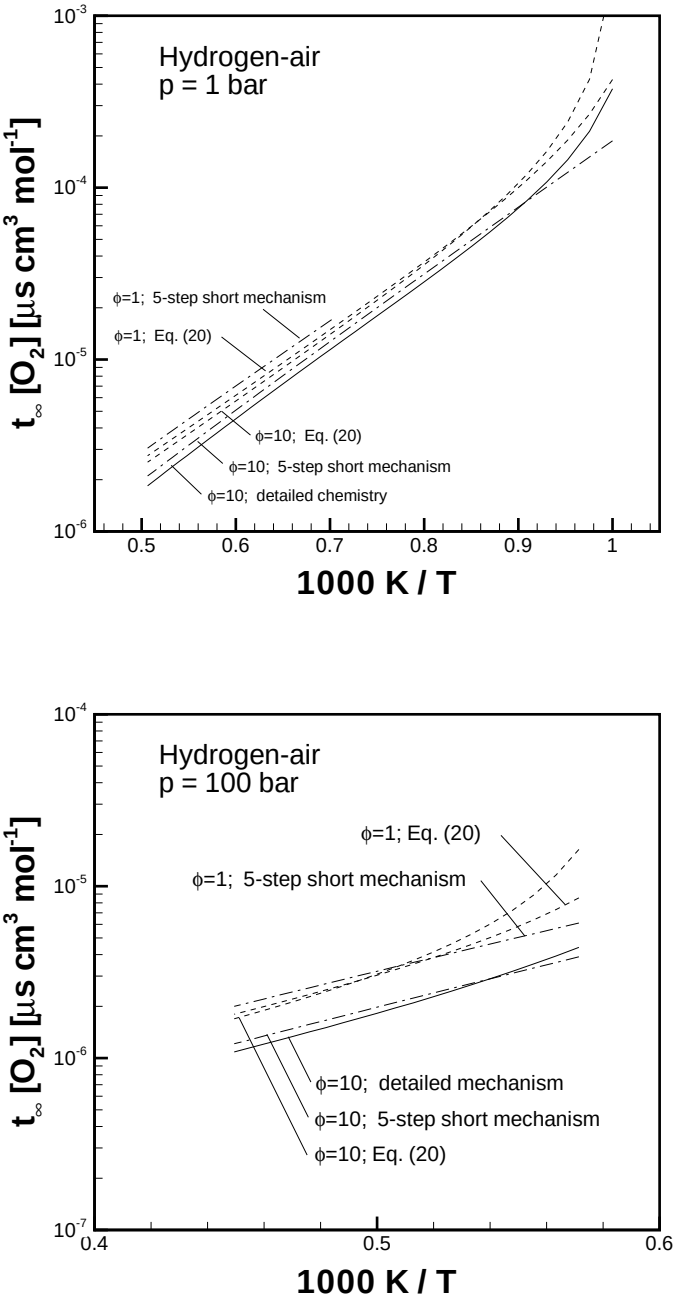

Figure 4.6 Variation of the product $t_\infty[O_2]$ with temperature T_0, predicted by Eq. (4.20) (dashed curves), and obtained in the approximation of isothermal branched-chain explosion considering the ignition time to be the time at which radical concentrations reach partial equilibrium (solid curves), a: for hydrogen-air mixtures with equivalence ratios $\phi = 1, 10$ at a pressure of 1 bar, and b: for hydrogen-air mixtures with equivalence ratios $\phi = 1, 10$ at a pressure of 100 bar.

of Eq. (4.20) in Fig. 4.6, where all conditions are sufficiently far from crossover that Eq. (4.20) is an excellent approximation to the result of numerical integration of Eq. (4.6). The small differences between the predictions of the detailed mechanism and of the five-step mechanism are illustrated in Fig. 4.6 for $\phi = 10$ at 1 bar; these differences are illustrative of those found under other conditions as well. The agreement of the predictions of Eq. (4.20) with the temperature-inflection criterion in the full mechanism is seen in Fig. 4.6 to be excellent in stoichiometric mixtures. This is attributable to the fact that the temperature profiles agree quite well nearly up to the inflection point, and the asymptotic approximation diverges rapidly to infinity after that. For fuel-rich conditions at high pressure, however, the asymptotic ignition times are about twice as long. This is a reflection of differences in predicted temperatures profiles early in the induction history resulting from variations in reaction rates with temperature that are not captured well by the Frank-Kameneskii approximation, partially attributable to effects of falloff at high pressures in the recombination step.

4.7 Conclusions

Over wide ranges of conditions that include fuel-rich hydrogen-oxygen systems, asymptotic analyses based on thermal runaway yield excellent approximations to ignition times defined in terms of inflection points in temperature-time histories. This has been demonstrated explicitly for a chemical-kinetic model that includes temperature-sensitive branching and temperature-insensitive recombination, with exothermicity in either or both of these steps. The explicit formulas for the ignition times, obtained from the asymptotic analysis, show that the ignition time varies inversely with the net branching rate, thereby exhibiting the strong effect of radical depletion through recombination in delaying ignition. The initiation rate and the heat release accelerate ignition through a logarithmic factor. As crossover is approached, where the recombination rate equals the branching rate,

the asymptotic analysis for small initiation rates fails, and different kinds of expansions are needed, which could profitably be investigated in the future. Ignition times become long as crossover is approached, pointing towards the need for a revised nondimensionalization of the time. There are accident scenarios that involve low temperatures and long autoignition times, which motivate future studies in this direction.

At higher temperatures, for stoichiometric and fuel-rich hydrogen-oxygen systems, it has been shown that thermal runaway occurs before the shuffle reactions achieve partial equilibrium, even when reactant depletion is neglected. The partial-equilibrium criterion therefore tends to overestimate ignition times for fuel-rich hydrogen-oxygen systems, although this need not necessarily be true for all fuels because the two criteria depend on entirely different chemical-kinetic parameters that will have different values for different systems. Since applications in aerospace propulsion, of the kind encountered in hydrogen-fueled supersonic-combustion ramjets, for example, often encounter quite fuel-lean conditions, it could be of interest to extent the high-temperature analysis, to account for two radicals (O and OH) not being in steady-state, with the H atom in steady-state, to obtained well-justified closed-form expressions for autoignition times under those conditions.

Chapter 5

Vaporization Of A Droplet In Slowly Varying Rectilinear Flow At Low Reynolds Numbers

The vaporization of a droplet in rectilinear motion relative to a stagnant gaseous atmosphere is addressed for the limit of low Reynolds numbers and slow variation of the droplet velocity. Approximations are introduced that enable a formal asymptotic analysis to be performed with a minimum of complexity. It is shown that, under the conditions addressed, there is an inner region in the vicinity of the droplet within which the flow is nearly quasisteady except during short periods of time when the acceleration changes abruptly, and there is a fully time-dependent outer region in which departures of velocities and temperatures from those of the ambient medium are small. Matched asymptotic expansions, followed by a Greens-function analysis of the outer region enable expressions to be obtained for the velocity and temperature fields and for the droplet drag and vaporization rate. The results are applied to problems in which the droplet experiences constant acceleration, constant deceleration and oscillatory motion. The results, which identify dependences on the Prandtl number and the transfer number, are intended to be compared with experimental measurements on droplet behaviors in time-

varying flows.

5.1 Statement Of The Problem

A theoretical analysis employing matched asymptotic expansions is presented. For a droplet of diameter d, in a flow with a characteristic external velocity u_e measured with respect to the droplet, a characteristic Reynolds number based on droplet radius is

$$\epsilon = \frac{du_e}{2\nu}, \tag{5.1}$$

where ν denotes the kinematic viscosity. Since attention is focused on small Reynolds numbers, ϵ will be a small parameter of expansion. For small ϵ there are two distinguished regions in the flow, an inner Stokes region where the radius is of order d and an outer Oseen region where the radius is of order d/ϵ. A characteristic diffusion time in the Oseen region is therefore $t_o = d^2/4\nu\epsilon^2$, and the ratio of this to a characteristic time t_e of variation of the external velocity is

$$c = t_o/t_e = \frac{d^2}{4\nu\epsilon^2 t_e}. \tag{5.2}$$

The analysis to be developed treats c of order unity and ϵ as a small parameter.

The ratio of a characteristic diffusive time in the Stokes region, $t_s = d^2/4\nu$, to the characteristic time t_e is $c\epsilon^2$ according to Eq. (5.2), which is very small for small ϵ and c of order unity. This favors applicability of quasisteady solutions in the Stokes region to leading order. Although the formulation will allow for general time variations of the external velocity under these restrictions, specific problems resulting in somewhat special expansions will be addressed. One is the acceleration of the droplet from rest in a stagnant atmosphere at a constant acceleration a. In this case, there is no imposed characteristic velocity u_e, and since the Oseen region is expected to control the characteristic evolution time for c of order unity, the value of c in Eq. (5.2) may be set equal to unity, resulting,

with the definition $t_e = u_e/a$ and with Eq. (5.1), in the expression

$$\epsilon = \frac{da^{1/3}}{2\nu^{2/3}} \tag{5.3}$$

for the small parameter of expansion; this corresponds to $u_e = (a\nu)^{1/3}$, making the convection and diffusion terms in the Oseen region be of the same order of magnitude. Another problem concerns the deceleration of a droplet initially vaporizing quasisteadily in a flow of constant external velocity u_e, with a constant deceleration rate a imposed after time zero. In this case, Eq. (5.1) defines the relevant Reynolds number ϵ, and Eq. (5.2) again applies for c with $t_e = u_e/a$. In a general situation, the maximum imposed external velocity would be used to define the small parameter ϵ, and the maximum absolute value of the acceleration would be used to define the parameter c.

The last problem to be addressed in this work corresponds to the evaporation of a droplet in sinusoidal oscillatory motion about a mean velocity u_e, with constant frequency ϖ and amplitude of the oscillations u'_e. In this case Eqs. (5.1) and (5.2) are used to define ϵ and c, with $t_e = \varpi^{-1}$ being the appropriate characteristic time of variation of the external velocity. For purely oscillatory motion with zero mean velocity, the amplitude of the oscillation is taken to be the characteristic external velocity, and therefore $\epsilon = du'_e/(2\nu)$ becomes the corresponding Reynolds number.

5.2 Formulation

The problem is formulated initially with nondimensional variables appropriate for the Stokes region. The droplet radius $d/2$ and the diffusion time in the Stokes region $d^2/4\nu$ are chosen as scales for length and time, and the viscous velocity $2\nu/d$ is selected as the scale for velocity. For simplicity, the density, specific heat, thermal conductivity and coefficient of viscosity initially are assumed constant, and the conservation equations are written in a coordinate system attached

to the droplet. This is an inertial system when the droplet is stationary and the fluid is moving or if the droplet is moving at constant velocity in an ambient fluid at rest, but it is a noninertial system if the droplet moves at variable velocity. Because of the constant-density approximation, both situations can be described by the same formulation if an additional acceleration term is included in the body force, making an additional contribution to the hydrostatic pressure gradient when the droplet is in variable motion. With p' denoting the resulting nondimensional ratio of pressure to density (nondimensionalized by the square of the viscous velocity), $\bar{\bar{\tau}}'$ denoting the corresponding nondimensional viscous stress tensor and $\vec{g}'$ the nondimensional acceleration by body forces, the mass, momentum and energy conservation equations become

$$\nabla \cdot (\vec{v}) = 0, \tag{5.4}$$

$$\frac{\partial \vec{v}}{\partial t} + \vec{v} \cdot \nabla \vec{v} = -\nabla p' + \vec{g}' + \nabla \cdot \bar{\bar{\tau}}' \tag{5.5}$$

and

$$\frac{\partial \theta}{\partial t} + \vec{v} \cdot \nabla \theta = \frac{\nabla^2 \theta}{\sigma}. \tag{5.6}$$

Here σ is the Prandtl number, $\vec{v}$ denotes the nondimensional velocity vector, and the nondimensional temperature is

$$\theta = (T - T_s)/(T_\infty - T_s), \tag{5.7}$$

where T denotes temperature, the subsript s identifies conditions at the surface of the droplet, and the subscript ∞ denotes conditions in the ambient gas.

In the far field, the boundary conditions at infinity are

$$\theta = 1, \qquad \vec{v} = \epsilon U \vec{e}_x, \tag{5.8}$$

where U represents the ratio of the instantaneous external velocity (with respect to the droplet) to u_e, so that ϵU is the instantaneous Reynolds number, and the x direction has been taken to be the direction of the external velocity (assumed not to change with time), $\vec{e}_x$ denoting a unit vector in the x direction. The nondimensional radial coordinate will be denoting by r, and at the droplet surface ($r = 1$), the tangential component of velocity must vanish by the no-slip condition, the liquid being assumed sufficiently viscous to prevent internal fluid motion. The heat of vaporization per unit mass for the liquid L_v is assumed to be large compared with product of the gas constant per unit mass for the liquid and the boiling temperature, whence T_s approximately becomes constant and equal to the boiling temperature, and the other boundary conditions at the droplet surface become

$$\theta = 0, \qquad \frac{\partial \theta}{\partial r} = \frac{\sigma}{B} v_r, \qquad v_r = b, \tag{5.9}$$

where the transfer number is $B = c_p(T_\infty - T_s)/L_v$, c_p denoting the specific heat at constant pressure, v_r is the radial component of the nondimensional velocity, and the nondimensional radial velocity b in the gas at the droplet surface depends in general on both time and the polar angle $cos^{-1}\mu$ measured from the direction of the external gas velocity (the x axis). By symmetry, the velocity and temperature fields are axisymmetric, independent of the azimuthal coordinate in a spherical polar coordinate system.

It is convenient to introduce a nondimensional stream function ψ, replacing the momentum conservation equation by a vorticity conservation equation, and to write the resulting conservation equations in terms of the nondimensional time t, the nondimensional radial coordinate r and the independent variable μ, the cosine of the polar angle. Equations (5.4), (5.5) and (5.6) then reduce to

$$D^4\psi + L(\psi, D^2\psi) = \frac{\partial}{\partial t} D^2\psi \tag{5.10}$$

and

$$\nabla^2\theta + C(\psi,\theta) = \sigma\frac{\partial\theta}{\partial t}, \tag{5.11}$$

where

$$D^2 = \frac{\partial^2}{\partial r^2} + \frac{1-\mu^2}{r^2}\frac{\partial^2}{\partial\mu^2}, \tag{5.12}$$

$$\nabla^2 = \frac{1}{r^2}\frac{\partial}{\partial r}\left(r^2\frac{\partial}{\partial r}\right) + \frac{1}{r^2}\frac{\partial}{\partial\mu}\left((1-\mu^2)\frac{\partial}{\partial\mu}\right), \tag{5.13}$$

$$L(\psi, D^2\psi) = \frac{1}{r^2}\left[\frac{\partial\psi}{\partial\mu}\frac{\partial}{\partial r}D^2\psi - \frac{\partial\psi}{\partial r}\frac{\partial}{\partial\mu}D^2\psi - 2\frac{\partial\psi}{\partial r}\frac{\mu}{1-\mu^2}D^2\psi - \frac{2}{r}\frac{\partial\psi}{\partial\mu}D^2\psi\right] \tag{5.14}$$

and

$$C(\psi,\theta) = \frac{\sigma}{r^2}\left(\frac{\partial\psi}{\partial\mu}\frac{\partial\theta}{\partial r} - \frac{\partial\psi}{\partial r}\frac{\partial\theta}{\partial\mu}\right). \tag{5.15}$$

Equations (5.10) and (5.11) are to be solved subject to the boundary conditions

$$\frac{\partial\psi}{\partial r} = 0, \qquad \frac{\partial\psi}{\partial\mu} = -b, \qquad \theta = 0, \qquad \frac{\partial\theta}{\partial r} = \frac{\sigma b}{B} \tag{5.16}$$

at $r = 1$ and

$$\psi = \frac{1}{2}\epsilon U r^2(1-\mu^2), \qquad \theta = 1 \tag{5.17}$$

at $r = \infty$, and initial conditions $\psi_i(r,\mu)$ and $\theta(r,\mu)$. It is assumed that prior to the time variation of the external velocity, the droplet is evaporating steadily and possibly moving steadily. Uniformly valid matched asymptotic expansions of the solutions ψ and θ based on the small parameter ϵ will be sought. The nondimensional vaporization velocity b at the droplet surface is to be determined in the course of the solution, the nondimensional total vaporization rate, $M = 2\pi\int_{-1}^{1} b\,d\mu$, being of particular interest.

5.3 The Inner Problem And The Quasisteady Inner Solution

In the Stokes region, the solutions for ψ, θ and b can be written for small ϵ in terms of the expansions

$$\psi = \psi_0 + \epsilon\psi', \qquad \theta = \theta_0 + \epsilon\theta',$$
$$b = b_0 + \epsilon b', \tag{5.18}$$

where the leading-order terms

$$\psi_0 = -\mu b_0, \qquad \theta_0 = \frac{1}{B}\left\{(1+B)^{1-1/r} - 1\right\}, \qquad b_0 = \frac{\ln(1+B)}{\sigma} \tag{5.19}$$

correspond to steady vaporization of a droplet at rest in a stagnant atmosphere. The perturbations ψ' and θ' are then found from Eqs. (5.10) and (5.11) to obey

$$D^4\psi' + \epsilon L(\psi', D^2\psi') - \frac{b_0}{r^2}\left(\frac{\partial}{\partial r} - \frac{2}{r}\right) D^2\psi' = \frac{\partial}{\partial t} D^2\psi', \tag{5.20}$$

and

$$\nabla^2\theta' + \epsilon C(\psi', \theta') - \frac{\sigma b_0}{r^2}\frac{\partial\theta'}{\partial r} + \frac{\sigma b_0 (1+B)^{1-1/r}}{B r^4}\frac{\partial\psi'}{\partial\mu} = \sigma\frac{\partial\theta'}{\partial t}, \tag{5.21}$$

with boundary conditions

$$\frac{\partial\psi'}{\partial r} = 0, \qquad \frac{\partial\psi'}{\partial\mu} = -b', \qquad \theta' = 0, \qquad \frac{\partial\theta'}{\partial r} = \frac{\sigma b'}{B} \tag{5.22}$$

at $r = 1$, obtained from Eq. (5.16), and matching conditions with the outer solution at $r \to \infty$.

By introducing Gegenbauer polynomials for the angular dependence of ψ' and Legendre polynomials for the angular dependences of θ' and b', the solution to Eqs. (5.20)-(5.22) can be written as

$$\psi' = U\left\{-\mu\lambda + \frac{1}{2}(1-\mu^2)f\right\}, \qquad \theta' = \sigma U\left\{g - \mu h\right\}, \qquad b' = U\left\{\lambda - \mu\chi\right\}, \tag{5.23}$$

where the functions $f(r,t)$, $g(r,t)$ and $h(r,t)$ as well as $\lambda(t)$ and $\chi(t)$ remain to be obtained. For large t, a quasisteady solution to Eqs. (5.10)-(5.11) applies in the first approximation for small ϵ. The resulting quasisteady problem has been treated extensively in the literature [81,95,101], and it can be shown that, neglecting terms of higher order in ϵ,

$$\lambda = g_\infty B/(1+B) \tag{5.24}$$

and

$$\chi = \frac{1 - K_1 - (1 - 3A_2/A_1)K_3 - 3K_4/A_1}{K_2 + (1 - A_2/A_1)K_3 + K_4/A_1}, \tag{5.25}$$

where

$$A_1 = b_0^2/2 - 1 + (1+b_0)e^{-b_0} \tag{5.26}$$

and

$$A_2 = b_0^2/6 - 1/5 - [(b_0^4 - b_0^3 + 2b_0^2 - 6b_0 - 6)/30]e^{-b_0}, \tag{5.27}$$

which are plotted in Fig. 5.1, and K_1, K_2, K_3 and K_4 are given in Appendix D, while

$$f = r^2 + \frac{2}{r} - \frac{3+\chi}{r}\left\{1 + \frac{b_0^5}{A_1}\left[\int_{1/b_0}^{r/b_0}\left(\xi^3 + \xi^4\right)e^{-1/\xi}d\xi + \frac{r^3-1}{6b_0^3} - \frac{r^5-1}{5b_0^5}\right]\right\}, \tag{5.28}$$

$$g = g_\infty\left(1 - 1/r\right)\left(1+B\right)^{-1/r} \tag{5.29}$$

and

$$h = \left[Ce^{-\sigma b_0} + V_2(r)\right]\left(1 - \frac{2r}{\sigma b_0}\right) - \left[C\left(\frac{2-\sigma b_0}{2+\sigma b_0}\right) + V_1(r)\right]\left(1 + \frac{2r}{\sigma b_0}\right)e^{-\sigma b_0/r}, \tag{5.30}$$

where the functions $V_1(r)$ and $V_2(r)$ are defined as

$$V_1 = \frac{1+B}{B}\int_1^r \left(1 - \frac{2r}{\sigma b_0}\right)\frac{f(r)}{r^2}dr \tag{5.31}$$

and

$$V_2 = \frac{1+B}{B}\int_1^r \left(1 + \frac{2r}{\sigma b_0}\right)\frac{f(r)}{r^2}e^{-\sigma b_0/r}dr, \tag{5.32}$$

and

$$C = \frac{(1+B)(2+\sigma b_0)}{B(\sigma b_0)^2 K_2}\left\{1 - K_1 + 2K_3 - (3+\chi)\left[K_3(1 - A_2/A_1) + K_4/A_1\right]\right\}. \tag{5.33}$$

Expansions of χ, f, g and h for small and large values of b_0 are given in Appendix E.

These results are stated here, without derivation, in an optimally compact form which cannot be found in the literature. It may be noted from these result that, even for the time-dependent problem, the functions f and h are independent of t, and χ is a constant. These functions and the constant χ are determined uniquely by just two parameters, the thermodynamic variable B and the transport property σ, the nondimensional leading-order vaporization rate b_0 being related to these by Eq. (5.19). The angular dependences of the temperature field and vaporization rate are carried by the time-independent function h and eigenvalue χ, and these dependences average to zero when integrated over all angles. The time dependences of the vaporization rate and the temperature field appear only in U, λ and g and, given U, are determined by the single function $g_\infty(t)$, which must be obtained by matching. Except for the given function $U(t)$ and the simple

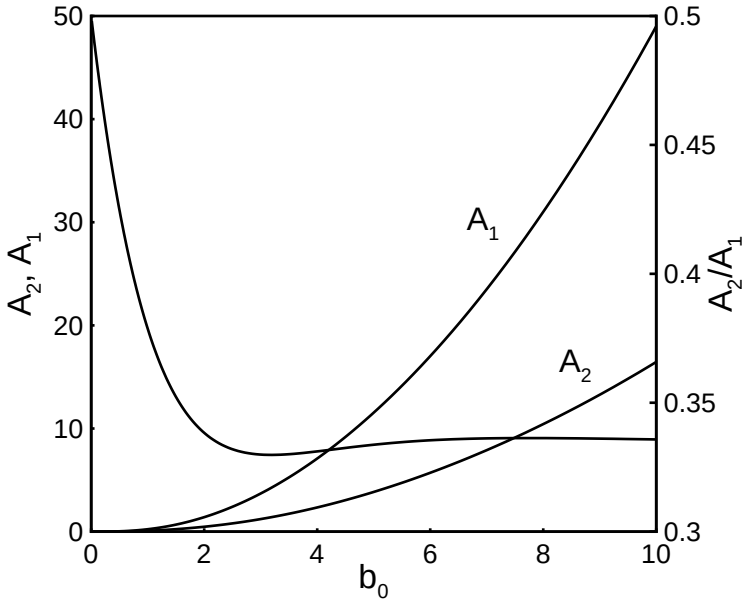

Figure 5.1 Variations of the constants A_1 and A_2 given by Eqs. (5.26) and (5.27) and of the ratio A_2/A_1 with the unperturbed nondimensional vaporization rate b_0.

dependence arising through $\lambda(t)$, the velocity field depends only on the function f, which is seen from Eq. (5.28) to be independent of t, like h and χ, and determined uniquely by b_0 and σ. The normalized nondimensional vorticity in the inner region can be expressed as $\omega = -\epsilon\sqrt{1-\mu^2}\Omega/r$, with $\Omega = d^2f/dr^2 - 2f/r^2$. Introducing the expression for f given by Eq. (5.28) into this formula for Ω gives

$$\Omega = \frac{2(3+\chi)r^2}{A_1}\left\{e^{-b_0/r}\left(1+\frac{b_0}{r}+\frac{b_0^2}{2r^2}\right)-1\right\}, \tag{5.34}$$

the functional form of which depends only on b_0, the Prandtl number σ appearing only in the prefactor. The only unknown to be determined by matching to the outer region then, up to terms of order ϵ^2, is g_∞, which affects the temperature field and the vaporization rate.

5.4 Properties Of The Quasisteady Inner Solution

5.4.1 Velocity field and mass source

From Eqs. (5.18), (5.23) and (5.24) the nondimensional vaporization velocity can be written, up to terms of order ϵ^2, as

$$b = b_0 + \epsilon U \left\{ g_\infty B/(1+B) + \mu\chi \right\}, \tag{5.35}$$

in which U and g_∞ determine the time dependence and χ the angular dependence. Values of χ obtained from Eq. (5.25) are plotted in Fig. 5.2 as a function of b_0 for three values of σ. It can be seen that there is a monotonic increase of χ with b_0,

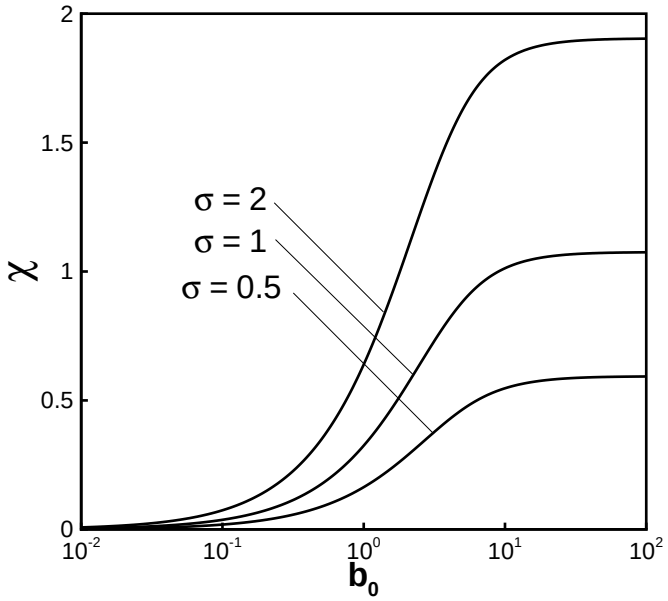

Figure 5.2 Variations of χ, the nondimensional coefficient of the angular dependence of the vaporization rate, with the unperturbed nondimensional vaporization rate b_0 evaluated from Eq. (5.25) for different values of the Prandtl number ($\sigma = 0.5, 1$ and 2).

which goes from zero at $b_0 = 0$ to

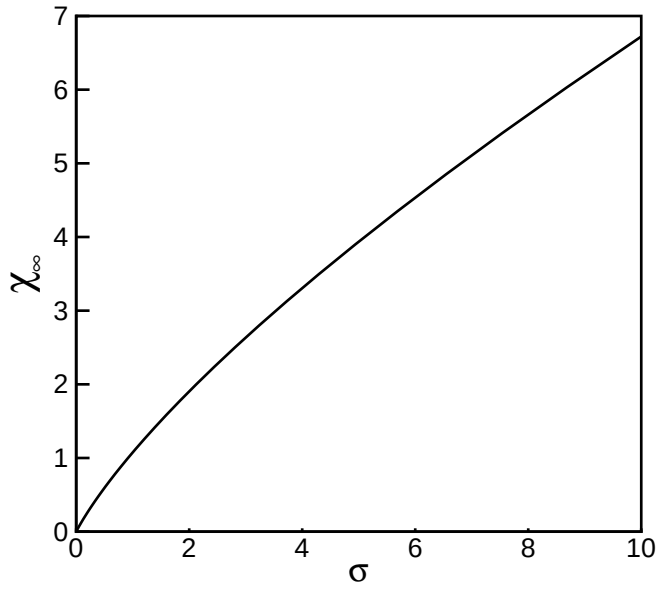

Figure 5.3 Dependence of χ_∞ on σ obtained from Eq. (5.36), showing how, in the limit of large vaporization rates, the strength of the angular dependence of the vaporization rate increases with the Prandtl number.

$$\chi_\infty = 15\sigma^3 \left\{ \sigma^5 \ln\left(\frac{1+\sigma}{\sigma}\right) + \left(10\sigma^2 + 15\sigma + 6\right) \ln(1+\sigma) - \right.$$
$$\left. \sigma^4 + \sigma^3/2 - 12\sigma^2 - 6\sigma \right\}^{-1} - 3, \tag{5.36}$$

at $b_0 = \infty$. The dependence of χ_∞ on the Prandtl number σ is shown in Fig. 5.3, which exhibits an increase of χ_∞ with σ from $3\sigma/2$ at small σ to $3\sigma/(2\ln\sigma)$ at large σ. Thus, in addition to increasing in proportion to the external relative velocity (through U) and to the apparent external temperature increase (through g_∞), the vaporization rate becomes larger in the upstream direction and smaller in the downstream direction, by an amount which increases with increasing unperturbed vaporization velocity and with increasing Prandtl number, lower thermal conductivities enhancing the angular dependence.

The nondimensional total vaporization rate $M = 2\pi \int_{-1}^{1} b d\mu$ can be calculated from the solution for b in Eq. (5.35) to give

$$M = 4\pi \left\{ [\ln(1+B)]/\sigma + \epsilon U g_\infty B/(1+B) \right\}. \tag{5.37}$$

From Eq. (5.4) it can be shown that M is the total rate of mass transfer through any spherical surface in the inner zone surronding the droplet (and centered at the droplet center) divided by the product of the viscosity coefficient and the droplet radius. Applying this result to large values of r demonstrates that sufficiently far from its surface the droplet behaves like a point source of mass, the stregth of which increases with increasing B, U, g_∞ and thermal conductivity (through σ).

The velocity field, determined by the stream function, is purely radial and irrotational at leading order in the inner zone, and there is an additional irrotational radial contribution, through λ in Eq. (5.23), in the perturbation. In addition to that, the perturbation introduces a nonradial, angular-dependent rotational contribution through f. The dependence of this component of the nondimensional stream function on r for various values of b_0 is shown in Fig. 5.4, for three different values of σ. The corresponding radial and tangential components of the nondimensional velocity, normalized by the product ϵU, are $\mu f/r^2$ and $-\sqrt{1-\mu^2}(df/dr)/(2r)$, respectively, and they are plotted for the limit of large b_0 in the fourth panel of the figure. The rotational part of the velocity field generates an angular-dependent component in the distribution of the nondimensional pressure p' of Eq. (5.5), which, normalized by the product ϵU, can be written as μp with

$$p = f'''/(2r) - [b_0 + 1/(2r^2)]f'' + f'[1/(2r^3) - 1/r^2] + 2f/r^3, \tag{5.38}$$

the prime here denoting differentiation with respect to r.

Figure 5.4 shows that at the droplet surface the function f is negative with zero slope, except in the limit $b_0 = 0$, in which case the value is zero. In this

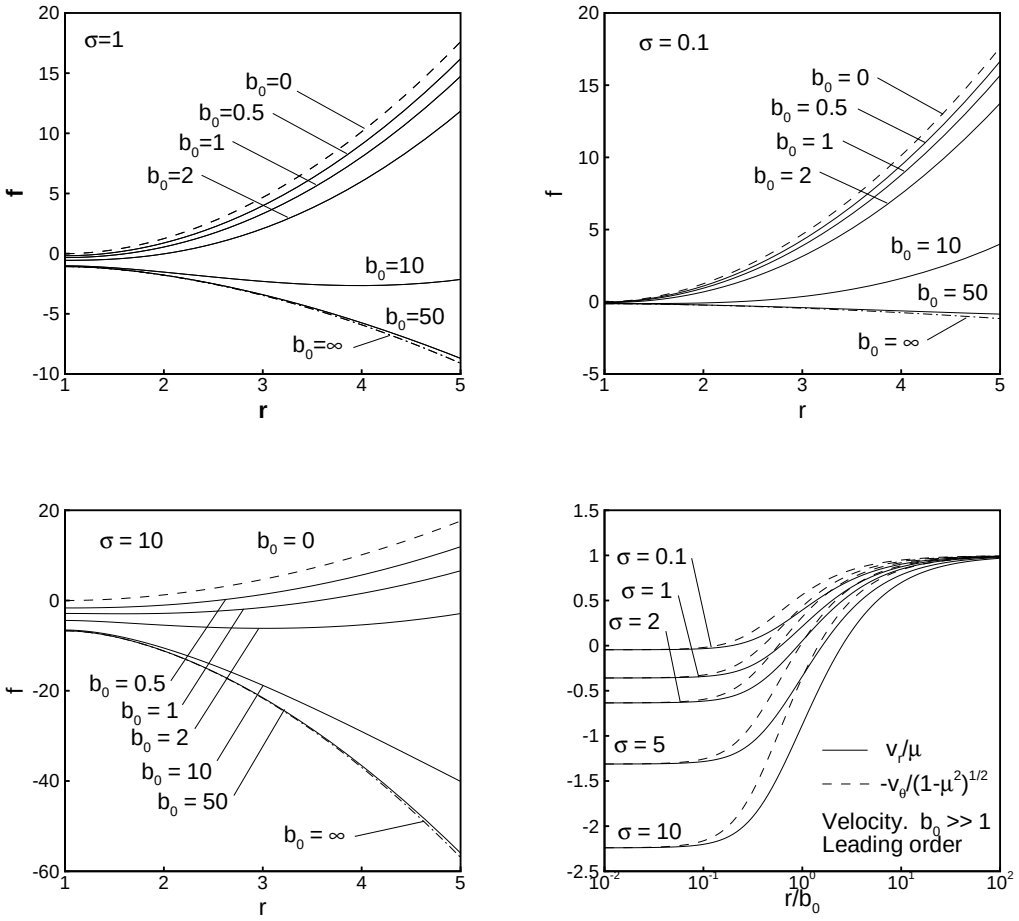

Figure 5.4 The rotational component of the velocity field in the inner region. The first three pannels show variations with r of the component f of the nondimensional perturbation stream function ψ' of Eq. (5.23), as given by Eq. (5.28), for various values of b_0 (solid lines: $b_0 = 0.5, 1, 2, 10$ and 50; dashed lines: $b_0 = 0$; dashed-dotted lines: $b_0 = \infty$) and for different values of Prandtl number (first panel: $\sigma = 1$; second panel: $\sigma = 0.1$; third panel: $\sigma = 10$). The fourth panel represents the radial and tangential components of the nondimensional velocity, normalized by the product ϵU, in the strong-vaporization limit.

limit, from the expansion given in Appendix B it is seen that $f = r^2 - 3r/2 + 1/(2r)$, which is the nondimensional stream function for a nonvaporizing sphere in steady flow for all values of σ, plotted as dashed curves in the first three panels of Fig. 5.4. The curves in Fig. 5.4 for small b_0 have positive curvature for all r, so f becomes positive near the droplet surface, at a radial distance that increases with increasing vaporization velocity. The curves for large b_0, however, have a negative curvature near the droplet surface, and f becomes positive only far from the surface. From the expansions for large b_0 given in Appendix D it can be seen that near the droplet surface, where r is of order unity, the nondimensional stream function approaches the negative-valued function $f = -(\chi_\infty/3)(r^2 + 2/r)$, for which the velocity field is irrotational; this is shown as the dot-dash curves in the first three panels of Fig. 5.4. Essentially, at large b_0, the vorticity region is blown away from the droplet surface, and a mixing region develops at large r, the flow being reversed on the droplet side, as will now be described more fully.

As shown in Appendix D, to investigate the blown-off mixing region it is appropriate to rescale r with b_0 and f with b_0^2. The fourth panel in Fig. 5.4 shows the resulting normalized nondimensional radial and tangential velocity components from f in this rescaled mixing region. These perturbations become equal, implying a purely axial component of the velocity field, not only outside the mixing region but also on the droplet side of it. Moreover, on the droplet side the tangential velocity component points upstream, except when $\sigma = 0$, in which case it is zero. This reverse flow is generated by the interactions of the angular-dependent source flow with the externally imposed uniform flow. Expanding Eq. (5.38) for large b_0 gives $p/b_0 = f''$ at leading order in b_0^{-1}, indicating that the angular-dependent component of the pressure is given mainly by the momemtum flux in the tangential direction. Since the angular-dependent tangential velocity component points upstream, which it must do to satisfy continuity as a consequence of the relative increase of the vaporization rate on the upstream side of the droplet, the pressure gradient in the tangential direction, $\sqrt{1-\mu^2}p/r$, becomes negative, reversing the

flow in this perturbation contribution. The pressure gradient, and consequently the strength of the reverse flow, increases with σ, smaller thermal conductivities favoring larger perturbations through the interactions. In the fourth panel of Fig. 4 it is seen that, except at the edges of the mixing region, the tangential velocity component always lies above the radial velocity perturbations, that is, the shear is largely in the tangential direction.

To illustrate more clearly the structure of the inner solution in the large-b_0 limit, the perturbation streamlines and isotherms calculated from the large-b_0 inner solution of the fourth panel of Fig. 4, for a droplet evaporating steadily in a constant-velocity flow are plotted in Fig. 5. The expressions for ψ' and θ used to obtained the curves in Fig. 5 are given by Eqs. (18), (19) and (23)-(33) with $g_\infty = \sigma(1+B)/(2B)$, the value obtained from matching to the outer solution for steady flow. It can be seen in Fig. 5 that, for large b_0, the effect of higher Prandtl numbers is to increase the stregth of the reverse flow and decrease the temperature of the inner region, the reverse-flow tendency being especially evident from the separation region downstream from the droplet, seen in Fig. 5b. The separation region, with reverse flow present everywhere around the droplet, is of course present only in the perturbation, as may be seen, for example, from the streamlines for the full solution, obtained from Eqs. (18), (19) and (23), plotted in Fig. 6 for $\epsilon U = 0.1$, with the other parameters corresponding to Fig. 5b.

The different behavior of the velocity field for strong vaporization, as compared with the behavior for weak or moderate vaporization, may also be viewed in terms of the vorticity in the inner region. Figure 5.7 shows (for $\sigma = 1$) the r dependence of the vorticity factor Ω given by Eq. (5.34), for the same values of b_0 that were selected for the first panel of Fig. 5.4. For $b_0 = 0, 0.5$ and 1, at the droplet surface the vorticity has a maximum value which decreases as the vaporization velocity increases. With further increase of b_0, the maximum of vorticity becomes detached from the surface. The curves for $b_0 = 10$ and 50 in Fig. 5.7 have approximately the same shape and maximum value, which is located at a

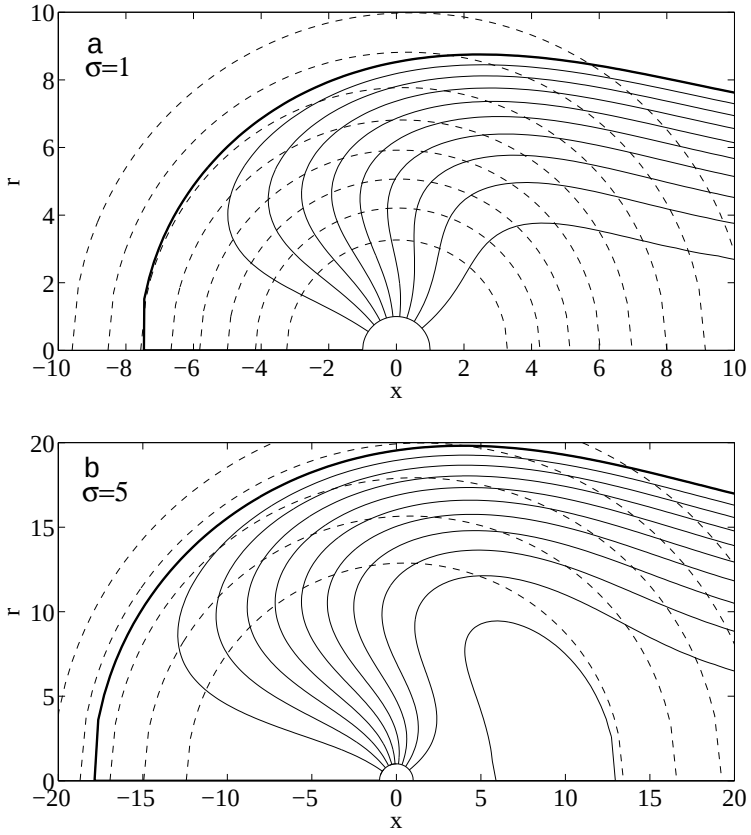

Figure 5.5 The streamlines for the perturbation of the streamfunction ($\psi'/(\epsilon U)$= $-\lambda$, corresponding to the horizontal axis $\mu = 1$, $-4\lambda/5$, $-3\lambda/5$, $-2\lambda/5$, $-\lambda/5$, 0, $4\lambda/5$, $3\lambda/5$, $2\lambda/5$, $\lambda/5$, and λ, the separatrix corresponding to the stagnating streamline) and the isotherms (Fig. 5a: θ=0, 0.05, 0.1, 0.15, 0.2, 0.25 and 0.30; Fig. 5b: θ=0, 0.03, 0.06, 0.09, 0.12 and 0.15), calculated from the large-b_0 inner solution for a droplet evaporating steadily in a constant-velocity flow, plotted as solid curves and dashed curves, respectively, for $b_0 = 10$, with $\sigma = 1$ (Fig. 5a) and $\sigma = 5$ (Fig. 5b).

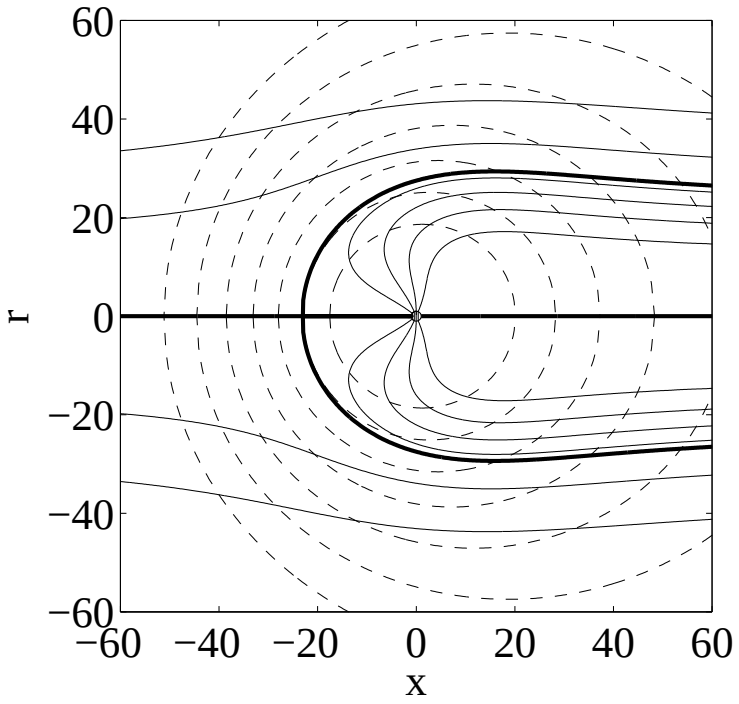

Figure 5.6 The streamlines (ψ=$-b_0 - \epsilon U\lambda$, corresponding to the horizontal line at r=0 for $x > 0$, -5, 0, 5, 10, $b_0 + \epsilon U\lambda$, the separatrix corresponding to the stagnating streamline, 25 and 50), shown as solid curves with the $\mu = 1$ and stagnation streamlines bold, and the isotherms (θ=0, 0.1, 0.2, 0.3, 0.4, 0.5, 0.6 and 0.7), shown as dashed curves, calculated from the large-b_0 inner solution for a droplet evaporating steadily in a constant-velocity flow for $\epsilon U = 0.1$ and $b_0 = 10$, with $\sigma = 5$.

radial distance proportional to b_0. This result indicates that, for sufficiently high vaporization velocities, the structure of the velocity field in the mixing region does not change if the problem is appropriately rescaled, as summarized in Appendix D. It may be remarked that, since this large-b_0 behavior applies only when the mixing layer is in the inner region, the value of ϵ must be small enough that $b_0 \ll 1/\epsilon$, that is, given ϵ the results break down when b_0 becomes too large. Figure 5.6, for which $b_0 = 1/\epsilon$, violates this inequality for the purpose of illustrating most clearly the characteristics of the streamlines.

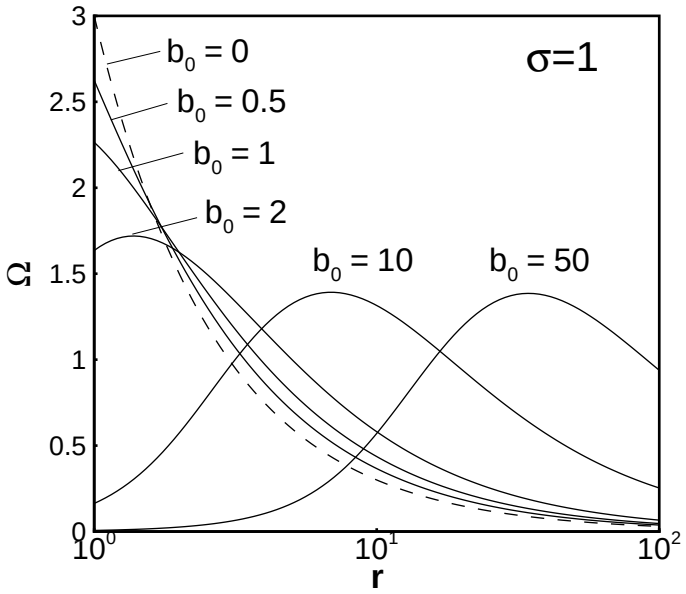

Figure 5.7 The r dependence of the vorticity factor Ω given by Eq. (5.34) for various values of b_0 (solid curves: $b_0 = 0.5, 1, 2, 10$ and 50; dashed curve: $b_0 = 0$) for $\sigma = 1$.

5.4.2 Force balances and Point Force

Once the velocity field in the inner region is obtained, the drag of the droplet can be determined. The nondimensional body force $\vec{g}$ that appears in Eq. (5.5) is of order ϵ^2, so its contribution to the pressure distribution in the inner

region can be neglected in the first approximation. Then, the total nondimensional drag corresponding to the quasisteady inner velocity field can be written as

$$F = 6\pi\epsilon U \left\{ \frac{(3+\chi)b_0^3}{9A_1} - \frac{2b_0}{3} \right\} + O(\epsilon^2). \tag{5.39}$$

Figure 5.8 shows variations of $F/6\pi\epsilon U$, calculated from Eq. (5.39), with b_0 for various values of σ. With this normalization, the well-known Stokes drag of a nonvaporizing sphere in steady rectilinear flow corresponds to $F/(6\pi\epsilon U) = 1$, and it is seen in Fig. 5.8 that, indeed, $F/(6\pi\epsilon U) = 1$ at $b_0 = 0$ for all values of σ. In this limit, the contribution of the viscous stresess to the drag is dominant and is twice the contribution of the pressure forces, which act in the same direction, that is, the total force arises two thirds from the viscous stresses and one third from the pressure.

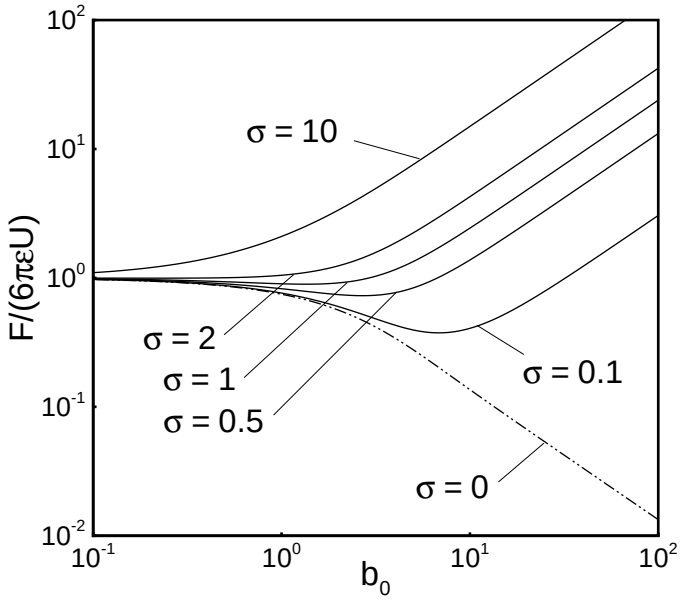

Figure 5.8 Variations with b_0 of normalized drag $F/(6\pi\epsilon U)$, calculated from Eq. (5.39), for various values of σ (solid curves: $\sigma = 0.1, 0.5, 1, 2$ and 10; dashed curve: $\sigma = 0$).

The curves for $\sigma \leq 2$ in Fig. 5.8 have negative slope at $b_0 = 0$ and reach

a minimum value that decreases with decreasing Prandtl number. However, the curve for $\sigma = 10$ has a positive slope at $b_0 = 0$. Calculating the derivative of F with respect to b_0 at $b_0 = 0$ from Eq. (5.39) gives a critical value of $\sigma = 7/3$, above which the drag increases with b_0 monotonically. At lower Prandtl numbers, then, moderate vaporization decreases drag. In the large-b_0 limit the normalized drag on the droplet is $2b_0\chi_\infty/9$ in the first approximation and is mainly due to the momentum flux ($4b_0\chi_\infty/9$), which is twice the contribution of the pressure forces, which provide thrust (negative drag, $-2b_0\chi_\infty/9$). The viscous stresses have a vanishing net contribution to drag in this limit.

From the quasisteady momentum conservation equation in the inner region, given by Eq. (5.5) with body forces and local time derivatives neglected, it can be shown that $F\vec{e}_x$ is the total force transmitted to a spherical surface of radius r divided by the product of the density and the square of the kinematic viscosity. The droplet therefore behaves like a point force for large values of r, although this point-force effect is of order ϵ in comparison with the mass-source effect of Eq. (5.37). The strength of the point force increases with both b_0 and σ for large b_0, becoming proportional to the vaporization velocity, a measure of the source strength. The initial drag reduction by vaporization at small σ is notable, F approaching $1 + (3\sigma - 7)b_0$ as b_0 approaches zero. The minimum drag in fact approaches zero as σ approaches zero, and in the limit $\sigma = 0$ the drag is a monotonically decreasing function of b_0, approaching zero as b_0 approaching infinity. In this limit, the flow near the droplet becomes isothermal and insulated from the external flow. Substantial drag reduction through vaporization therefore can occur at low Prandtl numbers (high thermal conductivities), especially at high vaporization rates.

5.4.3 Temperature Field and Heat Sink

From Eq. (5.23) it may be seen that the average perturbation of the inner temperature field is described by the function g, and its angular dependence

arises from the function h. It can be shown from Eq. (5.30) that as r approaches infinity h approaches $[(1+B)\ln(1+B)]/(2B)$ for all values of σ. Variations of $2Bh/[(1+B)\ln(1+B)]$ with r for various values of B, calculated from Eq. (5.30), are plotted in Fig. 5.9a. The ratio (g/g_∞) is similarly plotted in Fig. 5.9b as a function of r, with g evaluated from Eq. (5.29). The dashed curves in Figs. 5.9a and 5.9b correspond to $h = 1/2 - 3/4r + 3/8r^2 - 1/8r^3$ and $g/g_\infty = 1 - 1/r$, respectively, which describe the perturbation of the inner temperature in the nonvaporization limit $B = 0$, obtained in Appendix D. The gradients of h and g at the surface decrease as B increases. In the strong-vaporization limit, $B \gg 1$, variations of the temperature are exponentially small near the surface and begin to be important only at radial distances from the surface of order $\ln(1+B)$. The asymptotic behavior of θ for large values of r becomes

$$\theta \sim \theta_\infty - \frac{q_\infty}{r}, \tag{5.40}$$

with

$$\theta_\infty = 1 + \epsilon U \sigma \left\{ g_\infty - \mu \frac{(1+B)\ln(1+B)}{2B} \right\} \tag{5.41}$$

measuring the apparent outer temperature and

$$q_\infty = \frac{(1+B)\ln(1+B)}{B} + \epsilon U \sigma \left\{ g_\infty \left[1 + \ln(1+B)\right] + \mu \frac{(1+B)\ln(1+B)}{B} B_1 \right\} \tag{5.42}$$

the inward heat flux. Equations. (5.41) and (5.42) are obtained from Eqs. (5.18), (5.23) and (5.25)-(5.33) by constructing expansions for large values of r. The constant B_1 in Eq. (5.41) can be written as

$$B_1 = \frac{\ln(1+B)}{2} + \frac{(\chi+3)b_0^3}{12A_1}. \tag{5.43}$$

Equations (5.41) and (5.42) exhibit an angular-independent increase of θ_∞ and q_∞ with the transfer number. These increases are proportional to the

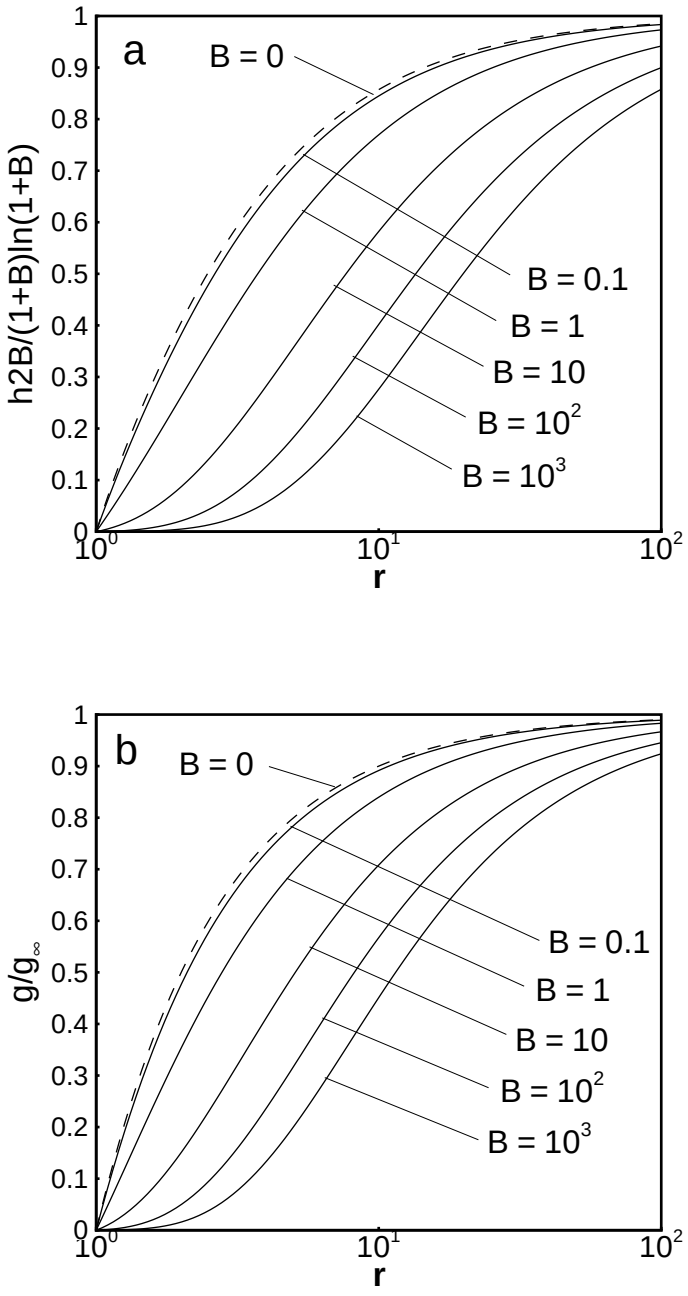

Figure 5.9 Variations with r of a: the normalized angular-dependent contribution to the temperature field $2Bh/[(1+B)\ln(1+B)]$, calculated from Eq. (5.30), and b: the normalized angular-independent perturbation to the temperature field (g/g_∞), calculated from Eq. (5.29), for various values of B (solid curves: $B = 0.1, 1, 10, 10^2$ and 10^3; the dashed curves correspond to $h = 1/2 - 3/4r + 3/8r^2 - 1/8r^3$ and $g/g_\infty = 1 - 1/r$, the solution for the nonvaporization lmit $B = 0$).

relative external velocity, to the Prandtl number and to g_∞. The Prandtl-number factor indicates that the Peclet number $\epsilon\sigma$ rather than the Reynolds number ϵ measures the stregth of these effects. They enhance both the apparent external temperature and the heat flux. Angular-dependent contributions also are present. The apparent temperature is smaller in the downstream direction and larger in the upstream direction, by an amount that increases with increasing B.

The angular variation of q_∞ can be illustrated by plotting B_1 as a function of B, as shown in Fig. 5.10 for various values of σ. This figure exhibits a monotonic

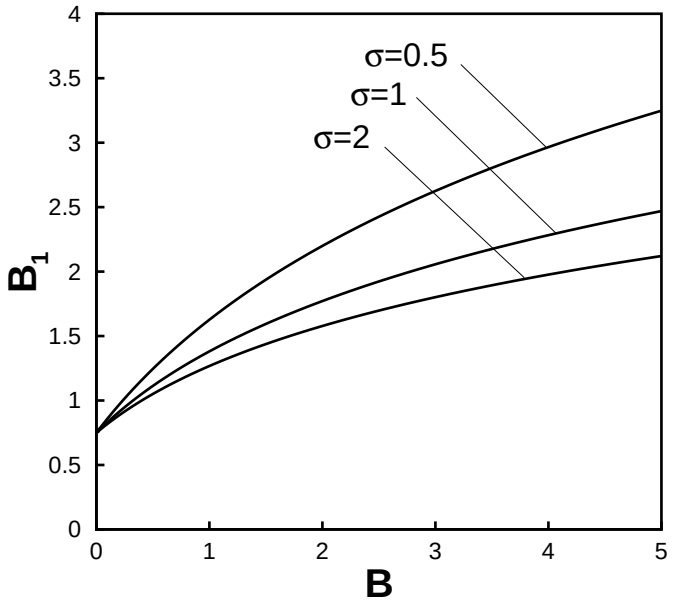

Figure 5.10 Variations of the measure B_1 of the angular dependence of the strength of the heat sink with b_0 evaluated from Eq. (5.43) for different values of the Prandtl number ($\sigma = 0.5, 1$ and 2).

increase of B_1 with B, indicating an increase of the heat flux with increasing transfer number in the upstream direction and a decrease in the downstream direction with increasing transfer number. Although B_1 decreases with increasing σ in Fig. 5.10, the effect of the factor σ in Eq. (5.42) is stronger, so that the angular dependence also increases with increasing Prandtl number at fixed Reynolds number. In

the nonvaporization limit $B_1 = 3/4$, independent of the Prandtl number.

The nondimensional total rate of heat transfer $Q = 2\pi \int_{-1}^{1} q_\infty d\mu$ can be calculated from the solution for q_∞ in Eq. (5.42) to be

$$Q = 4\pi\{(1+B)\ln(1+B)/B + \epsilon U\sigma g_\infty[1+\ln(1+B)]\}. \tag{5.44}$$

From Eq. (5.6) it can be shown that BQ is the total rate of heat transfer through any spherical surface in the inner zone surronding the droplet divided by the product of the heat of vaporization per unit mass, the viscosity coefficient and the radius of the droplet. Applying this result to large values of r demonstrates that sufficiently far from its surface the droplet behaves like a point sink of heat, the stregth of which increases with increasing B, U, σ and g_∞.

5.5 The Outer Solution

In terms of the appropriate rescaled outer variables $R = \epsilon r$, $\vec{V} = \vec{v}/\epsilon$, the temperature and stream function in the outer region, denoted by $\Theta = \theta$ and $\Psi = \epsilon\psi$, can be written in terms of the expansions

$$\Theta = 1 - \epsilon\Theta', \qquad \Psi = \frac{1}{2}UR^2(1-\mu^2) + \epsilon\Psi'. \tag{5.45}$$

It is convenient to introduce the outer time variable $\tau = \epsilon^2 t$, the characteristic diffusion time $t_o = ct_e$, according to Eq. (5.2), being the appropriate time scale in this region. From Eq. (5.6) the nondimensional temperature perturbation Θ' then satisfies the energy conservation equation

$$\frac{\partial\Theta'}{\partial\tau} + U\frac{\partial\Theta'}{\partial X} - \frac{1}{\sigma}\widetilde{\nabla}^2\Theta' = (Q/\sigma)\delta^3(\vec{R}), \tag{5.46}$$

with boundary condition $\Theta' \to 0$ at infinity. Here $\widetilde{\nabla}$ denotes the gradient operator defined in Eq. (5.13) but based on outer variables, $X = \epsilon x$ denotes the axial coordinate in the outer variables, and δ^3 stands for the delta function in three dimensions. The right-hand side of Eq. (5.46) represents a point heat sink located at the center of the droplet with time-dependent stregth Q given by Eq. (5.44).

By changing to a stationary reference system with origin located at the position of the droplet at $\tau = 0$, the solution to Eq. (5.46) can be written in terms of the Greens function of the unsteady diffusion equation [111]. The solution for Θ' based on coordinates moving with the droplet then becomes

$$\Theta' = \frac{\sqrt{\sigma}}{(4\pi)^{3/2}} \int_{-\infty}^{\tau} \frac{Q(\tau_0)}{\hat{\tau}^{3/2}} \exp\left\{\frac{-\sigma \hat{R}^2}{4\hat{\tau}}\right\} d\tau_0, \tag{5.47}$$

where $\hat{\tau} = \tau - \tau_0$ is the difference between the actual time and the integration time, $\hat{R} = \{[\mu R - X_d(\tau) + X_d(\tau_0)]^2 + (1-\mu^2)R^2\}^{1/2}$ is the distance to the center of the droplet in stationary coordinates, and $X_d(\tau) = \int_0^\tau U(\tau')d\tau'$ is the axial position of the droplet relative to its position at $\tau = 0$.

The asymptotic expansion of Θ' for small values of R needs to be obtained in order to determine g_∞ by matching with the inner temperature. In acomplish that, it is not valid to take the limit $R \to 0$ inside the integral of Eq. (5.47) because $\tau_0 = 0$ is within the limits of integration. Instead, it is necessary to expand asymptotically the integral for small values of R and then take the limit. This can be demonstrated formally by considering the quasisteady outer temperature generated by a constant-strength heat source Q_0 in a uniform flow at constant velocity U_0. In this case $\hat{R}^2 = R^2 - 2\mu R U_0 \hat{\tau} + U_0^2 \hat{\tau}^2$, so that the intregal in Eq. (5.47) can be evaluated exactly to give $\Theta' = [\sigma Q_0/(4\pi)]exp[-(1-\mu)\sigma R/2]$, which is the quasisteady outer solution. Taking the limit $R \to 0$ inside the integral of Eq. (5.47), however, gives $[\sqrt{\sigma}Q_0/(4\pi)^{3/2}] \int_0^\infty \hat{\tau}^{-3/2} exp(-\sigma\hat{\tau}U_0^2)d\hat{\tau}$ at leading order in R, the integral in which is divergent at its lower limit.

To express results in the most general form, an asymptotic expansion of Θ' for an arbitrary external velocity is helpful. Introducing the expansion for Q given by Eq. (5.44) inside the integral in Eq. (5.47) leads to an asymptotic expansion of Θ' in terms of ϵ. Expanding the corresponding leading-order term for small values of R, as is explained with more details in Appendix C, where use is made of the variable $\xi = \sqrt{\sigma/\hat{\tau}}/2$, gives

$$\Theta' \sim \frac{(1+B)\ln(1+B)}{B}\left\{\frac{1}{R} - \Gamma + \mu\frac{\sigma U}{2}\right\} + O(R), \tag{48}$$

with

$$\Gamma = \frac{2}{\sqrt{\pi}}\int_0^\infty \left(1 - e^{-\sigma Y^2\xi^2}\right) d\xi \tag{5.49}$$

and $Y = \int_{\tau-\sigma/4\xi^2}^{\tau} U(\tau')d\tau'$. The integral in Eq. (5.49) needs to be evaluated numerically for general expressions of the external velocity. The angular-dependent part of the expansion in Eq. (5.48) may be seen by comparison with Eq. (5.40), (5.41) and (5.42) to match automatically with the inner solution, which is quasisteady. Only the angular-independent part of the perturbation of the outer temperature depends on the vaporization history through Γ, which is related to g_∞ by matching with the inner solution. Comparing Eqs. (5.45) and (5.48) with Eqs. (5.40) and (5.41) demonstrate that matching requires

$$g_\infty U = \frac{b_0(1+B)}{B}\Gamma, \tag{5.50}$$

with b_0 given by Eq. (5.19).

In order to obtain closure of the complete solution for the temperature and velocity fields up to terms of order ϵ^2, the first perturbation of the stream function Ψ' must also be obtained. To acomplish that, it is convenient to consider the outer velocity field, which can be written in terms of the expansion

$$\vec{V} = U\vec{e}_x + \epsilon\vec{V}'. \tag{5.51}$$

The perturbation $\vec{V}'$ satisfy the continuity and momentum-conservation equations

$$\widetilde{\nabla}\cdot\vec{V}' = M\delta^3(\vec{R}) \tag{5.52}$$

and

$$\frac{\partial\vec{V}'}{\partial\tau} + \widetilde{U}\frac{\partial\vec{V}'}{\partial X} + \widetilde{\nabla}P' - \widetilde{\nabla}^2\vec{V}' = -(F/\epsilon)\vec{e}_x\delta^3(\vec{R}), \tag{5.53}$$

with boundary conditions $\vec{V}' = P' = 0$ at infinity. Here $P' = p'/\epsilon^2$ denotes the nondimensional ratio of pressure to density in the outer region. The right-hand sides of Eqs. (5.52) and (5.53) represent a point mass source and point force, respectively, both located at the center of the droplet, where the stregths M and F are given by Eqs. (5.37) and (5.39), respectively.

The solution for $\vec{V}'$ can be written uniquely by superposition of an irrotational velocity field generated by the mass source and a rotational velocity field generated by the component of the point force associated with the rotational part of the inner velocity field in the absence of the mass source, giving

$$\vec{V}' = \frac{b_0 + \epsilon g_\infty B/(1+B)}{R^2}\vec{e}_r + \vec{V}'_R. \tag{5.54}$$

The first component of $\vec{V}'$ in Eq. (5.54) is purely radial, the associated stream function being $\mu[b_0 + \epsilon g_\infty B/(1+B)]$, which matches with the radial irrotational part of the inner velocity field. Its interaction with the external velocity $U\vec{e}_x$ has a contribution of $4\pi\epsilon U b_0$ to the stregth of the point force F. Therefore, the rotational component of the outer velocity field $\vec{V}'_R$, which is solenoidal, satisfies the momentum conservation equation

$$\frac{\partial \vec{V}'_R}{\partial \tau} + \widetilde{U}\frac{\partial \vec{V}'_R}{\partial X} + \widetilde{\nabla} P'_R - \widetilde{\nabla}^2 \vec{V}'_R = 6\pi U \frac{(3+\chi)b_0^3}{9A_1}\vec{e}_x \delta^3(\vec{R}), \tag{5.55}$$

with boundary conditions $\vec{V}'_R = P'_R = 0$ at infinity.

The solution to Eq. (5.55) was first obtained by Ockendon [31] by means of a Fourier transform. He derived an expression for the associated stream function, denoted here by Ψ_R, written in terms of a double integral. A simplified expression for Ψ_R was obtained later by Asmolov [34] in terms of a single integral, in time, of a Greens function. This result can be written, in the notation used here, as

$$\Psi'_R = -\frac{(3+\chi)b_0^4}{12A_1\sqrt{\pi}}\int_{-\infty}^{\tau}\left\{\left[2U(\tau_0)\hat{\tau} - \mu R - Y\right]e^{-\hat{R}^2/4\hat{\tau}} + \mu R e^{-R^2/4\hat{\tau}}\right\}$$

$$\times \left[e^{-(1-\mu^2)R^2/4\hat{\tau}} - 1\right] \frac{d\tau_0}{\hat{\tau}^{3/2}}, \tag{5.56}$$

where $\hat{\tau}$ and $\hat{R}$ have been defined previously in connection with Eq. (5.47). The rescaled vorticity in the outer region, $\widetilde{\omega} = \omega/\epsilon^3$, can be expressed in terms of the outer streamfunction as $\widetilde{\omega} = -\sqrt{1-\mu^2}\widetilde{D}^2\Psi'_R/R$, with $\widetilde{D}^2$ being the operator defined in Eq. (5.12) but in terms of outer variables. Introducing the expression for Ψ'_R given by Eq. (5.56) into this formula for $\widetilde{\omega}$ gives

$$\widetilde{\omega} = \frac{(3+\chi)b_0^4}{12A_1\sqrt{\pi}} \frac{\sqrt{1-\mu^2}}{R} \int_{-\infty}^{\tau} G(R,\tau,\tau_0)d\tau_0, \tag{5.57}$$

with

$$G(R,\tau,\tau_0) = \frac{1}{\hat{\tau}^{3/2}} \left\{ \left[\frac{2U(\tau_0)\hat{\tau} - Y}{2\hat{\tau}} \left(\frac{\hat{R}^2}{2\hat{\tau}} - 1 \right) + \right.\right.$$
$$\left.\left. \frac{3\mu R - 2Y}{2\hat{\tau}} - \frac{\mu R \hat{R}^2}{4\hat{\tau}^2} \right] e^{-\hat{R}^2/4\hat{\tau}} \left(e^{-(1-\mu^2)R^2/4\hat{\tau}} - 1 \right) +$$

$$\left[\frac{2U(\tau_0)\hat{\tau} - Y}{2\hat{\tau}} \left(\frac{3R^2}{2\hat{\tau}} - 1 \right) - \frac{\mu^2 R^2[\mu R + Y(1+\mu)]}{4\hat{\tau}^2} \right] (1-\mu^2) e^{-(\hat{R}^2 - (1-\mu^2)R^2)/4\hat{\tau}} -$$

$$\left. \left[\frac{3\mu R}{2\hat{\tau}} - \frac{\mu R^3}{4\hat{\tau}^2} \right] e^{-R^2/4\hat{\tau}} \left(e^{-(1-\mu^2)R^2/4\hat{\tau}} - 1 \right) \left[\frac{\mu R}{2\hat{\tau}} + \frac{\mu R^3}{2\hat{\tau}^2} \right] e^{-\mu^2 R^2/4\hat{\tau}} \right\}. \tag{5.58}$$

The asymptotic expansion of Ψ_R for small R can be used to determine perturbations of the velocity field of order ϵ^2 in the inner region. Expanding the integral in Eq. (5.56) for small values of R, which is explained with more details in Appendix E, gives

$$\Psi'_R = \frac{(3+\chi)b_0^4}{A_1} \frac{(1-\mu^2)}{12} \left\{ UR + \left[\mu \frac{U^2}{4} - \Pi \right] R^2 \right\} \tag{59}$$

with

$$\Pi = \frac{2}{\sqrt{\pi}} \int_0^{\infty} \xi'^{-2} \left[(U - 2Y/\xi'^2) e^{-Y^2\xi'^{-2}} - U(\tau) e^{\mu R U(\tau)/2\}} \right] d\xi'. \tag{60}$$

This result can be used to obtain an expansion of Ψ, given by Eq. (E18) in Appendix E, which matches with the expansion of ψ for large values of r, given by Eq. (E5) in the same Appendix.

The expressions obtained for Γ and Π allow for general time variations of the external velocity. Different vaporization histories will result by considering specific problems.

5.6 Acceleration From Rest And Deceleration From Constant Velocity

Specific results for a translating droplet that begins to accelerate from rest or decelerate from constant velocity u_e at $\tau = 0$ are derived in this section. The nondimensional external velocity can be written in general form as

$$U = U_0 + \gamma c^2 \tau \tag{5.60}$$

for $\tau > 0$ and $U = U_0$ for $\tau < 0$, where U_0 denotes the nondimensional initial velocity, c denotes the ratio of the characteristic diffusion time in the outer region to the characteristic time of variation of the external velocity, and the two-value parameter γ is 1 for acceleration and -1 for deceleration. If the droplet is initialy at rest, U_0 is zero in this notation, and $c = 1$, as explained in deriving Eq. (5.3), which applies in this case. If the droplet accelerates or decelerates from constant velocity, U_0 is 1 and $c = \sqrt{d^2 a/(4\nu\epsilon^2 u_e)}$, the initial constant velocity being the velocity scale.

An expression for g_∞ can be obtained from Eq. (5.50) by splitting the integral in Eq. (5.49) into two parts, $\int_0^{sqrt\sigma/\tau/2} + \int_{sqrt\sigma/\tau/2}^{\infty}$. The first of these integrals would correspond to $\tau < 0$ in Eq. (5.60), so that $U = U_0$ and $Y = U_0\sigma/(4\xi^2)$ according to the definition following Eq. (5.49), while Eq. (5.60) applies for the second integral, and $Y = \sigma[U_0 + \gamma c^2 Y - \sigma/(8\xi^2)]/(4\xi^2)$. The first integral can be expressed in terms of tabulated functions, but the second cannot. In the

second, it is useful to define $y = \sqrt{\sigma/\tau}/(4\xi) = \sqrt{\hat{\tau}/\tau}/2$, and it can then be shown from Eq. (5.49) that Eq. (5.50) can be written as

$$g_\infty U = \frac{(1+B)\ln(1+B)}{2B}\left\{U_0\left[1 - erf(U_0\sqrt{\sigma\tau}/2)\right] + \frac{2}{\sqrt{\sigma\pi\tau}}\left[1 + \Lambda - e^{-\sigma U_0^2\tau/4}\right]\right\}, \tag{5.61}$$

with

$$\Lambda = \int_0^1 y^{-2}\left\{1 - e^{-(\sigma/4)\tau y^2[U_0+\gamma c\tau(1-y^2/2)]^2}\right\}dy. \tag{5.62}$$

For a droplet accelerating from rest $c = 1$ with ϵ given by Eq. (5.3), and by putting $z = y\sqrt{\sigma\tau^3}/2$ Eqs. (5.61) and (5.62) can be simplied to give

$$g_\infty = \frac{(1+B)\ln(1+B)}{2\pi B}\int_0^{\phi(\tau)} z^{-2}\{1 - exp(-z^2[1 - z^2/\phi(\tau)^2]^2)\}dz, \tag{5.63}$$

with $\phi(\tau) = \sqrt{\sigma\tau^3}/2$. Numerical integration of this integral produces the solid curves shown in Fig. 5.11. According to Eq. (5.41), the increase in the apparent external temperature caused by the acceleratin is proportional to $\epsilon U\sigma g_\infty$, which, since $U = \tau$ here according to Eq. (5.60), is seen from Eqs. (5.3) and (5.63) to be $(d/2)a^{1/3}(\nu/,a)^{-2/3}[(1+B)/B][\ln(1+B)]$ multiplied by a function of $\sigma^{1/3}\tau$, the nondimensional time variable τ being the physical time multiplied by $(a^2/\nu)^{1/3]}$. These results indicate that the relevant parameter for nondimensionalizing the time is $(a^2\sigma/\nu)$, that is, the thermal diffusivity, rather than the kinematic viscosity, determines the time scale of temperature evolution under the imposed acceleration. In addition, the Peclet number $(d/2)a^{1/3}(\sigma/\nu)^{2/3}$, rather than the Reynolds number, is the appropriate small parameter, and with these revisions, the dependence on the Prandtl number disappears. The dependence on the transfer number is exactly the same as it is for the quasisteady problem with a constant imposed external velocity discussed following Eq. (5.41). Until τ becomes of order unity, the droplet is evaporating under the influence of the initial temperature field generated by the evaporating droplet at rest, so that the increase of $g_\infty U$

with time is small, especially at earlier times. The effect of the initial temperature field becomes more important with decreasing Prandtl numbers at fixed kinematic viscosity, since the heat transfer to the inner region increases with the thermal conductivity. For $\tau \gg 1$ the integral in Eq. (5.63) approaches $\sqrt{\pi}$, so that the expression for $g_\infty U$ approaches that corresponding to a quasisteady outer solution, $g_\infty U = [(1+B)\ln(1+B)/2B]\tau$, which is represented by the dashed line in Fig. 11b.

The case of droplet deceleration from a constant velocity is represented in Fig. 5.12, which shows variations of $2Bg_\infty U/[(1+B)ln(1+B)]$ with time for three different values of σ with $c = 1$. The values of $g_\infty U$ are calculated from Eqs. (5.61) and (5.62) with $U_0 = 1$ and $\gamma = -1$. At $\tau = 0$ the droplet is evaporating steadily at constant velocity, so the classical result $g_\infty U = \sigma b_0(1+B)/2B$ is obtained. As the external flow decelerates, perturbations of the external temperature tend to move away from the droplet surface so that the rate of heat transfer to the inner region and, therefore, the vaporization rate, decrease. At $\tau = 1$ the droplet is at rest; however, there still is a positive value of $g_\infty U$ which decreases as σ increases for constant kinematic viscosity, indicating that, even in the absence of a convective velocity, there exists a remaining perturbation of the temperature field that increases the vaporization rate in this time-varying situation.

The nondimensional temperature perturbation in the outer region can be evaluated numerically from Eq. (5.47) for these two problems. The results of the numerical integration are shown in Fig. 5.13. The temperature decrease with decreasing radius at different times and the approach to the limiting value obtained from Eq. (5.50) are readily apparent in this figure, in which the dominant term, proportional to $1/R$ which is seen in Eq. (5.48), has been substracted for greater clarity.

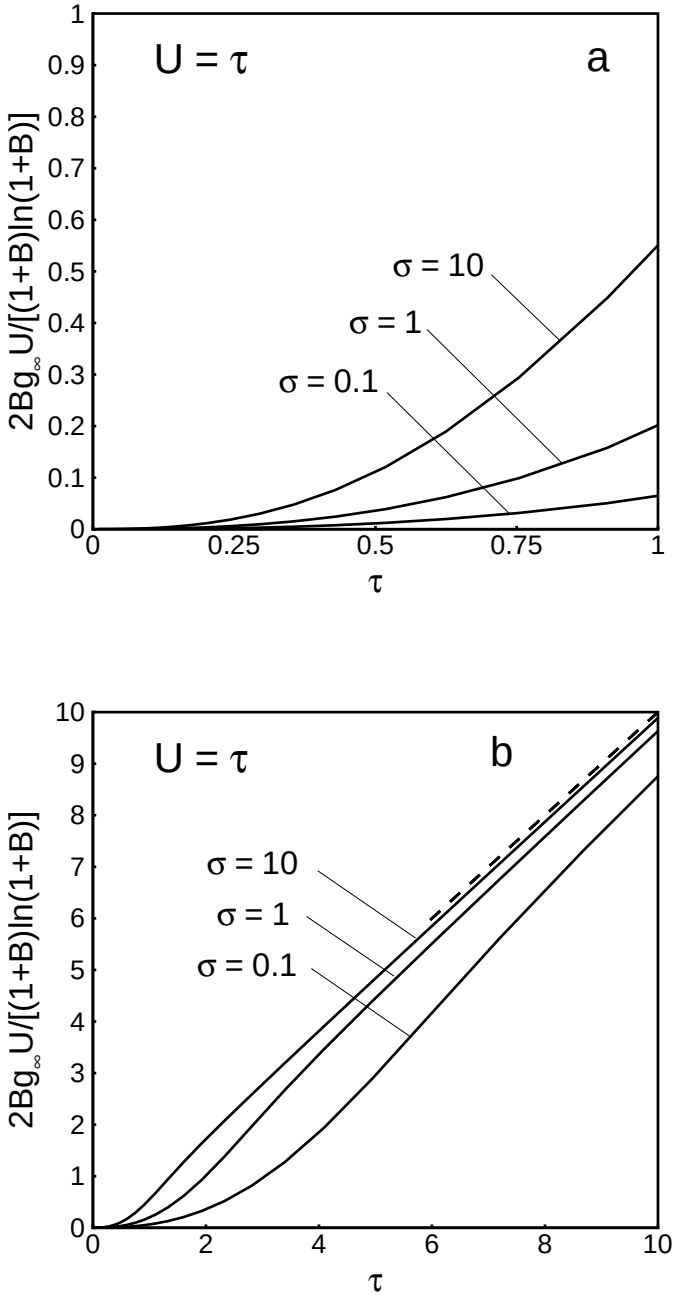

Figure 5.11 Variations of $2Bg_\infty U/[(1+B)ln(1+B)]$ with the nondimensional time, the ratio of the time to the characteristic time $(a^2/\nu)^{-1/3}$, evaluated from Eq. (5.63) for three different values of the Prandtl number ($\sigma = 0.1, 1$ and 10).

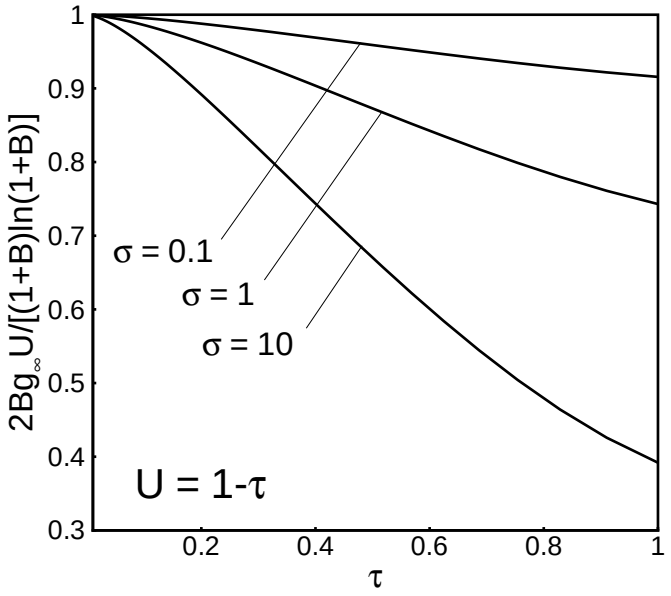

Figure 5.12 Variations of $2Bg_\infty U/[(1+B)ln(1+B)]$ with time evaluated from Eqs. (5.61) and (5.62) for three different values of the Prandtl number ($\sigma = 0.1, 1$ and 10) and $c = 1$, $U_0 = 1$ and $\gamma = -1$

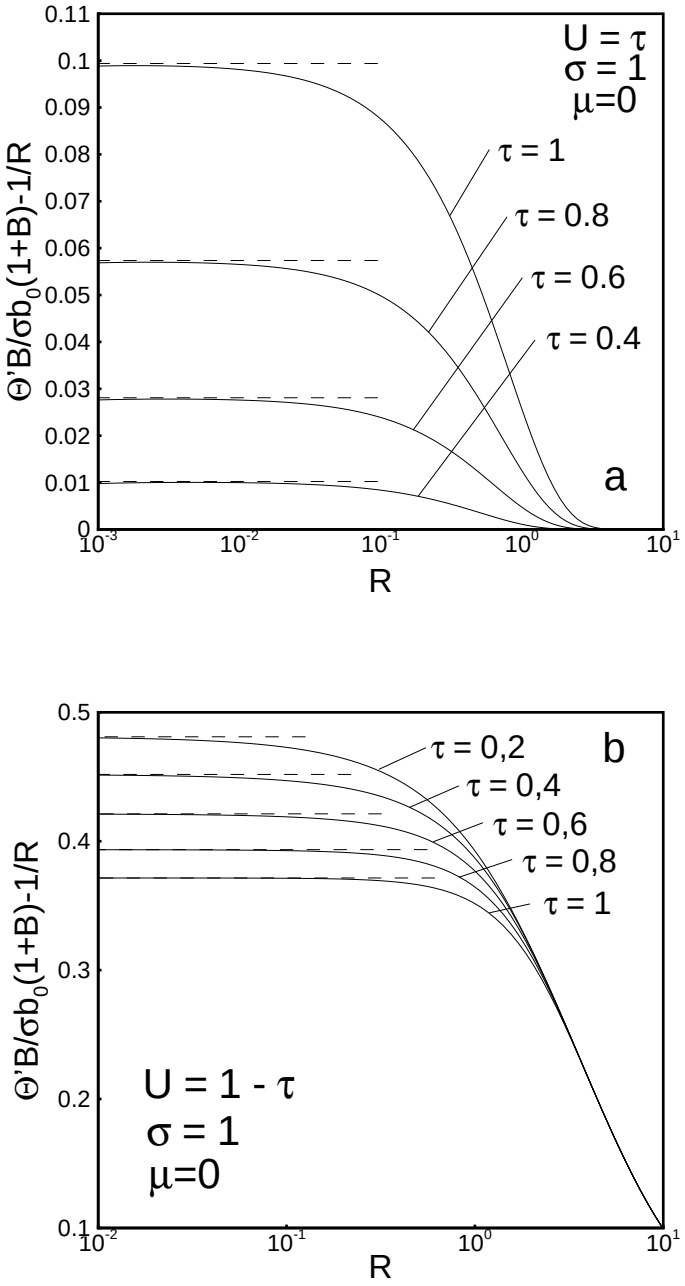

Figure 5.13 Variations of $\Theta' B/(\sigma b_0(1+B)) - 1/R$ with R, obtained by numerical evaluation of Eq. (5.47) and values of $g_\infty UB/[b_0(1+B)]$, calculated from Eq. (5.50), for a: droplet acceleration from rest ($U_0 = 0$, $\gamma = 1$), and for b: droplet deceleration from constant velocity ($U_0 = 1$, $\gamma = -1$).

5.7 Oscillatory Motion

For a droplet evaporating in oscillatory motion, the nondimensional external velocity can be written in general form as

$$U = U_m + W\cos(c\tau), \tag{5.65}$$

with U_m denoting the mean velocity, W the constant amplitude and c the nondimensional frequency normalized with the inverse of the characteristic diffusion time in the outer region t_o^{-1}. Typically the mean velocity is used as the velocity scale, so that $U_m = 1$ in this notation. For pure oscillatory motion with zero mean velocity ($U_m = 0$), the amplitude of the velocity fluctuations becomes the appropriate velocity scale; therefore $W = 1$. Introducing the definition of U in Eq. (5.64) into Eq. (5.49) gives an expression for $g_\infty U$ that can be written as

$$g_\infty U = \frac{(1+B)\ln(1+B)}{B}\frac{2}{\sqrt{\pi}}\int_0^\infty [1- \\ exp\left\{-\left(\frac{U_m y}{4} + \frac{\sigma W}{cy}\left[\sin(c\tau) - \sin(ct - cy^2/4)\right]\right)^2\right\}]\frac{dy}{y^2}, \tag{5.65}$$

where the integral needs to be evaluated numerically. Variations of $Bg_\infty U/[\sigma(1+B)]$ for oscillatory external velocity calculated from Eq. (5.65) are plotted as functions of a normalized time in Fig. 5.14 over one period of oscillation, for $\sigma = 1$ and different values of c. Figure 5.14a represents the case of oscillatory motion with mean velocity and $W = 1$, and Fig. 5.14b represents the case of pure oscillatory motion with zero mean velocity. In the limit $c = 0$, it can be shown from Eq. (5.65) that $g_\infty U = [(1+B)\ln(1+B)/(2B)]|U_0 + W cos(c\tau)|$, which is the result corresponding to a quasisteady outer solution, plotted as dashed curve in Fig. 5.14 for the two cases represented. For any other frequency of the external velocity represented in Fig. 5.14, $g_\infty U$ appears to be periodic with frequency c, the amplitude decreasing and the phase shifting as the frequency increases. The results in Fig. 5.14b are different to the results obtained by Pozrikidis [111] for

pure uniform oscillatory motion, in which there is no phase shift as the frequency increases. Except for this difference, the discussion by Pozrikidis [111] applies.

5.8 Concluding Remarks

The first-order asymptotic analysis presented here shows that the solution near the surface of a droplet evaporating in a slowly-varying flow at low Reynolds number is shown to be quasisteady except during short periods of time, on the order of the characteristic diffusion time based on the droplet diameter, when the droplet acceleration changes abruptly. The unsteadiness due to the time variation of the relative velocity between the droplet and the external flow affects only the perturbation of the temperature and velocity field in the Oseen region, written in terms of time-history integrals, and the vaporization rate through the angular-independent apparent external temperature, which increases with increasing external velocities.

Closed-explicit expressions for the quasisteady perturbations of the temperature and the velocity field in the inner region have been written in terms of the transfer number, the Prandtl number and the nondimensional time, in simpler forms than those that can be found in the literature, revealing certain properties of the solution in this region not seen before. Although the unperturbed vaporization rate b_0 decreases with decreasing Prandtl number, lower thermal conductivities and larger transfer numbers increase the perturbation of the vaporization rate, by increasing the apparent external temperature, and enhance its angular dependence, the vaporization rate becoming larger in the upstream direction and smaller in the downstream direction. For Prandtl numbers below the critical value $\sigma = 7/3$, the drag decreases with b_0 for low and moderate vaporization rates, reaching a minimum that decreases with decreasing Prandtl number. In the limit $\sigma = 0$, the drag is a monotonically decreasing function of b_0 and vanishes as b_0 tends to infinity. For large vaporization velocities the vorticity region is flown away from the droplet surface, the solution at the vicinity of the droplet becoming isothermal and

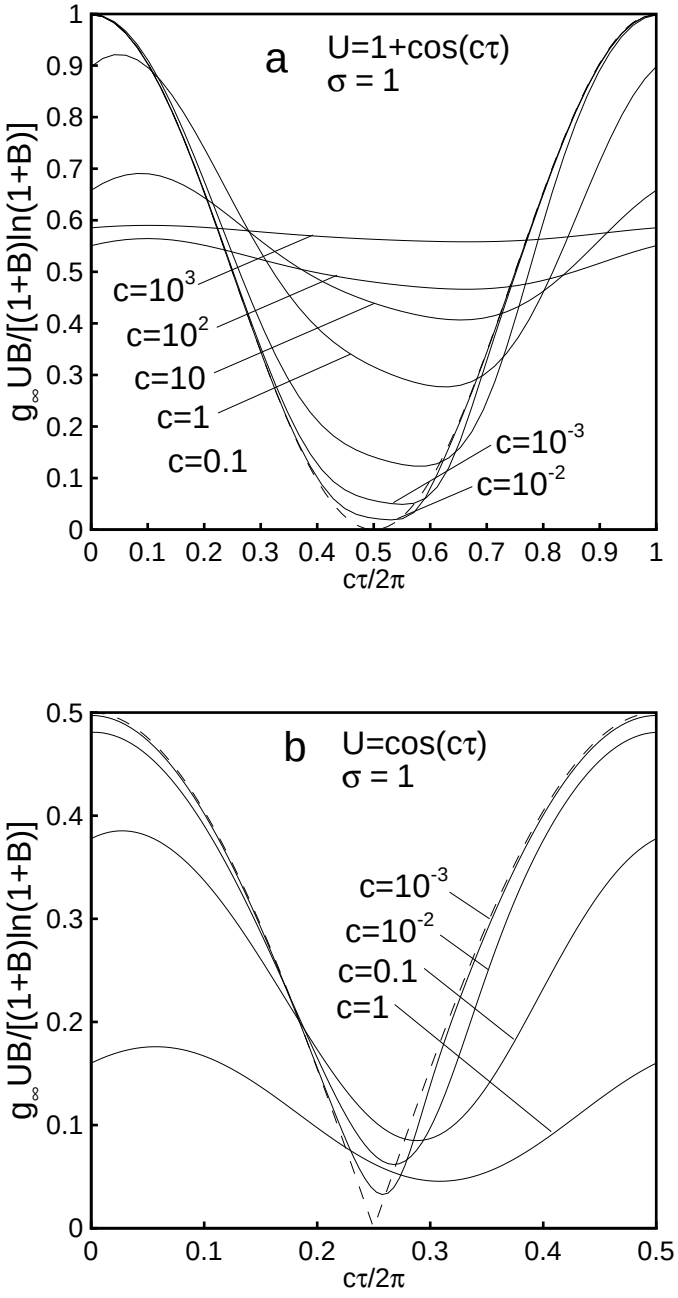

Figure 5.14 Variations of $Bg_\infty U/[\sigma(1+B)]$ with τ for oscillatory external velocity calculated from Eq. (5.65) over one period of oscillation, for $\sigma = 1$ and different values of the nondimensional frequency c for a: oscillatory motion with mean velocity and $W = 1$ for $c = 10^{-3}, 10^{-2}, 10^{-1}, 1, 10, 10^2$ and 10^3, and for b: pure oscillatory motion with zero mean velocity and $c = 10^{-3}, 10^{-2}, 10^{-1}$ and 1.

irrotational. In this large-b_0 limit, a transition mixing region develops at radial distance of order b_0^{-1} due to the interaction of the source flow with the externally imposed uniform flow, creating a negative pressure gradient in the tangential direction on the droplet side that reverses flow. The velocity and pressure fields near the droplet surface in the strong-vaporization limit depends only on the Prandtl number through the angular-dependent part of the vaporization rate, as it does the drag, which decreases with the Prandtl number and is mainly due to momentum, pressure forces having a negative contribution to the drag.

Sufficiently far from its surface, the droplet behaves like a point source of mass and heat, their strength increasing with the external velocity, the transfer number and the thermal conductivity, and like a point force pointing upstream in the axial direction and with strength equal to the drag. These approximations allows the solutions of the Oseen region to be written as single time-history integrals of Green functions. Particular results for a translating droplet that accelerates slowly from rest reveals that, until times in the order of the characteristic diffusion time of the Oseen region, the droplet evaporates under the influence of the initial temperature field generated by the droplet evaporating at rest and the apparent external temperature is smaller than the corresponding to a quasisteady solution, higher thermal conductivities increasing this effect. If the droplet decelerates from constant velocity, the heat transfer and, consequently, the vaporization rate decrease much slower than those corresponding to a quasisteady solution. Perturbations of the temperature in the Oseen region remains even in abscence of forced convection, higher thermal conductivities increasing the apparent external temperature. For a droplet moving in oscillatory motion, it is seen that the time variation of the apparent external temperature is periodic with the same frequency than the external velocity, but the amplitude decreases and the phase shifts as the frequency increases, correcting a previous result obtained by Pozrikidis [38].

Chapter 6

Future Work

In this chapter, a number of potential research topics related to the present dissertation and believed to be the subject of future investigations will be presented.

6.1 Hydrogen Ignition

There are accident scenarios that involve low temperatures and long autoignition times, which motivates future studies in this direction. For this reason the ignition of hydrogen-oxygen mixtures near and below the crossover limit, where the recombination rate $H+O_2+M \rightarrow HO_2+M$ equals the branching rate $H+O_2 \rightarrow O+OH$, deserves more attention. The asymptotic analysis presented in Chapter 4, based on small initiation rates, fails as crossover is approached, as the net rate of radical production $B_0(1-c)$, the difference between the branching rate and the recombination rate, becomes small. The ignition times near crossover become long, pointing towards the need for a revised nondimensionalization of the time using $[B_0(1-c)]^{-1}$ as a more appropriate time-scale. The resulting problem can be expressed in terms of two small parameters and different kinds of expansions are needed for the solution, which could profitably be investigated in the future, as explained with more details in Appendix B. Studies of autoignition of hydroen-oxygen mixtures below the crossover limit implies investigation of an alternative

reduction of chemistry under these conditions, possibly including the effect of HO_2 consumption.

Since applications in aerospace propulsion, of the kind encountered in hydrogen-fueled supersonic-combustion ramjets, for example, often encounter quite fuel-lean conditions, it could be of interest to extent the high-temperature analysis presented in Chapter 4 to account for two radicals (O and OH) not being in steady-state, with the H atom in steady-state. This implies reduction of chemistry from the five-step mechanism presented in Chapter 5, incorporating the chain-breaking effect of the elementary reaction $OH+OH \rightarrow H_2O+O$ at very lean mixtures. The resulting problem, whose formulation includes conservation equations of energy and of O and OH radicals, can be solved by asymptotic methods based on the small initiation rates and the large activation energy of the branching steps to obtained well-justified closed-form expressions for autoignition times under those conditions.

6.2 Droplet Combustion

As it was mentioned in the Introduction, the ultimate interest of the study addressed in Chaper 5 is to consider effects of non-spherical time-dependent convection on the combustion of fuel-droplets, which is taking place in a diffusion flame formed betweeen the fuel and the oxydizer sides. The difficulty in the theoretical analysis of this problem comes mainly from the effect of heat release associated with the chemical reactions, which creates typically large variations of temperature within the flow field so that the dependence of the density and the transport properties on the temperature needs to be included in the analysis. In addition, real fuel-combustion chemistry occur through a large number of elementary chemical reactions, whose rates are nonlinearly temperature-dependent, involving a large number of species. The mathematical description then includes coupled mass, momentum, species and energy conservation equations with chemical terms.

One first step before including the effect of the real fuel-oxydation chemistry would be to investigate the vaporization with combustion of fuel-droplets in slowly-varying flow at low-Reynolds numbers with variable density and transport properties and the chemistry being simplified to one irreversible, infinitely-fast overall step. Assuming lewis number unity for the fuel and the oxydizer in this Burke-Schumann approximation, the formulation can be simplified by expressing the concentration of species and the temperature in terms of coupling functions which are independent on the chemical terms [2,3]. A formal asymptotic analysis similar to the one presented in Chapter 5 can be performed, with a nearly quasisteady inner region at the vicinity of the droplet and a fully time-dependent outer region at distances of order the ratio of the droplet diameter to the Reynolds number. The solutions then can be written in terms of matched asymptotic expansions. In this analysis, different limits appear depending on the location of the flame relative to the droplet surface, which can be estimated as the product of the droplet diameter and the so-called overall stoichiometric ratio S, defined as the stoichiometric mass of oxydizer consumed per unit mass of fuel. For the combustion of high hydrocarbon fuels such as propane and heptane, in air, the overall stoichiometric ratio S is typically large so that, for Reynolds number of order S^{-1}, the flame will be located in the outer region. In this limit, the thermal expansion due to large variations of density needs to be included in the leading-order analysis of the outer region, but a constant-density approximation for the inner region might be still justified since variations of temperature occur in large radial distances. For values of S of order unity the flame will be located in the inner region, large variations of density existing at the vicinity of the droplet surface. In this limit the inner solution can be assumed to be spherico-symmetrical at leading order in the Reynolds number and a constant-density approximation can be used to calculate perturbations of the solutions in the outer region. For Lewis number different to unity, it is still possible to formulate the problem in terms of generalized coupling functions, but the analytical description becomes very complicated,

requiring significant computational work.

The incorporation of finite-rate chemistry in the analysis relies on the utilization of systematically reduced mechanisms. The simplest approach is to simplify the chemistry to one global step, believed to describe the overall effect of the reactants consumption and the heat release. The typically-large activation energy of the overall-reaction rate allows to study analytically the problem by using asymptotic methods based on Damkohler number, which represents the ratio of the characteristic time of the transport phenomena to the characteristic chemical time. Finally, more complicated descriptions of simplified chemistry including intermediate species out of steady state can be incorporated.

Appendix A

Asymptotic Formulas of t_R and t_L in Terms of the Rate Constants and Molar Concentrations.

The asymptotic formulas (3.14) and (3.16) for induction time can be written in terms of rate constants, k_i, and molar concentrations, c_i:

$$t_R = \frac{1}{c_{O_2}(2k_2 - k_5 c_M)} \ln\left(\frac{2K_2\phi(1 - k_5 c_M/2k_2)k_3 k_4}{k_2 k_1}\right) \qquad (A1)$$

and

$$t_L = \frac{1}{\sqrt{2c_{H_2}^2 k_3 k_4}} \left\{ \left[\frac{k_2 - k_5 c_M/2}{k_2 + k_5 c_M} + \left(\frac{k_5 c_M}{k_5 c_M + k_2}\right)^2 \frac{(k_3 + k_4)^2}{8k_3 k_4} \right]^{1/2} \right.$$
$$\left. - \left(\frac{k_5 c_M}{k_5 c_M + k_2}\right) \frac{(k_3 + k_4)}{\sqrt{8k_3 k_4}} \right\}^{-1} \ln\left(\frac{8K_2\phi k_3 k_4}{k_2} \frac{1 + \sqrt{k_3/2k_4}}{k_1 + \sqrt{2k_3/k_4}}\right), \qquad (A2)$$

where $c_M = 0.3c_{O_2} + 12.0c_{H_2O} + 1.0c_{N_2} + 0.5c_{Ar}$ denotes the effective chaperon concentration.

Equation (A1) is generally more useful than (A2) because its validity extends from very rich conditions nearly to stoichiometric conditions, while the latter is restricted to equivalence ratios less than about 0.1. At sufficiently high temperatures, the ratio of $k_5 c_M$ to $2k_2$ is much less than unity, so that equation

(A1) reduces approximately to

$$t_R = \frac{1}{2k_2 c_{O_2}} \ln\left(\frac{2\phi k_3 k_4}{k_{2b} k_2}\right), \qquad (A3)$$

where k_{2b} is the specific reaction-rate constant of the backward step 2 in Table 3.1. This equation shows the dominant influence of the rate of the forward branching step 2 on the induction time and its temperature dependence at high temperature. The dependence on branching by step 2 is modified only logarithmically by initiation (steps 1 and 2) and the ratio of branching through O and OH attack on H_2 (steps 3 and 4) to the backward shuffle through collision of O and OH (step 2b). The high-temperature effect of these logarithmic influences is to reduce the strength of the temperature dependence somewhat below that associated with the H+O_2 branching step 2 because the temperature dependence of initiation is much stronger than that of branching, but this effect is not large. The $\ln\phi$ dependence on the equivalence ratio is responsible for the increase in induction time with ϕ.

At lower temperatures, as crossover is approach, the largest modification to equation (A3) is a factor of $1-(k_6 c_M/2k_3)$ in the denominator, which increases the ignition time and its temperature dependence, causing it to approach to infinity at crossover. The recombination thus is responsible for the increase in slope with decreasing temperature in Fig. 3.1. The same factor is seen to also appear inside the logarithm in equation (A1), tending to offset the dependence outside the logarithm, but being inside it is weaker, so that the outside dependence dominates and derives t_R to infinity at crossover in this approximation.

Under very lean conditions it is seen from equation (A2) that the behavior is quite different. At high temperature, the dominant factor in t_L outside the logarithm becomes $(2c_{H_2}^2 k_3 k_4)^{-1/2}$, demonstrating the controlling character of the chain-branching step 3 and the straight-chain step 5 of Table 3 and the irrelevance of the H+O_2 branching step 2, which is now fast compared with the other two chain steps at these very lean conditions where there is little H_2 available to allow the essential steps 4 and 5 to proceed. As crossover is approached, like t_R, t_L also approach infinity, as may be seen from the limiting value of the expression

in braces in equation (A2). This is the main factor modifying the slope for lean mixtures in Fig. 3.1.

Appendix B

Asymptotic Behaviour of τ_∞ Near Crossover

The result in Eq. (4.18) suggests that, when $c < 1$, the most natural nondimensional time and small parameter ϵ for the analysis in the main text are

$$\tau = B_0(1-c)t, \qquad \epsilon = A_0(\alpha_b + \alpha_r c)/[B_0(1-c)^2], \tag{B1}$$

because then Eq. (4.18) is simply $\tau_\infty = \ln(1/\epsilon) - K(b,c)$. In terms of the parameters in Eq. (B1), Eq. (4.6) is

$$\frac{d^2\theta}{d\tau^2} = -ia\epsilon(1-c)e^{i\theta}\frac{d\theta}{d\tau} + \epsilon e^{i\theta}\left(\frac{e^\theta + bc}{1+bc}\right) + \left[\left(\frac{e^\theta - c}{1-c}\right) + \left(\frac{e^\theta d\theta/d\tau}{e^\theta + bc}\right)\right]\left[\frac{d\theta}{d\tau} + a\epsilon(1-c)e^{i\theta}\right], \tag{B2}$$

with initial conditions $\theta = 0$ and $d\theta/d\tau = a\epsilon(1-c)$ at $\tau = 0$. This modified formulation may facilitate analysis of the limit in which $(1-c)$ becomes small, approaching crossover, but it becomes singular and not useful at crossover ($c = 1$). Different regimes arise as crossover is traversed, necessitating different types of matched asymptotic expansions. Since attempts to explore these regimes systematically would complicate and lengthen the presentation appreciably, and since for aerospace propulsion application there is less interest in the long ignition times

encountered near and beyond crossover, the discussion here is restricted to a few general observations.

It is evident from Eq. (4.4) that, since $X = 0$ at $t = 0$, $d\theta/dt$ initially is negative when $a > 0$ and positive when $a < 0$, that is, for endothermic initiation ($a > 0$) there is a small temperature decrease initially, which is of higher order and unimportant when $(1 - c)$ is positive and not small. For exothermic initiation ($a < 0$) with $i > 0$, in extreme cases it is possible to encounter thermal runaway in the initiation step itself on the long time scale A_0^{-1}, the branching and recombination playing no role whatever; this simple limit is not of interest for branched-chain explosions. For sufficiently endothermic initiation, specifically for $\alpha_i > \alpha_r$, Eqs. (4.4) and (4.5) possess a steady-state solution having both $dX/dt = 0$ and $d\theta/dt = 0$. This solution, which has $\theta = \ln[c(\alpha_i - \alpha_r)/(\alpha_i + \alpha_b)]$, is most accessible below crossover ($c > 1$) and is irrelevant for $c < 1$, where it corresponds to a negative value of θ that is never reached from the initial state. For $c > 1$, thermal runaway can occur from the steady state on the long time scale A_0^{-1}. Near crossover thermal runaways are possible on shorter time scales, not achieving steady states. For example, for $1 - c \geq 0$ and small, and for small ϵ, there exists a three-zone matched asymptotic expansion that exhibits thermal runaway on a shorter time scale, intermediate between A_0^{-1} and B_0^{-1}. There would be some interest in exploring these regimes further, for example in connection with concerns about hydrogen safety.

Appendix C

The Constants Of Integration K_1, K_2, K_3 and K_4 In The Quasisteady Inner Solution

The constant of integration K_1, K_2, K_3 and K_4 in Eqs. (5.25) and (5.33) can be written as

$$K_1 = \frac{2}{(\sigma b_0)^2}\left(\sigma b_0 - 1 + e^{-b_0\sigma}\right), \tag{C1}$$

$$K_2 = \frac{2}{(\sigma b_0)^3}\left[\sigma b_0 - 2 + (\sigma b_0 + 2)e^{-\sigma b_0}\right], \tag{C2}$$

$$K_3 = \frac{2}{(\sigma b_0)^3}\left[\frac{1}{2}(\sigma b_0)^2 - 2\sigma b_0 + 3 - (\sigma b_0 + 3)e^{-\sigma b_0}\right] \tag{C3}$$

and

$$K_4 = \frac{1}{30\sigma^3 b_0^2}\left\{\left[\sigma^5 \ln\left(\sigma^{-1}+1\right) + (10\sigma^2 + 15\sigma + 6)\ln(1+\sigma) - \sigma^4 + \sigma^3/2 - 12\sigma^2 - 6\sigma\right] b_0^4 - 10\sigma^2 b_0^3 + 10\sigma b_0^2 + 4\sigma^2 b_0 - 6\sigma + \left[-\sigma^2 b_0^5 + (\sigma^2 + 4\sigma)b_0^4 + (8\sigma^2 + 11\sigma)b_0^3 - (4\sigma^2 + 7\sigma)b_0^2 - (4\sigma^2 - 6\sigma)b_0 + 6\sigma\right] e^{-b_0} + \left[\sigma^4 b_0^3 - (\sigma^3 + 10\sigma)b_0^2 + 2\sigma^2 b_0 + 6\sigma\right] e^{-\sigma b_0} + \left[2\sigma b_0^4 - (\sigma^4 - \sigma^3 + \sigma^2 + 11\sigma)b_0^3 + (\sigma^3 - 2\sigma^2 + 7\sigma)b_0^2 - 2(\sigma^2 + 3\sigma)b_0 - 6\sigma\right] e^{-(1+\sigma)b_0}$$

$$+\left[\sigma^2 b_0^2 - 4\sigma b_0 - 10\sigma^2 - 15\sigma - 2(\sigma b_0 + 3)e^{-\sigma b_0} - b_0 K_3/30\right] b_0^4 E_1(b_0) - \sigma^5 b_0^4 E_1(\sigma b_0)$$
$$+(\sigma^5 + 10\sigma^2 + 15\sigma + 6) b_0^4 E_1[(1+\sigma)b_0]\Big\}, \qquad (C4)$$

with

$$E_1(x) = \int_x^\infty \frac{e^{-t}}{t} dt, \qquad (C5)$$

which is related to the exponential integral [114]. The first three of these, which are plotted in Fig. C1, depend only on the product σb_0, that is, they are determined uniquely by the single parameter B. The fourth, which depends on both B and σ, is plotted in Fig. C2 for different values of σ. As B approaches infinity, the values of K_1, K_2 and K_3 all approach zero, while K_4 diverges (in proportion to B^2). At $B = 0$, K_3 and K_4 vanish, but K_1 and K_2 are positive. Typically K_1 is the largest and most important of these four functions, while K_2 is the second most important, altough all four have significant effects on the solution.

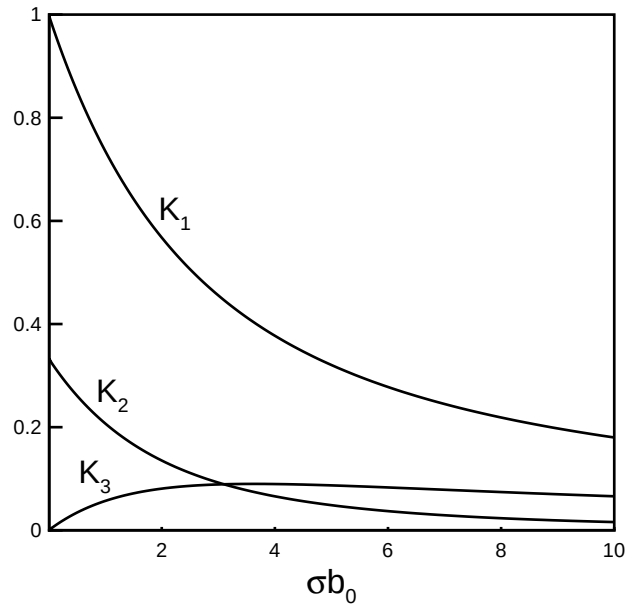

Figure C.1 Variations of the integration constants K_1, K_2 and K_3, given by Eqs. (C1), (C2) and (C3), with the product σb_0 related to the transfer number.

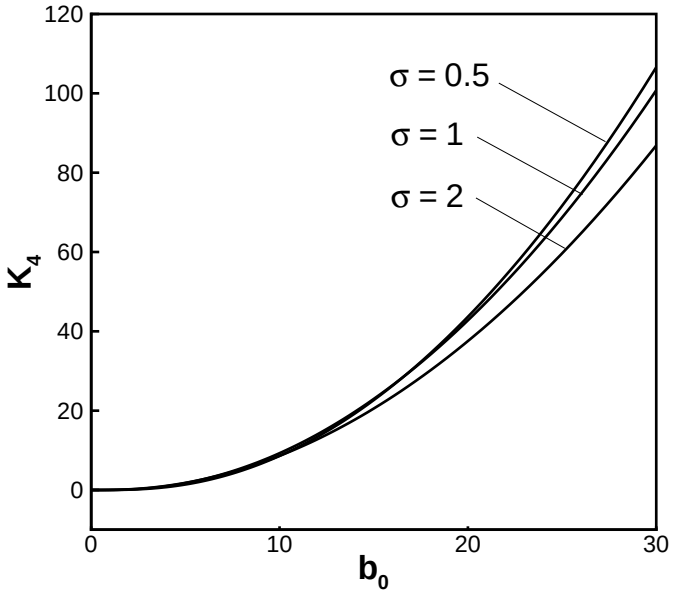

Figure C.2 Variations of the integration constant K_4, given by Eq. (A4), with the unperturbed nondimensional vaporization rate b_0 for various values of the Prandtl number ($\sigma = 0.5, 1$ and 2).

Appendix D

The Limits of Weak And Strong Vaporization

The limiting case of weak vaporization of the droplet, $b_0 \ll 1$, is a regular perturbation problem at the leading orders. The solutions in the inner region can be written as series of powers of b_0 by expanding the expressions for λ, χ, f, g and h in Eqs. (5.24),(5.25) and (5.28)-(5.30) for small b_0. The constants A_1 and A_2 in Eqs. (5.26) and (5.27) and the constants K_1, K_2, K_3 and K_4 in Eqs. (C1)-(C4) can be expanded for small b_0, giving $A_1 = b_0^3/3 - b_0^4/8 + O(b_0^5)$, $A_2 = b_0^3/6 - b_0^4/8 + O(b_0^5)$, $K_1 = 1 - \sigma b_0/3 + \sigma^2 b_0^2/12 + O(b_0^3)$, $K_2 = 1/3 - \sigma b_0/6 + O(b_0^2)$, $K_3 = \sigma b_0/12 - \sigma^2 b_0^2/30 + O(b_0^3)$ and $K_4 = \sigma b_0^4/36 - (2\sigma^2 + 3\sigma) b_0^5/216 + O(b_0^5 \ln b_0)$. Introducing these results into Eq. (5.25) and expanding for small b_0 gives

$$\chi = \frac{3\sigma b_0}{8} + O(b_0^2). \qquad (D1)$$

The integral in Eq. (5.28) can be expanded for small b_0 and values of r of order unity giving $(r^5 - 1)/(5b_0^5) - (r^3 - 1)/(6b_0^3) + (r^2 - 1)/(6b_0^2) - (r - 1)/(8b_0) + O(\ln r)$. Employing this result and the expansions of χ and A_1 in Eq. (5.28) gives, at leading order in b_0,

$$f = r^2 + \frac{1}{2r} - \frac{3r}{2} + \frac{3}{16}\left[6 - (3+\sigma)\left(\frac{1}{r} + r\right)\right] b_0 + O(b_0^2). \qquad (D2)$$

The corresponding expansion for g in Eq. (5.29) is

$$g = g_\infty(1 - 1/r)(1 - \sigma b_0/r) + O(b_0^2), \tag{D3}$$

and from Eqs. (5.30) and (D2),

$$h = \frac{1}{2} - \frac{3}{4r} + \frac{3}{8r^2} - \frac{1}{8r^3} + O(b_0). \tag{D4}$$

Through Eq. (5.23) and other equations, these results determine the velocity and temperature fields for nonvaporizing and weakly vaporizing droplets. In particular, the first term in Eq. (D2) gives the well-known Stokes stream function for flow around a solid sphere, and the second term is the correction for weak vaporization.

The limiting case of strong vaporization, $b_0 \gg 1$, is somewhat more involved. Near the droplet surface the solutions for g and h are exponentially small, implying temperatures determined by the unperturbed spherically symmetrical temperature field, and f can be expanded in powers of b_0^{-1} to obtain

$$f = -\frac{\chi_\infty}{3}\left(r^2 + \frac{2}{r}\right) + O(b_0^{-1}), \tag{D5}$$

with χ_∞ given by Eq. (5.36). Then, at leading order in b_0^{-1}, the solution near the surface becomes isothermal and irrotational, the flow being purely radial in the first approximation.

At radial distance of order b_0, for large b_0, the solution can be written in the appropriate rescaled variables $\bar{r} = r/b_0$, $\bar{f} = f/b_0^2$, $\bar{g} = g/b_0$ and $\bar{h} = h/b_0$. Then, at leading order in b_0^{-1}, the inner solution in this region can be written as

$$\bar{f} = 2\,(3 + \chi_\infty)\left[\frac{\bar{r}^4}{5} - \frac{1}{\bar{r}}\int_0^{\bar{r}}\left(\xi^3 + \xi^4\right)e^{-1/\xi}d\xi\right] - \chi_\infty\frac{\bar{r}^2}{3}, \tag{D7}$$

$$\bar{g} = \bar{g}_\infty e^{-\sigma/\bar{r}}, \tag{D8}$$

with $\bar{g}_\infty = g_\infty/b_0$, and

$$\bar{h} = \left[\int_0^{\bar{r}} \left(\frac{2\xi}{\sigma} - 1\right) \frac{\bar{f}d\xi}{\xi^2}\right] \left(\frac{2\bar{r}}{\sigma} + 1\right) e^{-\sigma/\bar{r}} - \left[\int_0^{\bar{r}} \left(\frac{2\xi}{\sigma} + 1\right) \frac{\bar{f}e^{-\sigma/\xi}d\xi}{\xi^2}\right] \left(\frac{2\bar{r}}{\sigma} - 1\right). \quad (D9)$$

The vorticity function written in Eq. (5.34) can be seen directly to depend only on $\bar{r}$, apart of a scaling prefactor, just σ-dependent, determining its strength. These solutions describe the flow and temperature fields associated with the interaction of a point source with a uniform flow at a temperature different from that of the source.

Appendix E

Calculations Needed For Obtaining The Composite Solution Of The Stream function and Temperature

In order to match the inner and outer solution, the asymptotic expansions of θ and ψ for large r and of Θ and Ψ for small R need to be obtained. To derive the θ expansion for large r, the expressions for θ_0, g and h from Eqs. (5.19), (5.29) and (5.30) can be expanded in the large-r limit to give, up to terms of order $1/r^2$

$$\theta_0 = 1 - \frac{(1+B)\ln(1+B)}{B}\frac{1}{r}, \tag{E1}$$

$$g = g_\infty \left\{1 - [1 + \ln(1+B)]\,(1/r)\right\} \tag{E2}$$

and

$$h = \frac{(1+B)\ln(1+B)}{B}\left\{\frac{1}{2} + \frac{B_1}{r}\right\}, \tag{E3}$$

with B_1 given by Eq. (5.43). Combinig these results according to Eqs. (5.18) and

(5.23), the asymptotic expansion of θ for large r can be expressed as

$$\theta \sim \theta_\infty - \frac{q_\infty}{r}, \tag{C4}$$

with θ_∞ and q_∞ given by Eqs. (5.41) and (5.42) in the main text. To obtain the ψ expansion for large r, the asymptotic expansion of the integral in Eq. (5.28) for large r can be written as $(r^5-1)/(5b_0^5) - (r^3-1)/(6b_0^3) + (r^2-1)/(6b_0^2) - (r-1)/(8b_0) + O(\ln r)$, leading to an expansion of f which can be used with Eqs. (5.18), (5.19) and (5.23) to show that

$$\psi = -\mu b_0 + \epsilon U \left\{ -\frac{\mu g_\infty B}{1+B} + \frac{1-\mu^2}{2}\left[r^2 + \frac{b_0^3(3+\chi)}{6A_1}\left(r + \frac{3b_0}{4}\right) + \left\{ \frac{(3+\chi)b_0^4}{8A_1} - (1+\chi)\right\}\frac{1}{r}\right]. \right. \tag{E5}$$

By introducing the expansion for Q given by Eq. (5.44) inside the integral in Eq. (5.47) and changing to a more convenient variable $\zeta = R/\sqrt{4\hat{\tau}/\sigma}$, at leading order in ϵ the expression

$$\Theta' = \frac{\sigma b_0(1+B)}{BR}\sqrt{\frac{4}{\pi}}\int_0^\infty \exp\left[-\zeta^2\left(1 - 2\mu Y R^{-1} + Y^2 R^{-2}\right)\right] d\zeta \tag{E6}$$

is obtained, with $Y = X_d(\tau) - X_d(\tau - \sigma R^2/4\zeta^2)$. An asymptotic expansion of the integral in Eq. (E6) for small values of R can be obtained by breaking the integral into two parts, $\int_0^\lambda + \int_\lambda^\infty$, with $R \ll \lambda \ll 1$. Since $U = dX_d/d\tau$, use of a Taylor expansion in the expression for Y shows that the approximation $Y = \sigma U R^2/(4\zeta^2)$ is valid in the interval $\lambda < \zeta < \infty$, reducing the argument of the exponential in Eq. (E6) to $-\zeta^2 + \mu\sigma U R/2 - \sigma^2 U^2 R^2/(16\zeta^2)$, so that the second of these integrals becomes proportional to $erfc(\lambda)$ and, in the limit of small λ, approaches $(\sqrt{\pi}/2)(1+\mu\sigma U R/2)$ when expanded to first order for small R. In the first integral an appropriate variable is $\xi = \zeta/R$, in terms of which this integral becomes, up to terms of order R^2, $R\int_0^{\lambda/R} exp[-Y\xi^2(Y - 2\mu R)]d\xi$, in which $Y = \int_{\tau-\sigma/4\xi^2}^{\tau} U(\tau')d\tau'$ in

the present variables. Since Y is seen from this expression to become proportional to ξ^{-2} for large ξ, the leading-order term in the argument of the exponential for small R vanishes for large ξ, causing the exponential to approach unity and the integral to diverge as λ/R approaches infinity. It is therefore appropriate to add and subtract $R\int_0^{\lambda/R} d\xi = \lambda$, obtaining, up to terms of order R^2, $\lambda - R\int_0^{\lambda/R}(1 - e^{-Y^2\xi^2})d\xi$, which, in the limit of vanishing λ and R/λ, approaches $\sqrt{\pi}R\Gamma/2$, with Γ defined by Eq. (5.49), a convergent integral. Combining these results produces an asymptotic expansion of Θ' for small values of R, given by Eq. (5.48), which can be introduced into Eq. (5.45) to give, up to terms of order ϵ^2, the expansion

$$\Theta = 1 - \epsilon\frac{\sigma b_0(1+B)}{B}\left\{\frac{1}{R} - \Gamma + \mu\frac{\sigma U}{2}\right\} + O(R). \qquad (E7)$$

The procedure used to obtain the expansion in Eq. (E7) can be followed to expand the integral in Eq. (5.56), as well, which can be written in terms of $\zeta' = R/\sqrt{4\hat{\tau}}$ and Y to give

$$\Psi'_R = -\frac{(3+\chi)b_0^4}{3A_1\sqrt{\pi}}\int_0^\infty H(\tau,\zeta')d\zeta', \qquad (E8)$$

with

$$H(\tau,\zeta') = \left[\left(UR/2\zeta'^2 - \mu - Y/R\right)e^{-\zeta'^2\left(1-2\mu YR^{-1}+Y^2R^{-2}\right)} + \mu e^{-\zeta'^2}\right\} \times \left[e^{-(1-\mu^2)\zeta'^2} - 1\right]. \qquad (E9)$$

An asymptotic expansion of Ψ'_R for small values of R can be obtained by breaking the integral of Eq. (E9) into two parts, $\int_0^\lambda + \int_\lambda^\infty$. Introducing the approximation $Y = aR/\zeta'^2$ in the second of these integrals gives $-[I_1(a,\lambda) - I_1(\mu a,\mu\lambda)] + [\mu I_2(a,\lambda) - I_2(\mu a,\mu\lambda)$, with $a = UR/4$,

$$I_1(a,\lambda) = \frac{\sqrt{\pi}}{4}\left\{e^{2(1+\mu)a}[1 + erf(\lambda + a/\lambda)] - e^{-2(1-\mu)a}[1 + erf(\lambda - a/\lambda)]\right\}, \qquad (E11)$$

and

$$I_2(a,\lambda) = \frac{\sqrt{\pi}}{4}\ e^{-2(1-\mu)a}[1 - erf(\lambda - a/\lambda)] + e^{2(1+\mu)a}[1 - erf(\lambda + a/\lambda)] - 2[1 + erf(\lambda)]. \quad (E12)$$

The expressions for $I_1(\mu a, \mu\lambda) - I_1(a,\lambda)$ and $\mu I_2(a,\lambda) - I_2(\mu a, \mu\lambda)$ can be expanded for small a, λ and a/λ. Neglecting higher-order terms gives

$$I_1(\mu a, \mu\lambda) - I_1(a,\lambda) = \sqrt{\pi}a(\mu - 1) - \lambda a e^{2\mu a}(1 - \mu^2) + \sqrt{\pi}2a^2\mu(\mu - 1) - \frac{a^3}{\lambda}e^{2\mu a}(1 - \mu^2) \quad (E13)$$

and

$$\mu I_2(a,\lambda) - I_2(\mu a, \mu\lambda) = \frac{\sqrt{\pi}}{2}(\mu - 1)(e^{2\mu a} - 1) + \sqrt{\pi}a^2\mu(1 - \mu) + \frac{2}{3}a\lambda^3\mu^2(1 - \mu^2) - \frac{a^4}{2\lambda}\mu(1 - \mu^2). \quad (E14)$$

The first integral becomes $R^3(1 - \mu^2)[J_1 + \mu R J_2]$, with

$$J_1 = \int_{R/\lambda}^{\infty} \xi'^{-4}[2U(\tau - \xi'^2/4)\xi'^2/4 - Y] \exp\{-Y\xi'^{-2}[Y - 2\mu R]\} d\xi' \quad (E15)$$

and

$$J_2 = \int_{R/\lambda}^{\infty} \xi'^{-4}[1 - \exp\{-Y\xi'^{-2}[Y - 2\mu R]\} d\xi', \quad (E16)$$

where $\xi' = R/\zeta'$. The integrals J_1 and J_2 are divergent in the limit of vanishing R/λ. If $(a/R)e^{\mu 2a}\int_{R/\lambda}^{\infty}\xi'^{-2}d\xi'$ is added to and substracted from J_1, it is found that

$$\int_{R/\lambda}^{\infty} \{\xi'^{-4}[2U(\tau - \xi'^2/4)\xi'^2/4 - Y] \exp(-Y\xi'^{-2}[Y - 2\mu R]) - (a/R)e^{\mu 2a}\xi'^{-2}\} d\xi' + a\lambda e^{2\mu a}/R^2. \quad (E17)$$

The last integral is convergent in the limit $R/\lambda \to 0$, so it can be split as $\int_0^\infty - \int_0^{R/\lambda}$. Using the approximation $Y = U\xi'^2/4$ in the second of the last integrals gives $a^3 R^{-2} e^{2\mu a}/\lambda + O(R^2)$. Adding and substracting $\int_{R/\lambda}^\infty \{[1-e^{2\mu a}]y^{-4} + a^2\xi'^{-2}]d\xi'$ for J_2 gives

$$\int_{R/\lambda}^\infty \{\xi'^{-4}[e^{2\mu a} - \exp\{-Y\xi'^{-2}[Y - 2\mu R]\}] - a^2\xi'^{-2}/R^2\}d\xi' + (1-e^{2\mu a})\lambda^3/3R^3 + a^2\lambda/R^3. \quad (E18)$$

The last integral is convergent, so it can be split as $\int_0^\infty - \int_0^{R/\lambda}$. The second of these integrals can be expanded to give $-a^4/(2R^3\lambda)$. Combining these results gives an asymptotic expansion of Ψ'_R for small values of R, given by Eq. (5.59), which can be introduced in Eq. (5.45) to give, up to terms of order ϵ^2, the expansion

$$\Psi = \frac{1}{2}UR^2(1-\mu^2) + \epsilon\left\{\mu b_0 + \frac{(\chi+3)b_0^4}{A_1}\frac{(1-\mu^2)}{12}\left[UR + \mu\frac{U^2}{4} - \Pi\right]R^2\right\}, \quad (E19)$$

where

$$\Pi = \frac{2}{\sqrt{\pi}}\int_0^\infty \xi^{-2}\left[(U - 2Y/\xi^2)e^{-Y^2\xi^{-2}} - U(\tau)e^{\mu RU(\tau)/2\}}\right]d\xi \quad (E20)$$

and the term $-\mu b_0$ inside the square brackets in Eq. (E18) corresponds to the leading-order term in ϵ of the streamfunction associated with the first component of $\vec{V}'$ in Eq. (5.54).

References

[1] Hirschfelder J. O., Curtiss C. F., and Bird R. B. Molecular Theory of Gases and Liquids. John Wiley Sons, New York, 1954.

[2] Williams, F. A. Combustion Theory. Second Edition, Addison-Wesley, Redwood City, CA, 1985.

[3] Buckmaster, J., Clavin, P., Liñán, A., Matalon, M., Peters, N., Sivashinsky, G., and Williams, F.A. Combustion Theory and Modelling. Proceedings of the Combustion Institute, 30, 2005, pp. 1-19.

[4] Liñán and Williams, F. A. Fundamental Aspects of Combustion, Oxford University Press, New York, 1993.

[5] Lewis, B. and von Elbe, G. Combustion, Flames and Explosions of Gases. Academic Press, New York, 3rd edition, 1987, p. 26.

[6] Steinberg, M. and Kaskan, W.E. The ignition of combustible mixtures by shock-waves. Proc. Combust. Inst., Vol. 5, 1955, pp. 664-672.

[7] Schott, G.L. and Kinsey, J.L. Kinetic studies of hydroxyl radicals in shock waves II: Induction times in the hydrogen-oxygen reaction. J. Chem. Phys., Vol. 29, 1958, pp. 1177-1182.

[8] Strehlow, R. A. and Cohen, A. Initiation of detonation. Phys. Fluids, Vol. 5, 1962, pp. 97-101.

[9] Fujimoto, S. Chemical reaction in a shock-wave I: The ignition delay of a hydrogen-oxygen mixture in a shock tube. Bull. Chem. Soc. Japan, Vol. 36, 1963, pp. 1233-1236.

[10] Miyama, H. and Takeyama, T. Kinetics of hydrogen-oxygen reaction in shock-waves. J. Chem. Phys., Vol. 41, 1964, pp. 2287-2290.

[11] Asaba, T., Gardiner, W. C. and Stubbeman, R.F. Shock-tube study of the hydrogen-oxygen reaction. Proc. Combust. Inst., Vol. 10, 1965, pp. 295-302.

[12] Belles, F.E. and Lauver, M.R. Effects of concentration and of vibrational relaxation on the induction period of the H_2-O_2 reaction. Proc. Combust. Inst., Vol. 10, 1965, pp. 285-293.

[13] Skinner, G.B. and Ringrose, G.H. Ignition delays of a hydrogen-oxygen-argon mixture at relatively low temperature. J. Chem. Phys., Vol. 42, 1965, pp. 2190-2192.

[14] Snyder, A.D., Robertson, J., Zanders, D.L. and Skinner, G.B. Shock-tube studies of fuel-air ignition characteristics, Report AFAPL-TR-65-93, 1965.

[15] Voevodsky, V.V. and Soloukhin, R.I. On the mechanism and explosion limits of hydrogen-oxygen chain self-ignition in shock waves. Proc. Combust. Inst., Vol. 10, 1965, pp. 279-283.

[16] White, D.R. and Moore, G.E. Structure of gaseous detonations IV: induction zone studies in H_2-O_2 and CO-O_2 mixtures. Proc. Combust. Inst., Vol. 10, 1965, pp. 785-795.

[17] Craig, R.R. A shock-tube study of the ignition delay of hydrogen-air mixtures near the second explosion limit. Report AFAPL-TR-66-74, 1966.

[18] Cohen, A. and Larsen, J. Explosive mechanism of the H_2-O_2 reaction near the second ignition limit. Report BRL 1386, 1967.

[19] White, D.R. Density induction times in very lean mixtures of D_2,H_2,C_2H_2 and C_2H_4 with O_2. Proc. Combust. Inst., Vol. 11, 1967, 147-154.

[20] Just, T. and Schmalz, F. Measurements of ignition delays of hydrogen-air mixtures under simulated conditions of supersonic combustion chambers. AGARD CP No. 34, Part 2, Paper 19, 1968.

[21] Jachimowski, C.J. and Houghton, W.M. Shock-tube study of the initiation process in the hydrogen-oxygen reaction. Combust. Flame, Vol. 17, 1971, pp. 25-30.

[22] Bhaskaran, K.A., Gupta, M.C. and Just, T. Shock-tube study of the effect of unsymmetric dimethyl hydrazine on the ignition characteristics of hydrogen-air mixtures. Combust. Flame, Vol. 21, 1973, pp. 45-48.

[23] Cheng. R.K. Induction times and strong ignition limits for mixtures of methane with hydrogen. PhD Dissertation, University of California, Berkeley, 1977.

[24] Slack, M. and Grillo, A. Investigation of hydrogen-air ignition sensitized by

nitric oxide and by nitrogen dioxide. NASA CR-2896 Report, Contract NAS 1-14348, 1977.

[25] Blumenthal, R., Fieweger, K., Komp, K., Adomeit, G. and Gelfond, B.E. Self-ignition of H_2-air mixtures at high pressures and low temperature. 20th Intl. Symp. on Shock Waves, 1996, pp. 935-940.

[26] Petersen, E.L., Davidson, D.F., Röhrig, M. and Hanson, R.K. High-pressure shock-tube measurements of ignition times in stoichiometric $H_2/O_2/Ar$ mixtures. 20th Intl. Symp. on Shock Waves, 1996, pp. 941-946.

[27] Wang, B.L., Olivier, H. and Gronig, H. Ignition of shock-heated H2-air-steam mixtures. Combust. Flame, Vol. 133, 2003, pp. 96-106.

[28] Petersen, E.L., and Hanson, R.K., Nonideal effects behind reflected shock waves in a high-pressure shock tube. Shock Waves, Vol. 10, No. 6, 2001. pp. 405-420.

[29] Matsuo, A. and Fujii, K. Prediction Method of Unsteady Combustion Around Hypersonic Projectile in Stoichiometric Hydrogen-Air. Institute of Space and Aeronautical Sciences, Japan, Vol. 36, No. 10, 1998, pp. 1834-1840; AIAA Paper 96-3137.

[30] Law, C.K., Sung, C.J., Wang, H. and Lu, T.F. Development of Comprehensive Detailed and Reduced Reaction Mechanisms for Combustion Modelling. AIAA Journal, Vol. 41, No. 9, 2003, pp. 1629-1646.

[31] Williams, F.A. Propulsion Combustion: Fuel to emissions. Chapter 4. Taylor Francis, Washington D.C., 1998, pp. 93-128.

[32] Kushida, R. The reactions of hydrogen and oxygen at high temperature. National Engineering Science Company, Air Force Contract No. AF 3396160-8506, 1962.

[33] Treviño, C. Ignition phenomena in $H_2 - O_2$ mixtures. Progress in Astronautics and Aeronautics, Vol. 131, 1991, pp. 19-43.

[34] Gray, P. and Lee, P.R. Thermal Explosion Theory. Oxidation and Combustion Reviews, Vol. 2, 1967, pp. 1-183.

[35] Frank-Kamenetskii, D.A. Diffusion and Heat Transfer in Chemical Kinetics. Second edition, Plenum Press, New York, 1969.

[36] Kassoy, D.R. and Poland, J. The Subcritical Spatially Homogeneous Explosion: Initiation to Completion. Combustion Science and Technology, Vol. 11, Nos. 3-4, 1975, pp. 147-152.

[37] Birkan, M. and Kassoy D. R. The Unified Theory for Chain Branching Thermal Explosions with Dissotiation-Recombination and Confinement Effects. Combustion Science and Technology, Vol. 44, Nos. 5-6, pp. 223-256.

[38] Sidhu, H.S., Forbes, L.K. and Gray, B.F. Analysis of the Unified Thermal and Chain Branching Model of Hydrocarbon Oxidation. Proceedings of the Royal Society A, Vol. 449, 1995, pp. 493-514.

[39] Varatharajan, B. and Williams, F. A. Ignition Times in the Theory of Branched-Chain Thermal Explosions. Combustion and Flame, Vol. 121, No. 3, 2000, pp. 551-554.

[40] Bonilla, L.L., Sánchez, A.L., and Carretero, M. The description of homogeneous branched-chain explosions with slow radical recombination by self-adjusting time scales. SIAM Journal of Applied Mathematics, Vol. 61, No. 2, 2000, pp. 528-550.

[41] Kapila, A. K. Homogeneous Branched-Chain Reactions: Initiation to Completion. Journal of Engineering Mathematics, Vol. 12, 1978, pp. 221-235.

[42] Maas, U. and Warnatz, J. Ignition processes in hydrogen-oxygen mixtures. Combust. Flame, Vol. 74, 1988, pp. 53-69.

[43] Miller, J.A. and Bowman, C.T. Mechanism and modelling of nitrogen chemistry in combustion. Prog. Energy Combust. Sci., Vol. 15, 1989, pp. 287-338.

[44] Balakrishnan, G. and Williams, F.A. Turbulent combustion regimes for hypersonic propulsion employing hydrogen-air diffusion flames. J. Prop. Power, Vol. 10, 1995, pp. 434-437.

[45] Tan, Y., Dagaut, P., Cathonnet, M. and Boettner, J. Acetylene oxidation in a JSR from 1 to 10 atm and comprehensive kinetic modeling. Combust. Sci. Tech., Vol. 102, 1994, pp. 21-55.

[46] Frenklach, M., Wang, H., Goldenberg, M., Smith, G.P., Golden, D.M., Bowman, C.T., Hanson, R.K., Gardiner, W.C. and Lissianski,V. Gas Research Institute Topical Report No. GRI-95/0058, 1995.
$http://www.me.berkeley.edu/gri.mech/data/frames/.htlm.$

[47] Ranzi, E., Gaffuri, P., Faravelli, T. and Dagaut, P. A wide-range modelling study of n-heptane oxidation. Combust. Flame, Vol. 103, 1995, pp. 91-106.

[48] Marinov, N., Westbrook, C.K. and Pitz, W.J. Detailed and global chemical kinetics model for hydrogen. Transport Phenomena in Combustion, Volume 1 (S.H. Chan, editor), Taylor and Francis, Washington, DC (UCRL-JC-120677), 1996.

[49] Allen, M.T., Yetter, R.A. and Dryer, F.L. High pressure studies of moist carbon monoxide nitrous oxide kinetics. Combust. Flame, Vol. 109, 1997, pp. 449-470.

[50] Lindstedt, R.P. and Skevis, G. Chemistry of acetylene flames. Combust. Sci. Tech., Vol. 125, 1997, pp. 73-137.

[51] Glarborg, P., Alzueta, M.U., Dam-Johansen, K. and Miller, J.A. Kinetic modeling of hydrocarbon/nitric oxide interactions in a flow reactor. Combust. Flame, Vol. 115, 1998, pp. 1-27.

[52] Mueller, M.A., Yetter, R.A., and Dryer, F.L. Flow reactor studies and kinetic modelling of the H_2/O_2 reaction. Int. J. Chem. Kinet., Vol. 31, 1999, pp. 113-125.

[53] Bhattacharjee, B., Schwer D. A., Barton P. I. and William H. Optimally-reduced kinetic models: reaction elimination in large-scale kinetic mechanisms. Combust. Flame, Vol. 135, 2003, pp. 191-208.

[54] Li, J., Zhao, Z., Kazakov, A. and Dryer, F.L. An Updated Comprehensive Kinetic Model for H_2 Combustion. Fall Technical Meeting of the Eastern States Section of the Combustion Institute, Penn State University, University Park, PA., 2003.

[55] Del Alamo, G., Williams F. A. and Sánchez. A. L. Hydrogen-Oxygen Induction Times Above Crossover Temperatures. Combustion Science and Technology, Vol. 176, No. 10, 2004, pp. 1599-1626.

[56] Saxena P., Williams F. A. Testing a small detailed chemical-kinetic mechanism for the combustion of hydrogen and carbon monoxide. Combustion and Flame, Vol. 145, 2006, pp. 316-323.
http : *//www.mae.ucsd.edu/combustion/cermech.*

[57] Matsen D.A., Hanson, R.K., and Bowman, C.T. Shock-tube study of the reaction $H+O_2 \rightarrow O+OH$ using OH laser-absorption. Journal of Physical Chemistry, Vol. 94, No. 18, 1990, pp. 7119-7128.

[58] Yetter, R.A., Dryer, F.L., and Rabitz, H. A comprehensive reaction-mechanism for carbon-monoxide hydrogen oxygen kinetics. Combustion Science and Technology, Vol. 79, 1991, pp. 97-118.

[59] Baulch, D.L. Evaluated kinetic data for combustion modelling. Journal of Physical and Chemical Reference Data, Vol. 21, No. 3, 1992, pp. 411-736.

[60] Mueller, M. A., Kim, T. J., Yetter, R. A. and Dryer, F. L.. Flow reactor

studies and kinetic modeling of the H_2/O_2 reaction. International Journal of Chemical Kinetics, Vol. 31, No. 2, 1999, pp. 113-125.

[61] Sridharan, W.C., Qiu, L.X. and Kaufman, F. Kinetic and product channels of the reaction of HO_2 with O and H atoms at 296K. J. Phys. Chem., Vol. 86, 1982, pp. 4569-4574.

[62] Warnatz, J. Combustion Chemistry. W.C. Gardiner, Ed. Springer-Verlag, New York, 1984, Ch. 5.

[63] Keyser, L.F. Absolute rate constant and branching fraction for the $H+HO_2$ reaction from 245 to 300K. J. Phys. Chem., Vol. 90, 1986, pp. 2994-3003.

[64] Michael, J.V., Sutherland, J. W., Harding, L. B. and Wagner, A. F. Initiation in H_2/O_2: Rate Constants for $H_2+O_2 \rightarrow H+HO_2$ at High-Temperature. Proceedings of the Combustion Institute, Vol. 28, 2000, pp. 1471-1478.

[65] Semenov, N.N. Some Problems in Chemical Kinetics and Reactivity. Princeton University Press, Princeton, New Jersey, 1959, Ch. 10.

[66] Ripley, D.L. and Gardiner, W.C. Shock-tube study of the hydrogen-oxygen reaction. II. Rate of exchange initiation. J. Chem. Phys., Vol. 44, 1966, pp. 2285-2296.

[67] Troe, J. Detailed modelling of the temperature and pressure dependence of the reaction $H + O_2 (+ M) \rightarrow HO_2 (+ M)$. Proc. Combust. Inst., Vol. 28, 2001, pp. 1463-1469.

[68] Pitsch, H. Entwicklung eines Programmpaketes zur Berechnung eindimensionaler Flammen am Beispiel einer Gegenstromdiffusionsflamme. Master's Thesis, RWTH Aachen, Germany, 1993.

[69] Kee, R. J., Rupley, F. M. and Miller J. A. Chemkin II: A Fortran Chemical Kinetics Package for the analysis of Gas-Phase Chemical Kinetics. Sandia National Laboratories Report No. SAND89-8009, 1989.

[70] Petersen, E.L., and Hanson, R.K. Reduced kinetics mechanisms for ram accelerator combustion. Journal of Propulsion and Power, Vol. 15, 1999, pp. 591-600.

[71] Gilbert, R.G., Luther, K. and Troe, J. Theory of thermal unimolecular reactions in the fall-off range. ii. weak collision rate constants. Ber. Bunsenges. Phys. Chem., Vol. 87, 1983, pp. 169-177.

[72] Seshadri, K., Peters, N. and Williams F. A. Asymptotic Analysis of Stoichio-

metric and Lean Hydrogen-Air flames. Combustion and Flame, Vol. 96, No. 4, 1994, pp. 407-427.

[73] Sánchez, A.L., Liñán, A. and Williams, F. A. A Bifurcation Analysis of High-Temperature Ignition of H_2-O_2 Diffusion Flames. Proceedings of the Combustion Institute, Vol. 25, 1994, pp. 1529-1537.

[74] Godsave, G. A. E. Studies of the combustion of drops in a fuel spray: the burning of single drops of fuel. Proceeding of the Combustion Institute, Vol. 4, 1953, pp. 818-830.

[75] Spalding, D. B. The combustion of liquid fuels. Proceedings of the Combustion Institute, Vol. 4, 1953, pp. 847-864.

[76] Williams, F. A. Combustion Theory. Addison-Wesley, Reading, MA, 1965, pp. 47-57.

[77] Williams, A. Combustion of droplets of liquid fuels: a review. Combustion and Flame, Vol. 21, 1973, pp. 1-31.

[78] Faeth, G. M. Current status of droplet and liquid combustion. Progress in Energy and Combustion Science, Vol. 3, 1977, pp. 191-234.

[79] Law C. K. Recent advances in droplet vaporization and combustion. Progress in Energy and Combustion Science, Vol. 8, 1982, pp. 171-201.

[80] Fendell, F. E., Sprankle, M. L. and Dodson, D. S. Thin-flame theory for a fuel droplet in slow viscous flow. Journal of Fluid Mechanics, Vol. 26, 1966, pp. 267-280.

[81] Fendell, F.E. Decompositional burning of a droplet in a small Peclet number flow. AIAA Journal, Vol. 6, 1968, pp. 1946-1953.

[82] Gogos, G., Sadhal, S.S., Ayyaswamy, P.S. and Sundararajan, T. Thin-flame theory for the combustion of a moving liquid-drop. Effects due to variable density. Journal of Fluid Mechanics, Vol. 171, 1986, pp. 121-144.

[83] Jog, M. A., Ayyaswamy, P. S. and Cohen, I.M. Evaporation and combustion of slowly moving luiquid fuel droplets. Journal of Fluid Mechanics, Vol. 307, 1996, pp. 135-165.

[84] Wichman, I. S. and Baum, H. R. A solution procedure for low Reynolds number combustion problems under microgravity conditions. Heat Transfer in Microgravity, C. T. Avedisan and V. A. Arpaci, editors, American Society of Mechanical Engineers, 1993, New York, pp. 111-117.

[85] Ackerman, M. D. and Williams. F. A. A simplified model for drplet combustion in a slow convective flow. Combustion and Flame, Vol. 143, 2005, pp. 599-612.

[86] Crespo, A., and Liñán, A. Unsteady effects in droplet evaporation and combustion. Combustion Science and Technology, Vol. 11, 1975, pp. 9-18.

[87] Waldman, C. H. Theory of non-steady state droplet combustion. Proceedings of the Combustion Institute, Vol. 5, 1975, pp. 429-442.

[88] Sirignano, W. Fuel-droplet vaporization and spray combustion theory. Progress in Energy and Combustion Science, Vol. 9, 1983, pp. 299-322.

[89] Williams, F. A. Combustion Theory Second Edition, Addison-Wesley, Redwood City, CA, 1985, pp. 52-69.

[90] Dwyer, H. A. Calculation of droplet dynamics in high temperature environment. Progress in Energy and Combustion Science, 15, 1989, pp. 131-158.

[91] Sirignano W. A. Fluid Dynamics and Transport of Droplets and Sprays. Cambridge University Press, Cambridge, 1999, pp. 7-76.

[92] Chiu, H. H. Advances and challenges in droplet and spray combustion. I. Towards a unified theory of droplet aerothermochemistry. Progress in Energy and Combustion Science, Vol. 26, 2000, pp. 381-416.

[93] Fucks, N. A. Evaporation and Droplet Growth in Gaseous Media. Pergamon Press, London, 1959.

[94] Levich, V. G. Physicochemical Hydrodynamics. Prentice-Hall, Englewood Cliffs, NJ, 1962, pp. 395-457.

[95] Sadhal, S.S., and Ayyaswamy, P.S. Flow past a fluid drop with a large nonuniform radial velocity. Journal of Fluid Mechanics, Vol. 133, 1983, pp. 65-81.

[96] Stokes, G. G. On the effect of internal friction of fluids on the motion of pendulums. Transactions of the Cambridge Philosophical Society, Vol. 9, Part. II, 1851, pp. 8-106.

[97] Oseen, C. W. Ueber die Stokes'sche formel, und über eine verwandte aufgave in der Hydrodynamik. Arkiv för matematik, astronomi och fysik, Vol. 6, 1910, pp. 1-20.

[98] Proudman, I. and Pearson, J. R. A. Expansions of small Reynolds numbers for the flow past a sphere and a circular cylinder. Journal of Fluids Mechanics, Vol. 2, 1957, pp. 237-262.

[99] Acrivos, A. and Taylor, T. D. Heat and mass transfer from single spheres in Stokes flow. Physics of Fluids, Vol. 5, 1962, pp. 387-394.

[100] Brenner, H. Forced convection heat and mass transfer at small Peclet numbers from a particle of arbitrary shape. Chemical Engineering Science, Vol. 18, 1963, pp. 63-148.

[101] Batchelor, G. K. Mass transfer from a particle suspended in fluid with a steady linear ambient velocity distribution. Journal of Fluid Mechanics, Vol. 95, Part 2, 1979, pp. 369-400.

[102] Chung, J.N., Ayyaswamy, P.S., and Sadhal S.S. Laminar condensation on a moving drop. Part 1. Singular perturbation technique. Journal of Fluid Mechanics, Vol. 139, 1984, pp. 105-130.

[103] Clift, R. Grace, J. R. and Weber M. E. Bubbles, Drops, and Particles. Academic Press, New York, 1978.

[104] Ockendon, R.J. The unsteady motion of a small sphere in a viscous liquid. Journal of Fluid Mechanics, Vol. 34, 1968, pp. 229-239.

[105] Sano, T. Unsteady flow past a sphere at low Reynolds number. Journal of Fluid Mechanics, Vol. 112, 1981, 433-441.

[106] Hinch, E. J. The approach to steady state in Oseen flows. Journal of Fluid Mechancics, Vol. 256, 1993, pp. 601-604.

[107] Asmolov, E.S. Flow past a sphere undergoing unsteady rectilinear motion and unsteady drag at small Reynolds number. Journal of Fluid Mechanics, Vol. 446, 2001, pp. 95-119.

[108] Choudhury, P. N. and Drake, D. G. Unsteady heat transfer from a sphere in a low Reynolds number flow. Quarterly Journal of Mechanics and Applied Mathematics, Vol. 24, 1971, pp. 23-36.

[109] Abramzon, B. and Elata, C. Unsteady heat transfer from a single sphere in Stokes flow. International Journal of Heat and Mass Transfer, Vol. 27, 1984, pp. 687-695.

[110] Feng, Z. G. and Michaelides, E. E. Unsteady heat transfer from a sphere at small Peclet Numbers. Transcriptions of the ASME, Journal of Fluids Engineering, Vol. 118, 1996, pp. 96-102.

[111] Pozrikidis, C. Unsteady heat or mass transport from a suspended particle at low Péclet numbers. Journal of Fluid Mechanics, Vol. 334, 1997, pp. 111-133.

[112] Bender C. M. and Orszag S. A. Advanced Mathematical Methods for Scientists and Engineers. McGraw-Hill, New York, 1978.

[113] Lagerstrom, P. A. Matched Asymptotic Expansions: Ideas and Techniques. Applied Mathematical Sciences, Vol.76, Springer-Verlag, New York, 1988.

[114] Abramovitz, M. and Stegun, I. A. Handbook of Mathematical Functions. Dover, New York, 1965, p. 228.